PNWD-3300
WTP-RPT-076 Rev. 0

Identification of Washed Solids from Hanford Tanks 241-AN-102 and 241-AZ-101 with X-Ray Diffraction, Scanning Electron Microscopy, and Light-Scattering Particle Analysis

E. C. Buck
B. W. Arey
S. K. Fiskum
J. G. H. Geeting
E. D. Jenson
B. K. McNamara
A. P. Poloski

June 2003

WTP
Project
Report

Battelle – Pacific Northwest Division
Richland, Washington, 99352

LEGAL NOTICE

PNWD-3300
WTP-RPT-076 Rev. 0

Identification of Washed Solids from Hanford Tanks 241-AN-102 and 241-AZ-101 with X-Ray Diffraction, Scanning Electron Microscopy, and Light-Scattering Particle Analysis

E. C. Buck
B. W. Arey
S. K. Fiskum
J. G. H. Geeting
E. D. Jenson
B. K. McNamara
A. P. Poloski

June 2003

Prepared for Bechtel National, Inc.
under Contract 24590-101-TSA-W000-0004

Test Specifications: 24590-WTP-TSP-RT-01-005 and
TSP-W375-01-00002
Test Plans: TP-RPP-WTP-099 and TP-RPP-WTP-066
Test Exceptions: 24590-WTP-TEF-RT-02-081 (AZ101)
24590-WTP-TEF-RT-02-082 (Energetics)
R&T Focus Area: Pretreatment
Test Scoping Statement(s): B-78 and B-86

Battelle – Pacific Northwest Division
Richland, Washington, 99352

Completeness of Testing

This report describes the results of work and testing specified by Test Exceptions 24590-WTP-TEF-RT-02-081 (AZ101) and 24590-WTP-TEF-RT-02-082 (Energetics) Test Specifications 24590-WTP-TSP-RT-01-005 and TSP-W375-01-00002 and Test Plans TP-RPP-WTP-099 and TP-RPP-WTP-066. The work and any associated testing followed the quality assurance requirements outlined in the Test Specifications/Plans. The descriptions provided in this test report are an accurate account of both the conduct of the work and the data collected. Test plan results are reported. Also reported are any unusual or anomalous occurrences that are different from expected results. The test results and this report have been reviewed and verified.

Approved:

Gordon Beeman, Manager
WTP R&T Support Project

Date

Summary of Testing

The U.S. Department of Energy (DOE) intends to vitrify Hanford tank wastes at the River Protection Project-Waste Treatment Plant (RPP-WTP). The wastes will be phase separated in the plant, where solids will be washed, then forwarded for processing into a high-level waste (HLW) fraction, combined with other HLW waste processing streams, and vitrified into a HLW glass. Modeling these waste-processing steps for process optimization and cold commissioning requires using a simulant that accurately reflects the tank waste solids composition and particle size distribution (PSD). Battelle – Pacific Northwest Division (PNWD) tested Hanford Tanks 241-AN-102 (AN-102) and 241-AZ-101 (AZ-101) solids to define better the composition, morphology, and associated PSD. These characterization activities were performed according to Test Exception 24590-WTP-TEF-RT-02-081(AZ101) and 24590-WTP-TEF-RT-02-082 (Energetics). The testing was defined in technical scoping statements B-86 (AN-102) and B-78 (AZ-101) of the Research and Technology Plan.

Objective

The objective of this task was to identify individual phases present in the washed solids sub-samples derived from AN-102 and AZ-101 with scanning electron microscopy (SEM), energy dispersive x-ray spectroscopy (EDS), x-ray diffraction (XRD), infrared spectroscopy (IR), and laser light scattering particle size determination (PSD) to improve simulant development.

Conduct of Testing

Samples from homogenized AN-102 were extracted from the third wash of the solids (Bryan et al. 2002). Samples of blended AZ-101 were provided after phase separation (Urie et al. 2002) and rigorous washing (Geeting et al. 2002). These samples were further divided into sub-samples suitable for examination with SEM, EDS, XRD, IR, and PSD. The high activity of the samples necessitated reducing the sample size to allow examination in the various instruments. The need to reduce sample volume combined with the highly heterogeneous nature of the tank solids, suggests that the samples may not have been representative of the bulk material.

Results and Performance Against Objectives

The phase identifications are summarized in Table S.1. In AN-102, microstructural analysis provided evidence for the presence of zeolitic phases. XRD and SEM-EDS suggest the presence of boehmite (AlOOH) and sodium aluminate (although the Na-Al carbonate phase, dawsonite, cannot be ruled out). The evaporite phases, sodium nitrate ($NaNO_3$) and sodium nitrite ($NaNO_2$), were identified with XRD. Both $NaNO_3$ and $NaNO_2$ precipitated during sample preparation. A number of smaller particles were also found attached to the surface of the bulk material. The AN-102 sample did not have detectable levels of gibbsite. Uranium oxide (possibly schoepite) particles, ranging in size from 1 to 5 µm in diameter, were found in the AN-102 sample. Iron oxide (hematite) and iron chromium nickel oxide (chromite) were observed. A much rarer cerium oxide (possibly cerianite) and yttrium vanadate particles (possibly wakefieldite) were also found in the AN-102 sample.

Table S.1. Phase Identification Results Summary

Element	AZ-101 WS	Size (µm)	AN-102 WS	Size (µm)
Al	Gibbsite	2-3	Boehmite,	ND
Al	Boehmite	ND	Zeolite	5-20
Al	Zr-Fe phase	0.5-2	Na aluminate	<1
Ba	ND	NA	ND	NA
C as TIC	Carbonate	NA	Carbonate	NA
C as TOC	ND	NA	ND	NA
Ca	Calcite	5	Zeolite, calcite	5-20
Cd	Cd-Sn phase	4-8	ND	NA
Ce	ND	NA	Cerianite	10
Cl	ND	NA	ND	NA
Cr	Chromite	ND	Chromite	10
Cu	Fe-Zr phase, chromite	0.5-2	ND	NA
F	ND	NA	ND	NA
Fe	Hematite	1-3	Chromite	10
Fe	Fe-Zr phase	0.5-2	Hematite	NA
K	Mn-clay	0.3-0.5	Zeolite	5-20
La	Fe-Zr phase	0.5-2	ND	NA
Mg	ND	NA	ND	NA
Mn	Mn-clay	0.3-0.5	ND	NA
Mo	ND	NA	ND	NA
Na	$NaNO_3$	NA	Zeolite	5-10
Na	NA	NA	Na aluminate	<1
Nd	Fe-Zr phase	0.5-2	ND	NA
Ni	Fe-Zr phase	0.5-2	Chromite	10
NO_2	$NaNO_3$	NA	$NaNO_3$	NA
NO_3	$NaNO_2$	NA	$NaNO_2$	NA
P	Phosphate	NA	ND	NA
Pb	ND	NA	ND	NA
Pd	ND	NA	ND	NA
Rb	ND	NA	ND	NA
Ru	ND	NA	ND	NA
Si	Fe-Zr phase	0.5-2	Zeolite	5-20
SO_4	Na sulfate	NA	Na sulfate	NA
Sn	Cd-Sn phase	4-8	ND	NA
Sr	ND	NA	ND	NA
Te	ND	NA	ND	NA
Th	ND	NA	ND	NA
U	U(VI)-oxide	5-20	U(VI) oxide	5-10
V	ND	NA	Wakefieldite	5
Y	ND	NA	Wakefieldite	5
Zr	Fe-Zr phase	0.5-2	ND	NA

WS = washed solids, NA = not applicable

ND = not detected

Particle diameter based on SEM observations of individual particles.

Note: Some elements are listed more than once because they were present in more than one phase.

The laser light scattering particle size analysis of the AN-102 washed solids sample indicated that most of the particle volume was particles in the 0.5 to 15 micron range. However, under sonication, the agglomerates appeared to break apart, resulting in a larger volume of smaller-diameter particles. After sonication, most of the particles were between approximately 0.6 and 3.0 μm. The results of the particle size analysis were reasonably consistent with observations made with SEM on the nature of the particles. However, the sample preparation method for microscopy did result in the formation of soft agglomerated particles. Therefore, the SEM images of particles do not represent the anticipated size of the particles during waste processing.

Zeolites were not found in the two samples of AZ-101 solids. Both AZ-101 samples contained boehmite and gibbsite. A number of smaller particles were also found. Calcite was also identified in AZ-101. Uranium oxide (possibly schoepite) particles ranging in size from 5–10 μm to less than 1 μm in diameter were fairly common in the AZ-101 samples. Iron oxide (hematite) and iron chromium nickel oxide (chromite) were observed in both samples. A zirconium iron phase was common. These phases also contained aluminum, lanthanum, and neodynium. This phase may be mixed carbonate-phosphate, according to IR analysis. A manganese-bearing phase was also commonly found in the unwashed AZ-101 sample. Particle size analysis of these AZ-101 samples is described in Urie et al. (2002).

Quality Requirements

PNWD implemented the RPP-WTP quality requirements by performing work in accordance with the quality assurance project plan (QAPjP) approved by the RPP-WTP Quality Assurance (QA) organization. This work was conducted to the quality requirements of NQA-1-1989 and NQA-2a-1990, Part 2.7, as instituted through PNWD's *Waste Treatment Plant Support Project Quality Assurance Requirements and Description* (WTPSP) manual.

All of the instruments used in this study were checked where possible with National Institute of Standards and Technology (NIST) standards, as well as other internal standards, at the time of the analysis. NIST standards were not available for all instrumentation. For example, both the calibration of the infrared spectrometer and x-ray energy dispersive spectrometer was checked with various compounds.

PNWD addressed verification activities by conducting an Independent Technical Review of the final data report in accordance with procedure QA-RPP-WTP-604. This review verified that the reported results were traceable, that inferences and conclusions were soundly based, and the reported work satisfied the Test Plan objectives.

Issues

None.

Contents

Figures

Tables

Abbreviations, Acronyms, and Definitions

BSE	Backscattered electron
DOE	U.S. Department of Energy
EDS	Energy dispersive x-ray spectroscopy
FWHM	Full width half maximum
HLW	High level waste
IR	Infrared spectroscopy
IRC	Independent Review Committee
ISMS	Integrated Safety Management System
JCPDS	Joint Committee of Powder Diffraction Standard
NIST	National Institute for Standards and Technology
OM	Optical microscopy
PI	principal investigator
PNWD	Pacific Northwest Division (Battelle)
PSD	Particle size distribution
QA	Quality Assurance
RPL	Radiochemical Processing Laboratory
SAL	Shielded Analytical Laboratory
SEM	Scanning electron microscopy
TIC	Total inorganic carbon
TOC	Total organic carbon
UPA	Ultrafine particle analysis
WTP	Waste Treatment Plant
XRD	X-ray diffraction

Definitions

Acicular	Crystals with an elongated or needle-like form
Agglomerate	Particles in a dispersed system associated into larger structures
Amorphous	Non-crystalline substance that does not produce an XRD pattern
Botryoidal	A globular growth of minerals
Bremmstrahlung	X-ray background signal observed in EDS produced by electrons slowing down as they pass through the sample.
Dissolved solids	Soluble solids; those remaining after complete drying of a liquid at 105°C. Typically reported as wt%. During drying, most mass loss is due to water, but other volatile components (e.g., organics) may also be lost.
d-spacings	Lattice spacings obtained with XRD
Crypto-crystalline	Only partly crystallized but completely amorphous.
Euhedral	Well-formed crystal with regular shape
Floc	Assemblies of aggregates

Gel	A semi-solid colloidal product
Undissolved solids	Solids excluding all interstitial liquid. This can be thought of as the solids left if all the supernatant and associated dissolved solids could be drained from the bulk slurry. The undissolved solids will generally include some materials that can be washed or dissolved during pretreatment.
R	The correlation coefficient between measured and predetermined values.
Regression Line	The relationship between x and y is given by: $y = mx + c$; this is known as the regression line of y on x.
Spectrum	Refers to a plot of measured signal intensity versus energy.
Total solids	Solids remaining after drying to a stable mass at 105°C; includes dissolved and undissolved solids.

Mineral Names and Formulae

Analcime	$Na(AlSi_2O_6){\bullet}H_2O$
Asbolane	$(Co,Ni)_{1-y}(MnO_2)_{2-x}(OH)_{2-2y+2x}{\bullet}nH_2O$
Bayerite	β- $Al(OH)_3$
Birnessite	$Na_4Mn_{14}O_{27}{\bullet}9H_2O$
Boehmite	γ–AlOOH
Calcite	$CaCO_3$
Cancrinite	$(Na,Ca,K)_7Al_6Si_6O_{24}(CO_3)_{1.6}{\bullet}2.1H_2O$
Cerianite	CeO_2
Chromite	$FeCr_2O_4$
Clinoptilolite	$(Na, K, Ca)_{2-3}Al_3(Al, Si)_2Si_{13}O_{36}{\bullet}12H_2O$
Corrundum	Al_2O_3
Birnessite	$Na_4Mn_{14}O_{27}{\bullet}9H_2O$
Dawsonite	$NaAl(CO_3)(OH)_2$
Diaspore	β- AlOOH
Gibbsite	β- $Al(OH)_3$
Goethite	FeOOH
Mahlmodite	$FeZr(PO_4){\bullet}4(H_2O)$
Nitratite	$NaNO_3$
Norstrandite	β-$Al(OH)_3$
Hematite	Fe_2O_3
Heulandite	$(Ca,Na)_{2-3}Al_3(Al,Si)_2Si_{13}O_{36}{\bullet}12H_2O$
Philipsite	$(K_2Na_2Ca)(Al_2Si_4)O_{14}{\bullet}4\text{-}5H_2O$
Powellite	$CaWO_4$
Rutherfordine	UO_2CO_3
Schoepite	$UO_3{\bullet}2H_2O$
Sodalite	$Na_4Al_3Si_3O_{12}Cl$
Strontianite	$SrCO_3$
Wakefieldite	YVO_4

Uraninite	UO_2

Units

at%	Atomic percent
°C	degrees centigrade
cm^{-1}	wavenumbers
eV	electron volt
g	gram
keV	kilo-electron volt
L	liter
μg	microgram
μm	micrometer
M	molarity, mole/liter
m	meter
mg	milligram
mL	milliliter
nm	nanometer
vol%	volume percent
wt%	weight percent

1.0 Introduction

This report describes the identification of phases in the washed solids from actual sludge taken from a composite sample of Tanks 241-AN-102 (AN-102) and 241-AZ-101 (AZ-101) waste.[a] The U.S. Department of Energy (DOE) intends to vitrify Hanford tank wastes at the River Protection Project-Waste Treatment Plant (RPP-WTP). The wastes will be phase separated in the plant, where solids will be washed then forwarded for processing into a high-level waste (HLW) fraction, combined with other HLW waste processing streams, and vitrified into a HLW glass. Modeling these waste processing steps for process optimization and cold commissioning requires using a simulant that accurately reflects the tank waste solids composition and particle size distribution (PSD). Battelle – Pacific Northwest Division (PNWD) tested Hanford Tanks AN-102 and AZ-101 solids to define better the solids composition, morphology, and associated PSD. These characterization activities were performed according to Test Exception 24590-WTP-TEF-RT-02-081(AZ101) and 24590-WTP-TEF-RT-02-082 (Energetics), Test Specifications 24590-WTP-TSP-RT-01-005 and TSP-W375-01-00002 and Test Plans TP-RPP-WTP-099 Rev. 1, AZ-101 HLW Filtration and Caustic Leaching Plan Using the CUF and TP-RPP-WTP-066 Rev. 0, Energetics and Gas Generation Tests. The testing was defined in technical scoping statements B-30 (AN-102) and B-78 (AZ-101) of the Research and Technology Plan.

Work described in this report is being conducted at Battelle – Pacific Northwest Division (PNWD) for the DOE RPP-WTP. Two test exceptions covered the solids characterization work. The Test Plans were TP-RPP-WTP-099, TSS B-78; and TP-RPP-WTP-066, TSS B-86.

The objective of this work was to determine the structure, composition, and size distribution of individual phases in the washed solids sample. The techniques used were x-ray diffraction (XRD), scanning electron microscopy (SEM) with x-ray energy dispersive spectroscopy (EDS), and laser light scattering particle size determination (PSD).

Phase analysis was done by using SEM, EDS, IR, and XRD data from the samples and comparing the results with those reported in the literature. However, there are several limitations in this methodology. First, XRD highlights only the crystalline phases, in particular, the phases that scatter strongly [i.e., high atomic number (Z) crystalline phases]. In addition, the peak intensities cannot be used as a quantitative indication of phase concentration. The SEM tended to examine much smaller size samples than the XRD due to sample handling issues. SEM images are created by rastering a focused electron probe across a sample while simultaneously measuring various secondary and backscattered electron signals as a function of beam position. Elastic and inelastic scattering spread the incident electron beam within the sample yielding an interaction volume, the dimensions of which depend on the electron beam energy and sample composition (i.e., atomic number) rather than the focused probe size (Seaman 2002). As the energy of the beam increases, the interaction volume also increases. When electrons of adequate energy hit the sample, characteristic x-rays indicative of elemental composition (i.e., atomic number) are produced at intensities proportional to the mass concentration of the given element within the interaction volume. To generate an x-ray spectra, the electron beam energy must be greater than the characteristic x-ray energy of the element of interest. For example, to excite the Zr-K line, beam energy of 20 keV is

---

[a] Hanford waste tanks are designated with the prefix 241-. In this report, as in common usage, the prefix is omitted.

required. However, as the beam energy increases, the beam excitation volume increases, reducing the spatial resolution. In this study, the beam energy was held at 20 keV for all analyses.

The SEM investigation used backscattered imaging that highlights the high atomic number particles. The EDS used for compositional analysis has a minimal spatial resolution of about $1 \mu m^3$ and is unable to detect any elements lighter than carbon. In general, elements below 1 wt% in any analyzed region cannot be detected, and overlap problems can further reduce detection limits. Nearly all the data collected have been included in this report, including listings of d-spacings from XRD runs. This allows the reader to recheck the data analyses and interpretations themselves. Most phase identifications described in this report are based on interpretations of the available data. With the instrument techniques used and the nature of the tank waste samples, we cannot be completely confident that any phase identification is absolutely correct.

All the electron beam and x-ray techniques described here are unable to readily observe organic phases. These are thought to be an important component of AN-102 tank waste. Infrared microscopy and micro-Raman spectroscopy might be a promising technique to use in future investigations to address this issue.

The particle size distribution of solids sample from AN-102 labeled as AN-102 WS9 is described in this report. A Microtrac X-100 particle analyzer and a Microtrac ultrafine particle analyzer (UPA) were both used to measure the particle size distribution of the waste samples. The Microtrac X-100 particle analyzer measures particle diameter by scattered light from a laser beam projected through a stream of the sample particles diluted in a suspending medium. The amount and direction of light scattered by the particles is measured by an optical detector array and then analyzed to determine the size distribution of the particles. This measurement is limited to particles with diameters between 0.12 and 700 μm. The Microtrac UPA measures particle diameter by Doppler shifted scattered light. This method is limited to particles with diameters between 3 nm and 6.5 μm. Particle size analysis for AZ-101 samples is reported in Urie et al. (2002).

2.0 Experimental

The objective of this study was to identify individual phases present in the washed solids subsamples derived from AN-102 and AZ-101 with SEM, EDS, XRD, IR, and PSD to assist in the development of a tank waste simulant.

2.1 Sample History

Washed solids from Tank AN-102 and washed and unwashed solids from AZ-101 were prepared for micro-analytical characterization at the RPL in the Hanford 300 Area. The washing steps simulated the expected pretreatment processing for these tanks. Before the micro-analytical work was started, both AN-102 and AZ-101 samples had been homogenized, and subsamples had been pulled for further analytical work.

2.1.1 AN-102 Solids

The history of the AN-102 sample used in this study is described in Bryan et al. (2002). Figure 2.1 shows where the samples for this characterization work were obtained and their relation to other subsamples of AN-102. The shaded regions refer to steps taken in this investigation. Bryan et al. (2002) reported that samples were generated by homogenizing several of the 30 AN-102 samples that were sent to PNWD in August 2000. The homogenized sample (2129.51 g) went through three washing steps with 0.01 M NaOH. The solids and the wash solution were contacted for one hour with agitation and allowed to settle. Nominally 701.0 g of solids were recovered. This third washed solids sample was used in gas generation (Bryan et al. 2002), and a subsample of about 5g was provided for microcharacterization studies. This sample was dried in an oven at 60°C overnight. Approximately 1-2 mg was used for XRD and 0.5-0.1 mg for SEM studies.

2.1.2 AZ-101 Solids

Two samples of AZ-101, washed and unwashed, solids were examined. The material preparation and homogenization of AZ-101 and the details of the unwashed sample, including particle size measurements, are described by Urie et al. (2002). The history of the washed sample processing of the AZ-101 subsamples is described by Geeting et al. (2002). The analyzed washed solids sample is identified as AZ6 in flow charts.

Samples for XRD were prepared in the Shielded Analytical Laboratory (SAL). An aliquot of the sample was deposited on a clean glass slide. The slide was transferred to the XRD laboratory and run on the Scintag instrument. Samples for SEM needed to be further reduced in size owing to restrictions on handling and transporting these samples in the microscopes.

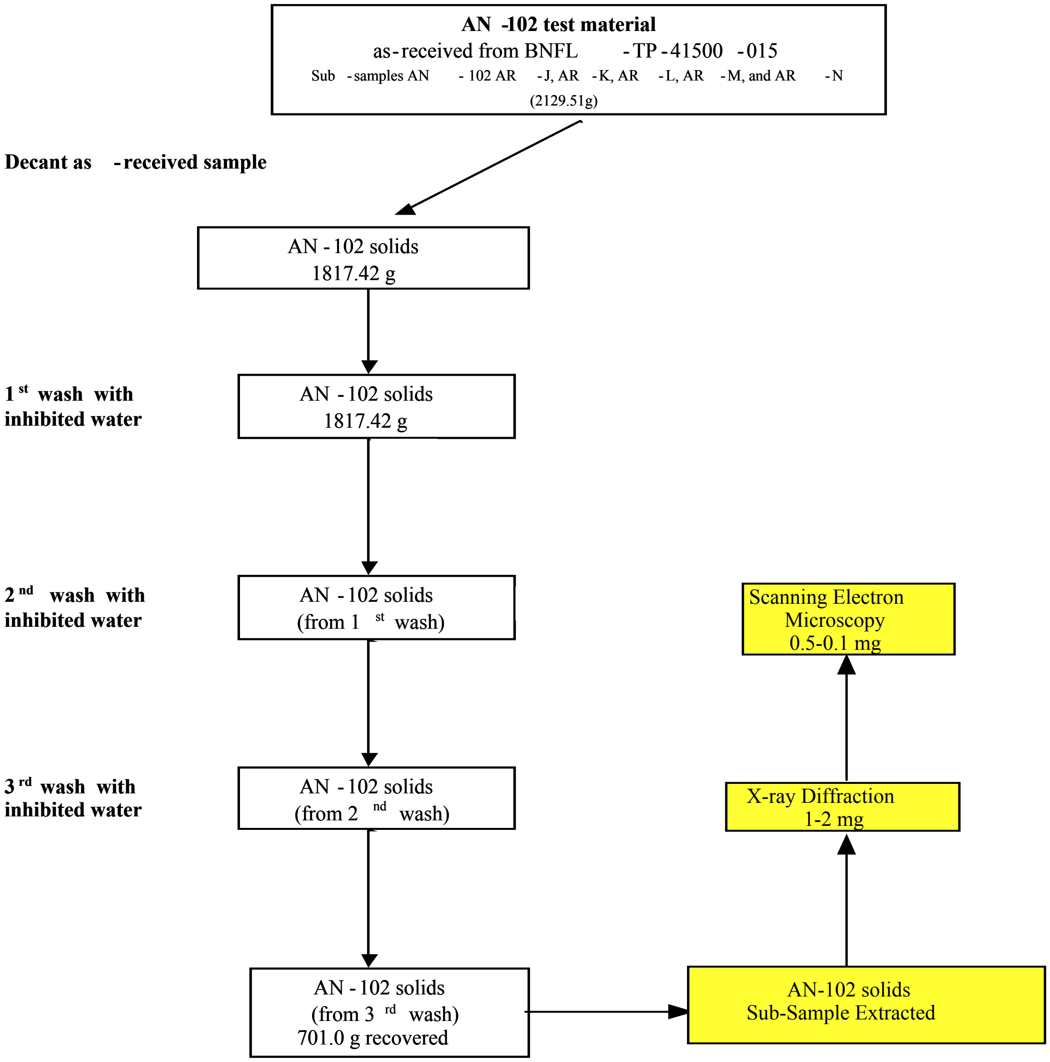

Figure 2.1. Flow Chart Describing Origin of AN-102 Washed Solids (adapted from Bryan et al. 2002)

2.2 Composition of Solids

Total chemical analyses of the AN-102 and AZ-101 washed and unwashed solids are reported in Bryan et al. (2002) and Urie et al. (2002). In Tables 2.1 and 2.2, only the major components are reported in atom percent (at%). As the SEM-EDS detection depends on atom concentration, this is more useful for interpreting the microscopy analyses. Comparison of the total chemical analyses with the analyses from XRD, SEM, and EDS can be used to determine how representative the microcharacterization has been of the bulk material.

In AN-102 there are high concentrations of Al, F, N, and Na (of the EDS detectable elements). The minor components include Cl, Ru, Mn, Cr, Fe, and U. In AZ-101, the major EDS detectable components are Al, F, N, S, Na, Si, Fe, and Zr. Minor components are Mg, P, K, Ca, Cr, Ni, Mn, La, Cd, and U.

Table 2.1. Composition of AN-102 Washed Solids reported in atomic % (at%) (adapted from Bryan et al. 2002)

Element/Species	**Washed Solids**	**Element/Species**	**Washed Solids**
Al	18.153%	Oxalate	7.443%
Br	0.054%	Pb	0.040%
Ca	0.079%	P	0.033%
Cl	0.356%	Ru	1.859%
Cr	0.751%	Si	0.077%
F	4.589%	Sn	0.012%
Fe	0.469%	S	0.028%
K	0.100%	U	0.649%
Mn	0.103%	V	0.026%
Na	60.158%	W	0.000%
Ni	0.007%	Y	0.048%
N	4.962%	Zr	0.002%

Table 2.2. Composition of Washed and Unwashed AZ-101 Solids reported in atomic % (at%) (adapted from Urie et al. 2002)

Element/Species	**Unwashed**	**Washed**	**Element/Species**	**Unwashed**	**Washed**
Al	43.423%	52.977%	Na	26.799%	16.043%
Ba	0.031%	0.038%	Nd	0.075%	0.093%
C as TIC(a)	6.020%	5.749%	Ni	0.407%	0.504%
C as TOC(a)	0.589%	0.286%	N	2.509%	0.760%
Ca	0.517%	0.639%	P	0.498%	0.557%
Cd	0.358%	0.443%	Pb	0.020%	0.025%
Ce	0.018%	0.023%	Pd	0.008%	0.009%
Cl	0.027%	0.009%	Rb	0.026%	0.032%
Cr	0.133%	0.117%	Ru	0.098%	0.121%
Cu	0.032%	0.040%	Si	1.170%	1.422%
F	1.865%	1.932%	S	2.155%	1.863%
Fe	10.320%	12.817%	Sr	0.035%	0.044%
K	0.309%	0.325%	Te	0.013%	0.016%
La	0.111%	0.138%	Th	0.004%	0.005%
Mg	0.156%	0.193%	U	0.133%	0.165%
Mn	0.232%	0.287%	Y	0.011%	0.014%
Mo	0.013%	0.013%	Zr	1.843%	2.283%

(a) TIC = total inorganic carbon.

(b) TOC = total organic carbon.

2.3 Microstructural Analysis of Subsamples

Samples for SEM (<2 mg) and XRD (20–50 mg) were produced in the Shielded Analytical Laboratory (SAL). For SEM, a small sample aliquot was placed on a clean glass slide in the SAL and transferred to another laboratory fume hood. Sub-samples were extracted from the larger sample and deposited on a sticky carbon tape mounted on a SEM stub. The SEM sample was examined in a JEOL840 (JEOL USA Inc., Boston, MA) SEM equipped with a backscattered electron detector and an Oxford (Oxford Instruments X-ray Technologies, Inc., Santa Cruz, CA) x-ray EDS system in the 326 Building. Because of the carbon coating used to make the sample conductive, the detector was unable to detect elements lighter than carbon.

2.3.1 Scanning electron microscopy

All SEM images were obtained in backscattered electron imaging mode with a 20 keV electron beam. This is sometimes a less effective method for obtaining morphological information on many of the phases; however, it is the preferable technique for finding different phases and obtaining EDS data rapidly over a wide energy range. Because the sample was not a polished flat section, it can be unreliable to extract quantitative data from these types of analyses. The SEM sample volume was significantly smaller than the XRD sample size due to radiological issues. Initial samples of AZ-101 were prepared for SEM in the SAL; however, the samples were too radioactive for transfer to Building 326. Using a fine needle, we transferred a small quantity of the sample intended for SEM onto another SEM mount. This reduced the radiation level associated with the sample by about 100 times; however, it similarly reduced the sample size and possibly made this new sample much less representative of the bulk homogenized sample. Because the intention of this study was to identify phases rather than quantify the amount of each phase, the representativeness of samples was not considered a critical issue. The sample was transported to the SEM in Building 326 and examined in the JEOL840 SEM.

The SEM magnification scale was calibrated with two National Institute for Standards and Technology (NIST) traceable standards (NIST-4202A and NIST-4250A). Particles from NIST-4202A containing 2.013±0.025 µm polymeric spheres and NIST-4250A containing 50.4±1.0 µm polymeric spheres were placed on a SEM stub, carbon coated, and examined. The NIST standards were similar to those used to check the light scattering equipment. The SEM images of the spheres are shown in Figure 2.2. In both cases, the SEM magnification was within acceptable tolerances. For NIST-4202A, dimensions of 2.045, 2.122, and 1.89 µm were obtained. The SEM image of the particles in Figure 2.2a does not show the complete spheres at this magnification and image contrast range. The polymeric spheres in NIST-4202A did not appear to be perfectly spherical. For NIST-4250A, dimensions of 46.85 and 48.47 µm were obtained. The errors in the SEM magnification were therefore estimated to be <10%.

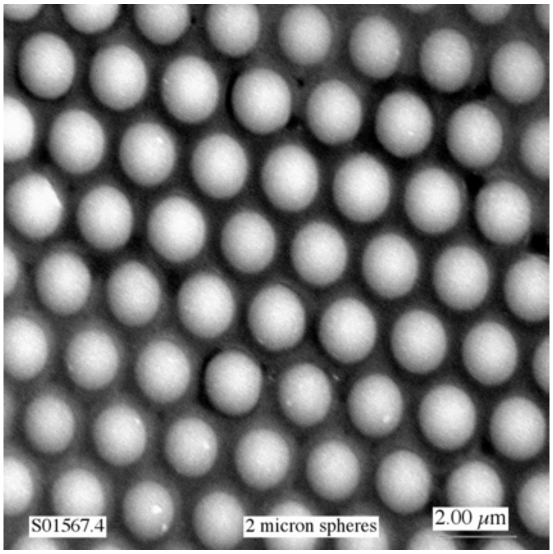

Figure 2.2a. NIST-4202A Polymeric Spheres

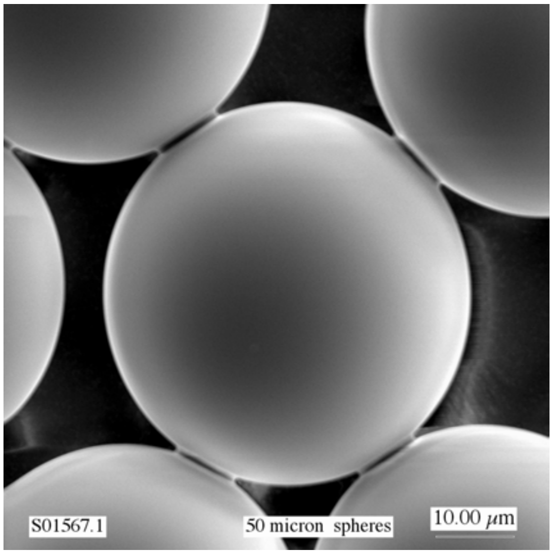

Figure 2.2b. NIST-4250A Polymeric Spheres

2.3.2 X-ray energy dispersive spectroscopy

The EDS system was calibrated with known compounds of $SrCO_3$ and $NaNO_3$. These were also analyzed with XRD (see Section 2.3.3). In Figure 2.3, energy positions of peaks measured on the EDS system have been compared with literature values. The agreement between literature and experimental values was excellent, demonstrating that the system was calibrated correctly for analyzing characteristic x-rays at both low and high energies.

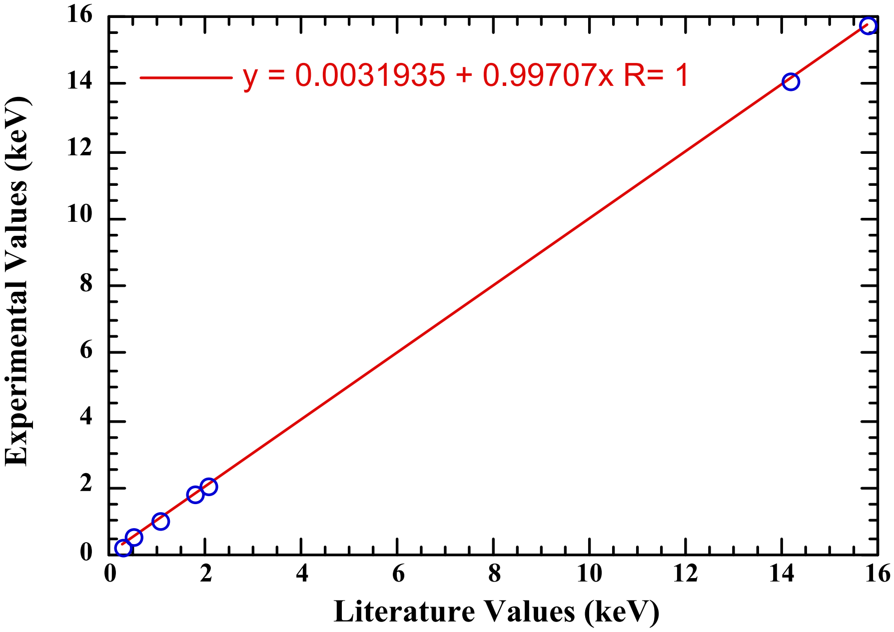

Figure 2.3. Calibration Check of EDS System

A comparison of literature energy x-ray line positions was made against experimentally derived values from a carbon-coated $SrCO_3$ and $NaNO_3$ sample with the JEOL 840 EDS system. The correlation coefficient (R) is 1.00 for the JEOL 840 Oxford EDS detectors. The error in the peak energy assignments was estimated to be <1%. A low energy peak was observed in most EDS spectra taken in this study. This is a detector artifact and should be ignored.

2.3.3 X-ray diffraction

XRD was performed with a Scintag (ThermoARL, Germany) diffractometer. The XRD samples of the tank waste solids were prepared in the SAL hot cells. The samples were dried at 90°C overnight, crushed and mixed with colloid ion, and deposited onto a clean glass slide. The samples were often covered by the dissolved solids, sodium nitrite, and nitrate phases that formed by evaporation on the slide. The XRD sample preparation exacerbated evaporite formation. The evaporites XRD signal tended to mask the other phases present. A NIST traceable internal standard, corundum (Al_2O_3), was run. The accuracy of the XRD system was tested by running two samples (SR-1 and SR-2) containing $SrCO_3$ (strontianite) and $NaNO_3$ (nitratite) (see Figure 2.4). These phases were chosen for calibration because they are similar to the phases observed in the tank samples. The agreement between literature values for $NaNO_3$ and $SrCO_3$ with the experimentally obtained data was excellent. All XRD slides were transferred to the XRD lab and run for eight hours (step size was 0.02° with 20-second dwell time). The data were analyzed using the International Centre for Diffraction Data (JCPDS) databases. The correlation coefficients were close to 1.00 in SR-2 and SR-1. The errors in XRD measurements are estimated to be <0.5%.

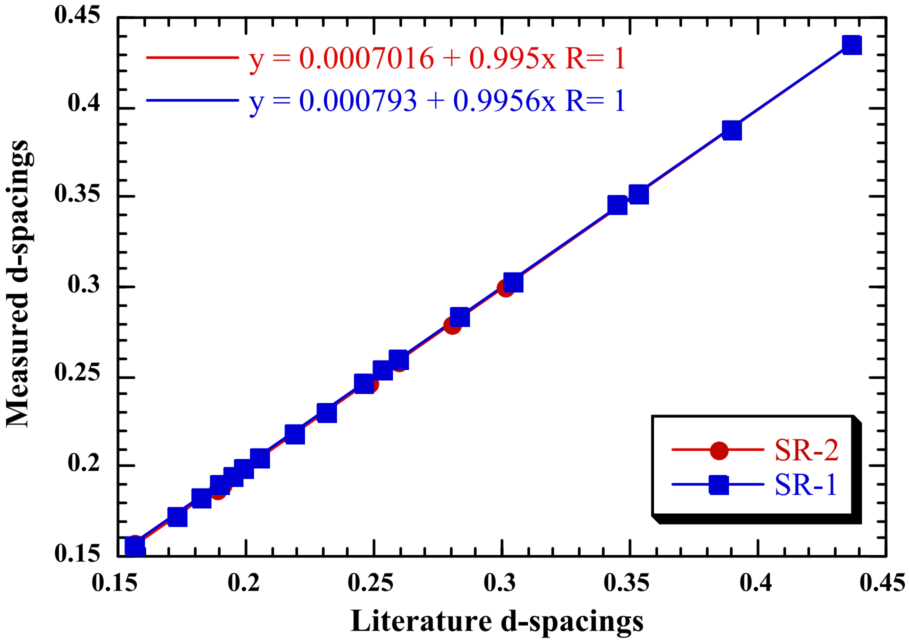

Figure 2.4. Plot Showing Accuracy of XRD Analysis on the Scintag Instrument

2.3.4 Infrared spectroscopy

Infrared spectroscopy was applied to Hanford waste tank simulants by Johnston et al. (2002) to determine the nature of alumina species in strongly alkaline solutions. The technique is effective at identifying the presence of carbonate, nitrate, and nitrite groups as well as organics that may be present. The entire scan might also serve as a fingerprint for comparing simulants and actual wastes. Possible components in the AZ-101 washed solids and a series of standard samples were identified using infrared spectroscopy. The samples were mixed at various concentrations with vacuum-dried potassium bromide. Pellets were made of these mixtures and spectral data acquired on a Nicolet (ThermoNicolet, Madison, WI) 750 infrared spectrometer. For testing the system, a spectrum of a sample containing $SrCO_3$ and $NaNO_3$ was examined. The IR analysis without spectra from the pure phases can be difficult to interpret. From Figure 2.5, it appears that the carbonate is bound to Sr in a unidentate (C_s) fashion because the splitting near 1400 cm^{-1} is around 100 cm^{-1}. Bidentate coordination (C_{3v}) usually causes larger splitting, on the order of 200-300 cm^{-1}, as the bonding becomes increasingly covalent.

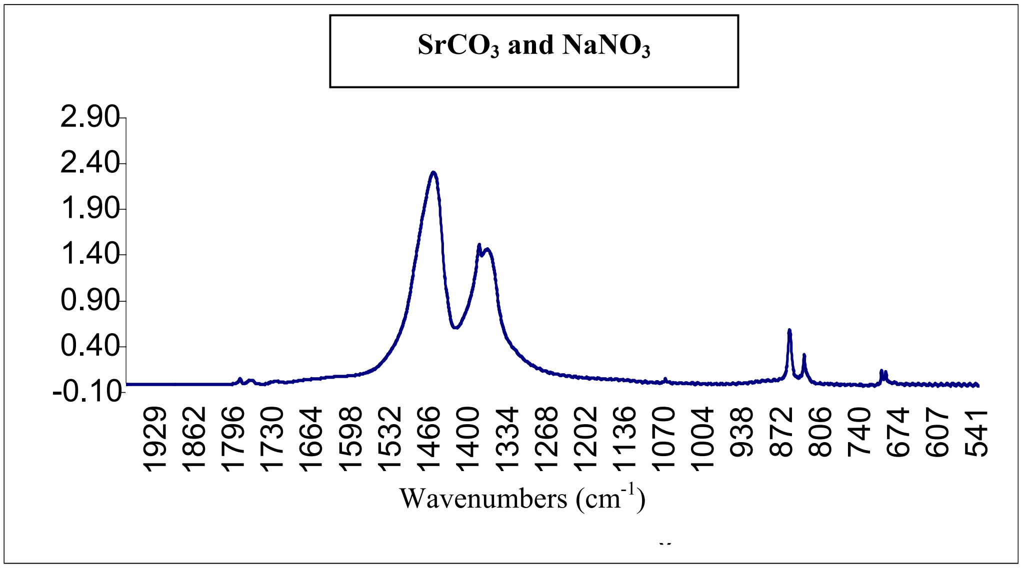

Figure 2.5. Infrared Spectrum of Sample Containing $SrCO_3$ and $NaNO_3$

2.3.5 Particle size analysis

The Microtrac (Microtrac Inc., Clearwater, FL) X-100 particle analyzer measures particle diameter by scattered light from a laser beam projected through a stream of the sample particles diluted in a suspending medium. For the tank waste solids, the suspending medium composition is shown in Table 3.2. The amount and direction of light scattered by the particles is measured by an optical detector array and then analyzed to determine the size distribution of the particles. This measurement is limited to particles with diameters between 0.12 and 700 µm. The Microtrac (Microtrac Inc., Clearwater, FL) Ultrafine Particle Analyzer (UPA) measures particle diameter by Doppler shifted scattered light. This method is limited to particles with diameters between 3 nm and 6.5 µm. The refractive index of the medium was assumed to be 1.33 and that of the particles 1.50. This is a reasonable value for many of the types of phases (i.e., $NaNO_3$ and Al_2O_3) expected in the samples.

The particle size distribution of the AN-102 washed solids sample was measured in the Microtrac X-100 at a flow rate of 40 mL/s. The flow rate was then increased to 60 mL/s and the particle size distribution measured. The sample was then sonicated with 40-W ultrasonic waves for 90 seconds at a flow rate of 60 mL/sec and the particle size distribution measured. Finally, the sample was sonicated a second time with 40-W ultrasonic waves for 90 seconds at a flow rate of 60 mL/sec and the particle size measured. Analyses were performed in triplicate on each sample under all flow/sonication conditions. The average of these triplicate measurements is reported in this document.

For the UPA instrument, no sonication or flow options are available. Therefore, the sample is placed in the instrument and the measurements are performed on the as-received, stationary material.

The performance of both instruments was checked against a range of NIST traceable standards from Duke Scientific Corporation. These standards are polystyrene microspheres dispersed in a 1 mM KCl solution. The standards were run prior to analyzing the sample and were the same standards used as a calibration check for the SEM magnification. Results from these standard tests are presented in Figures 2.6a through h. The percentile data shown in the table represent the given percent of the volume (or mass if the specific gravity for all particles is the same) that is smaller than the indicated particle size. The mean diameter of the volume distribution represents the centroid of the distribution and is weighted in the direction of larger particles. The results were within 10% of the NIST traceable values.

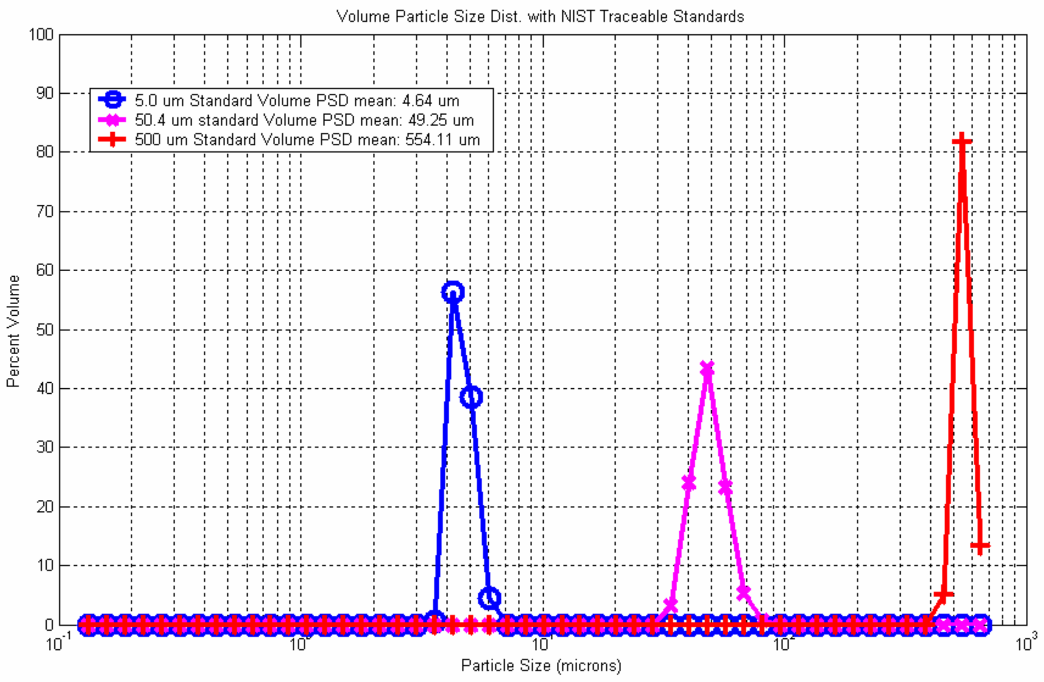

Figure 2.6a. X-100 Calibration Standards on a Volume Basis - Differential

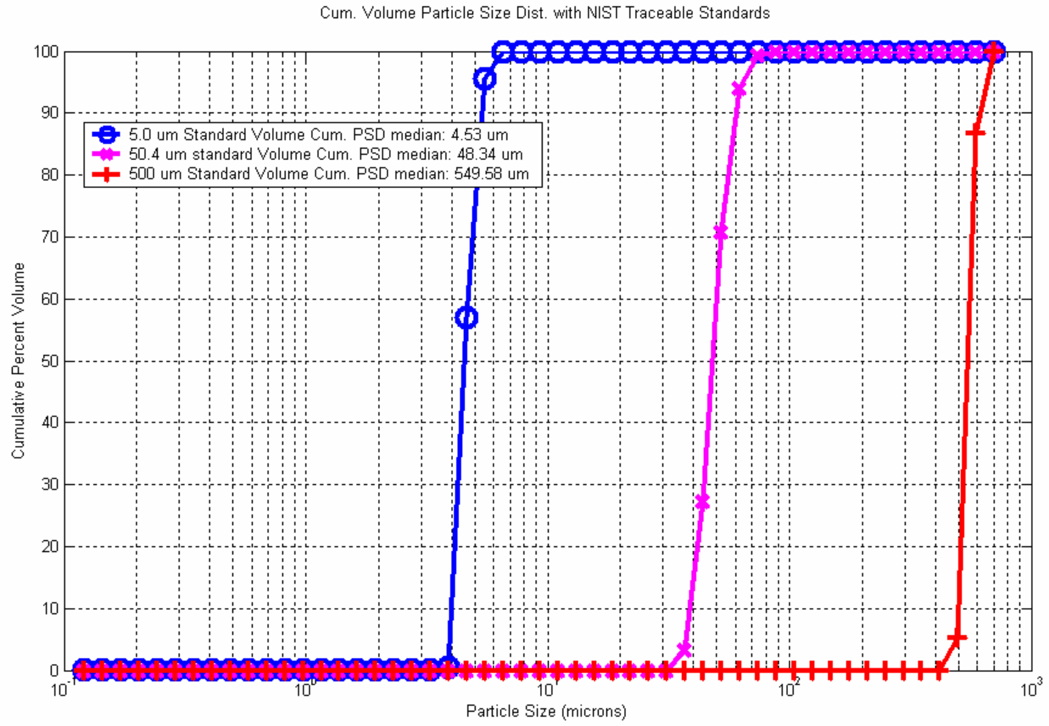

Figure 2.6b. X-100 Calibration Standards on a Volume Basis - Cumulative

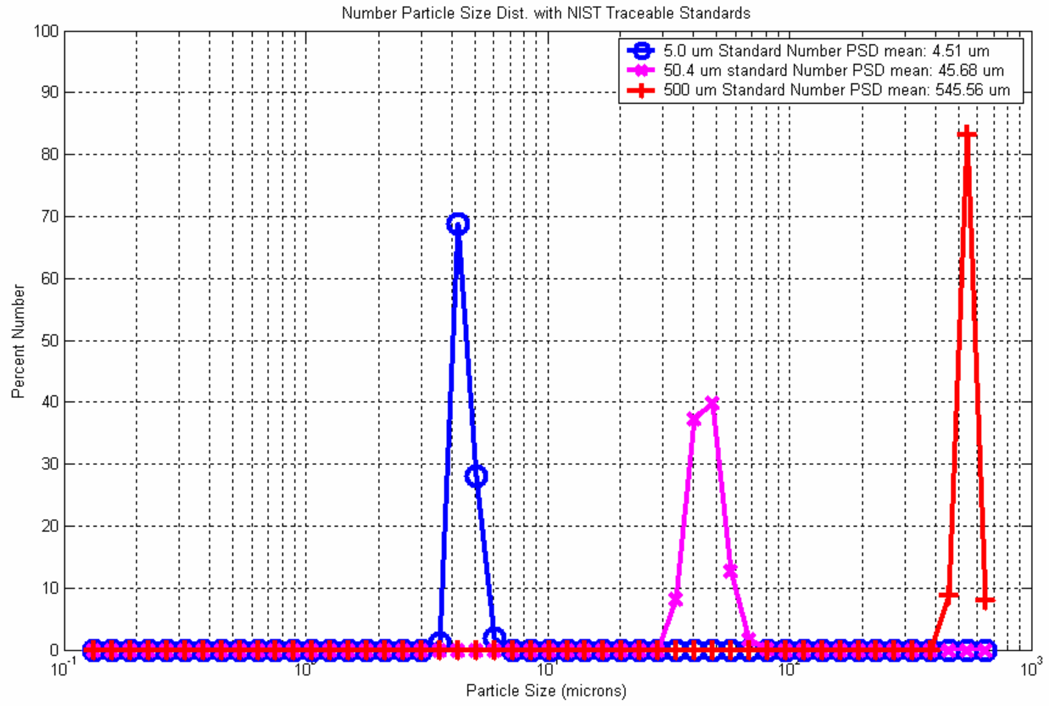

Figure 2.6c. X-100 Calibration Standards on a Number Basis - Differential

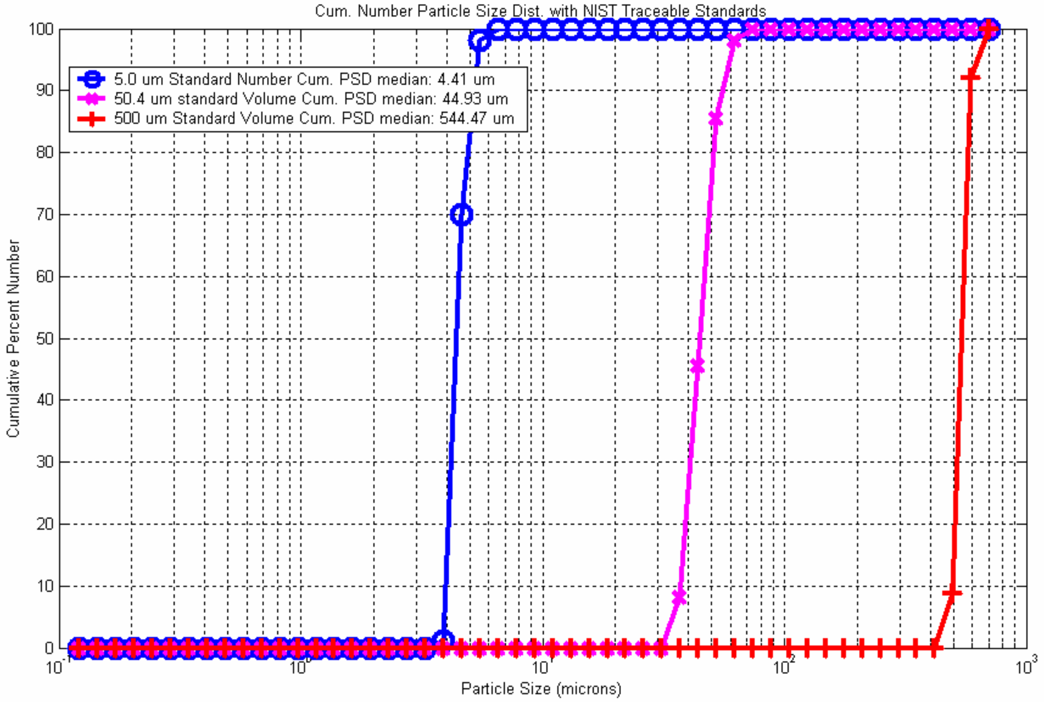

Figure 2.6d. X-100 Calibration Standards on a Number Basis - Cumulative

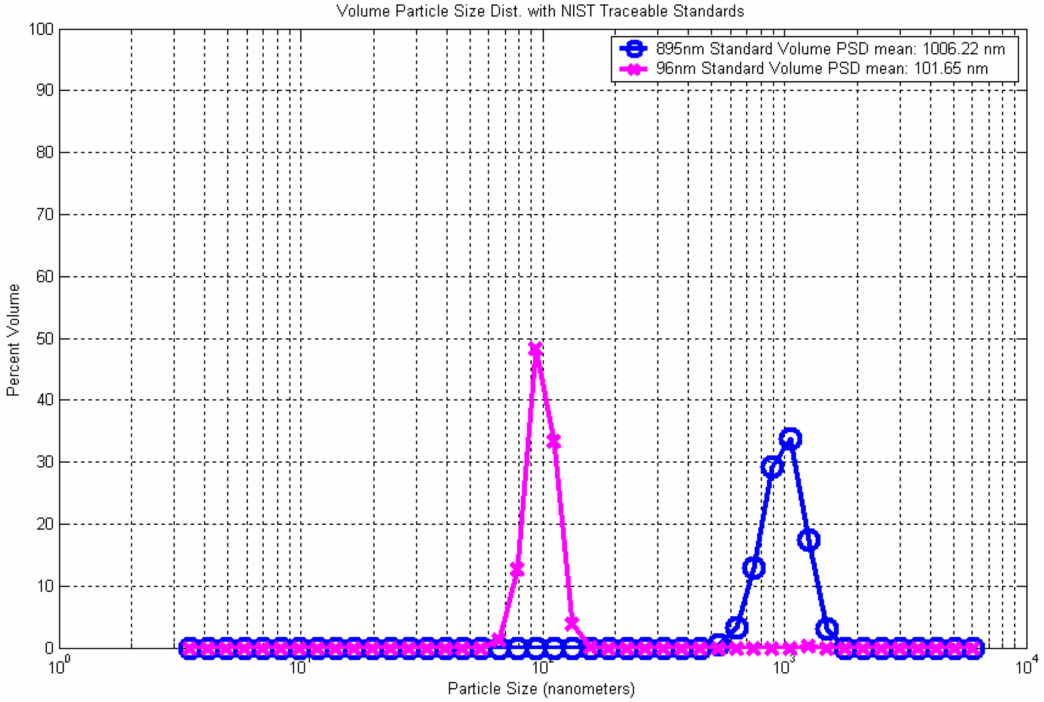

Figure 2.6e. UPA Calibration Standards on a Volume Basis - Differential

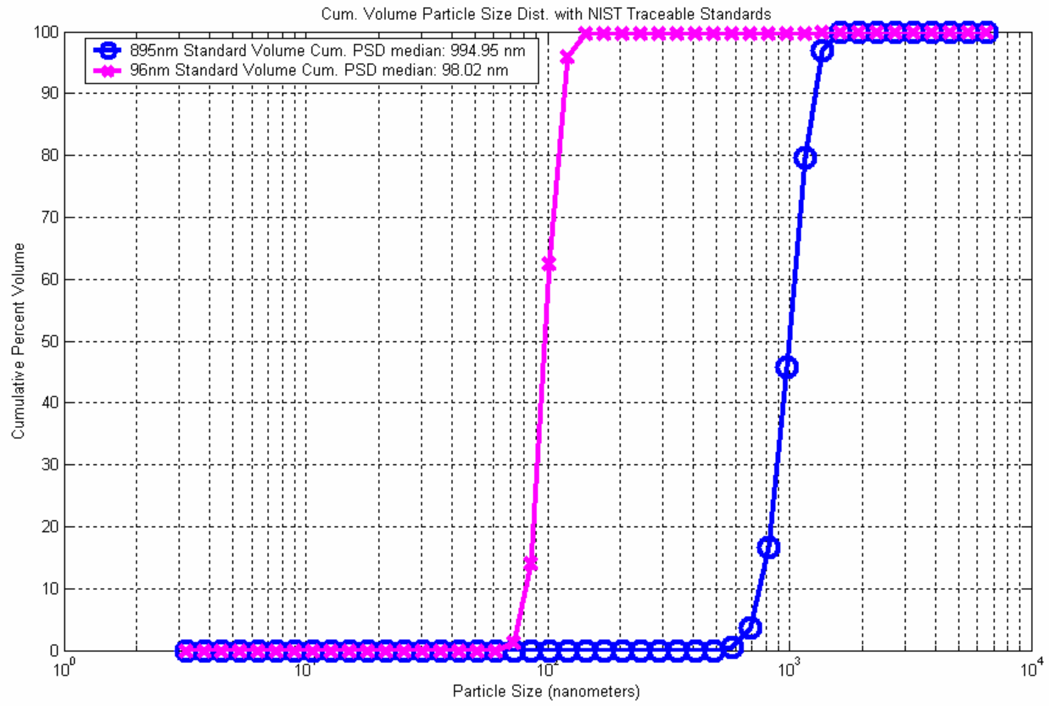

Figure 2.6f. UPA Calibration Standards on a Volume Basis - Cumulative

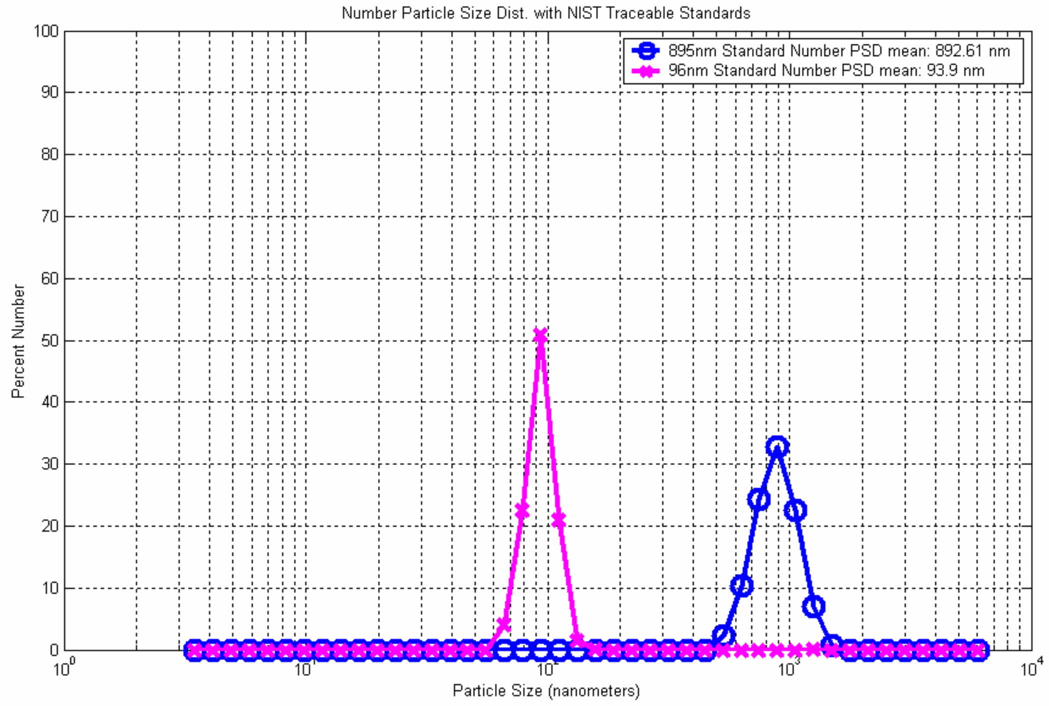

Figure 2.6g. UPA Calibration Standards on a Number Basis - Differential

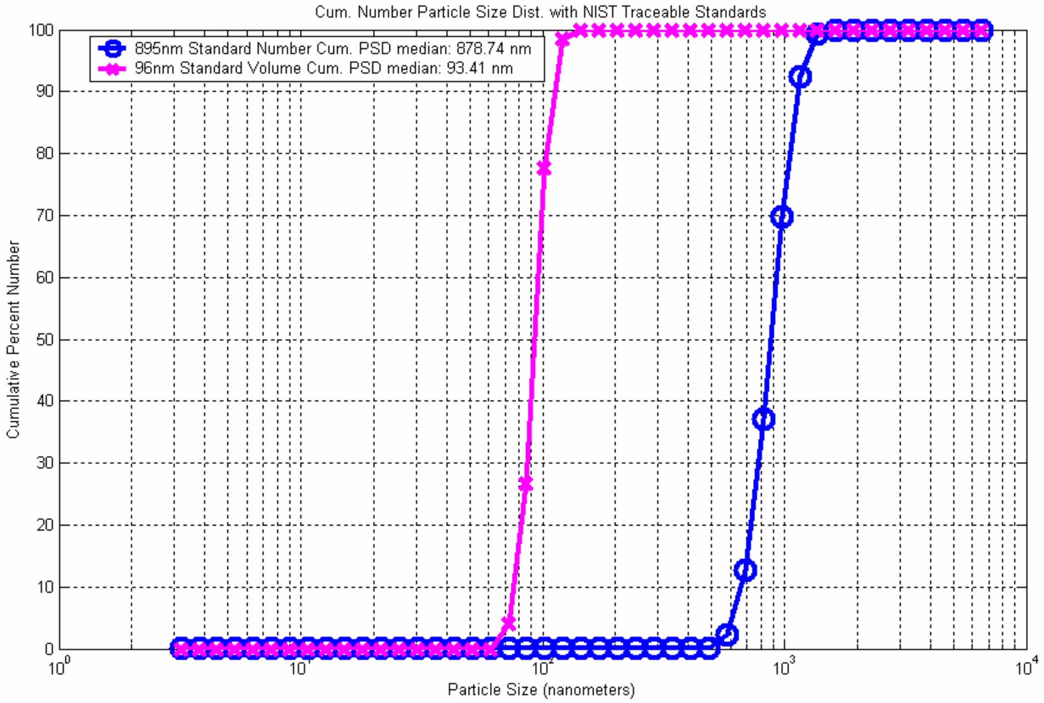

Figure 2.6h. UPA Calibration Standards on a Number Basis - Cumulative

3.0 Analysis of Washed AN-102 Solids

3.1 Scanning Electron Microscopy of AN-102 Washed Solids

The results presented in this section were obtained by inspecting a number of particles found on the SEM mount. Particles were selected for analysis on the basis of backscattered contrast, morphology differences, and relative quantity.

Most of the sample had similar contrast and morphology and contained oxygen, aluminum, and sodium as major components (see Figure 3.1). Minor constituents in this phase include chlorine, sulfur, chromium, and iron. It is not possible to determine the carbon content of any phase accurately because the sample was coated with carbon; however, based on the chemical analysis, carbon is a major component in the washed solids. Depending on the size of the area analyzed, the carbon signal will vary. As the probed area increases, the carbon signal also increases. Figures 3.2a and b show the approximate size of the entire sample examined. Toward the periphery of this larger mass, zeolitic particles (see Figures 3.3a through c) were observed. Small crystallites were found on the surface of the larger zeolite particles, but these remain unidentified. The sample consisted of a matt of a sodium-aluminate phase.

The initial SEM analysis of these zeolitic particles indicated the presence of both potassium and calcium alumino silicates. These were isolated lying on top of the major sodium-aluminate phase. Based on their euhedral form, these were most likely crystalline. In contrast, the sodium aluminate matt looked either amorphous or crypto-crystalline. No larger single-crystal precipitates were found with the sodium aluminate composition.

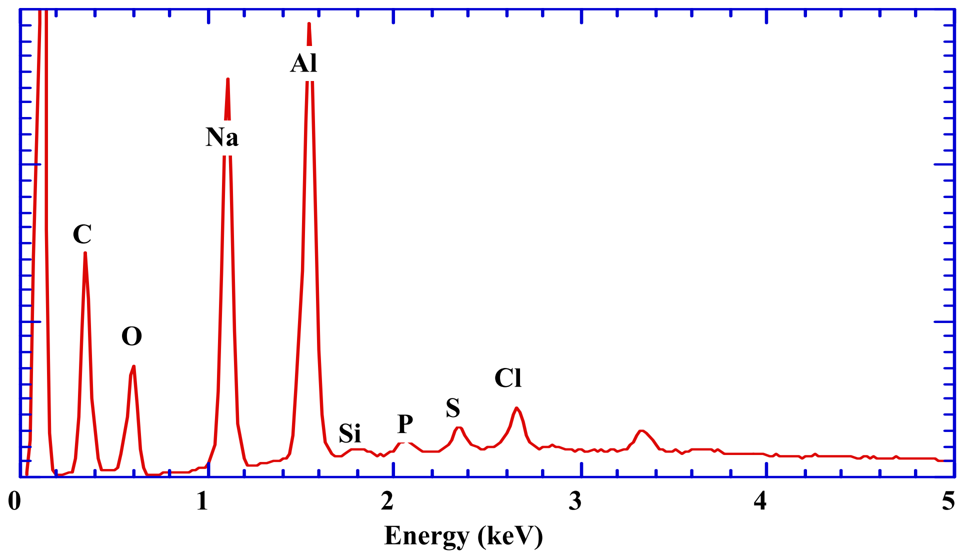

Figure 3.1. X-Ray Energy Dispersive Spectrum of Major Phase in AN-102; the carbon signal on this phase is high relative to most other spectra collected because of the area examined. The low energy peak is an artifact from the detector.

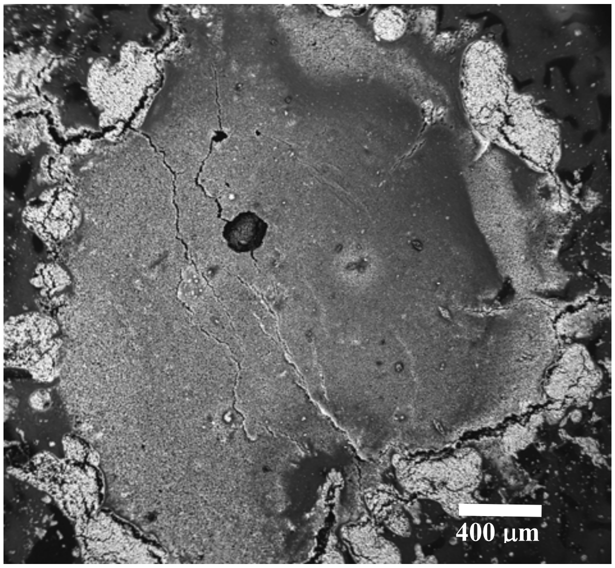

Figure 3.2a. Low-Magnification SEM/BSE Image of Sample AN-102. This phase consisted mainly of sodium and aluminum with an almost gel-like consistency.

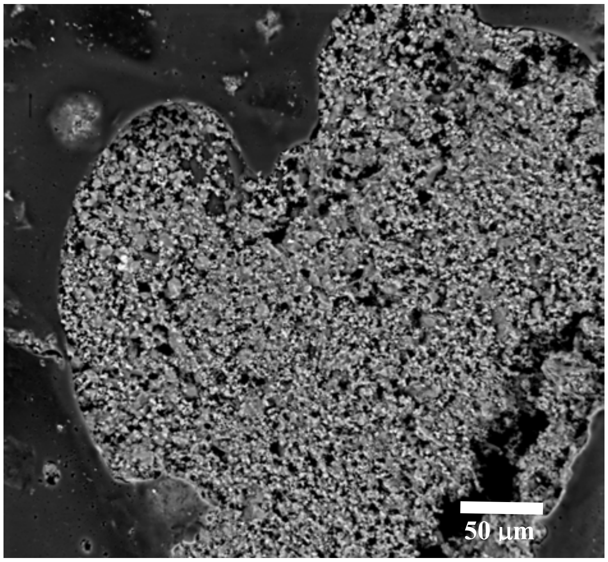

Figure 3.2b. Overview of AN-102 SEM Sample. Alumino silicate phases found around periphery of particle; several smaller Fe, Cr, U, V-containing phases were detected attached to the surface of the dominant material.

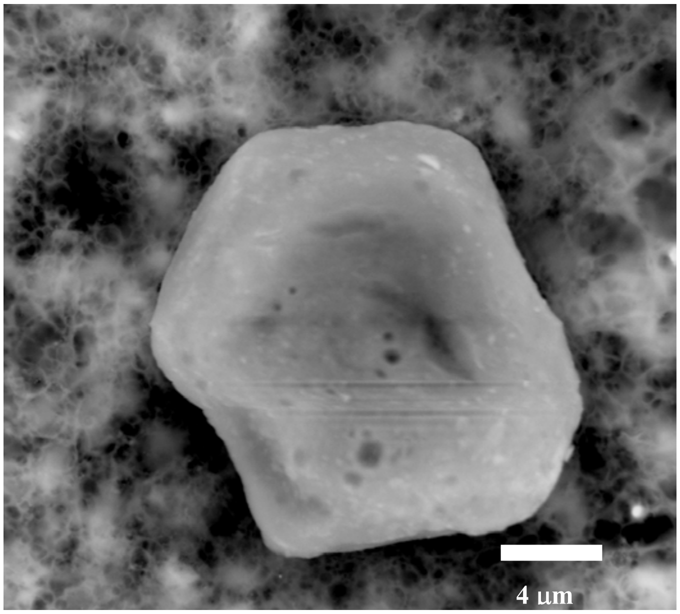

Figure 3.3a. Possible Zeolite Particle in AN-102. The darker pits on the surface result from the EDS probe. Such rapid damage further supports the identification of the phase as zeolite. The background material had a fibrous texture and was composed mainly of aluminum and sodium.

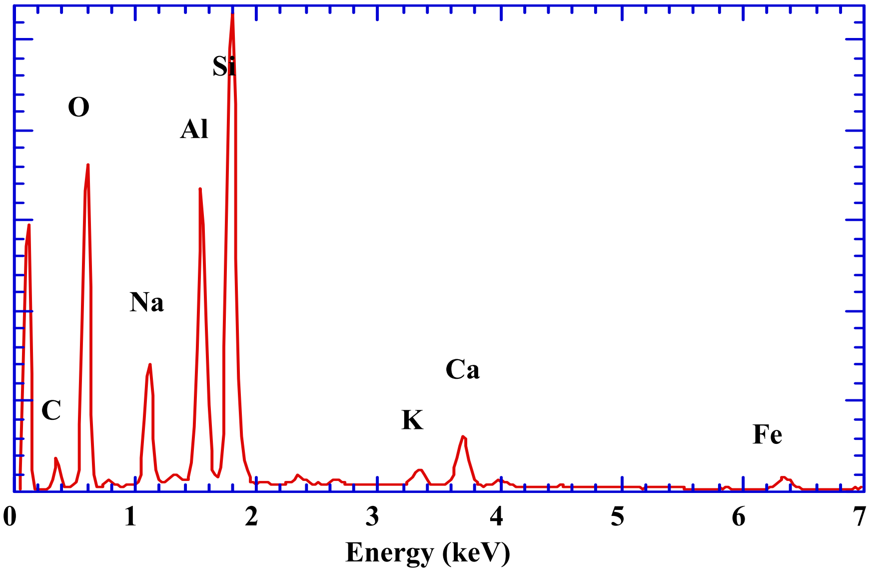

Figure 3.3b. EDS Analysis of Zeolite Phase. The alumino silicate phase contains calcium and a lesser amount of potassium and sodium.

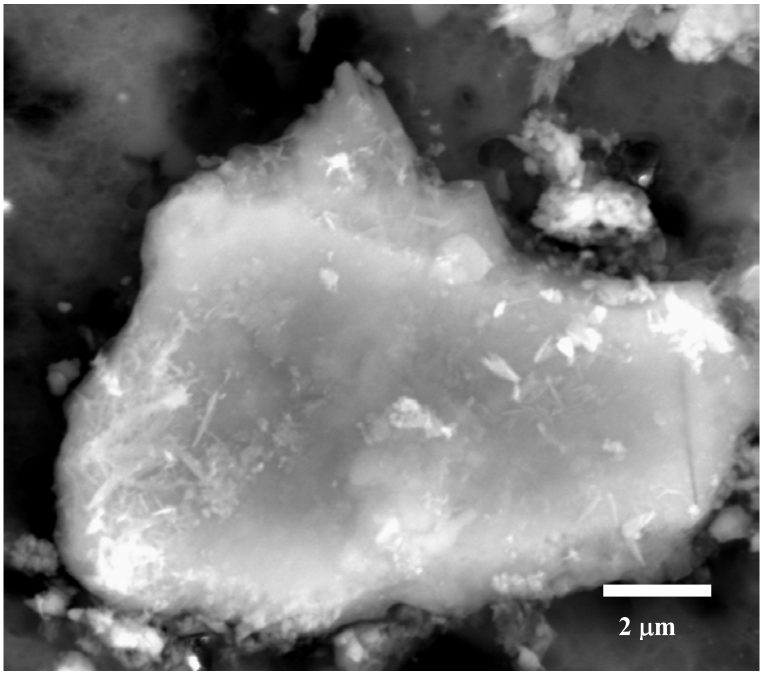

Figure 3.3c. Another Example of an Alumino Silicate Phase in AN-102

As can be seen in Figure 3.3c, the zeolitic particles had much smaller phases lying on the surface. It was not possible to determine the nature of the phases on the surface of the zeolitic phases.

The XRD signal strength will depend both on the crystallinity and the composition of the particles. A small amount of crystalline phase consisting of heavy metals could generate a stronger XRD signal than a larger mass of an amorphous low-Z material. In Figures 3.4 through 3.7, EDS analyses and SEM images of a series of high-Z particles found in AN-102 are shown. In Figure 3.4, an overview of these types of particles is shown. With backscattered imaging, uranium-bearing particles can be easily identified (Figure 3.5). Unlike the darker (low Z) particles that looked liked aggregates of many particles, the high-Z particles appeared to be individual crystals. Figure 3.6b is a yttrium vanadate phase. In Figures 3.5a and b, SEM analysis of a uranium oxide particle is shown. The EDS analysis of a cerium oxide particle is shown in Figure 3.6a, and in Figures 3.7a through c SEM-EDS analysis of iron-bearing particles is shown. These heavy minerals may also respond differently during laser light scattering particle size measurements than the light material because of their higher refractive indexes, although they represent a very minor component of the AN-102 sample. It is not possible to quantify the amount of particles in the sample with SEM techniques.

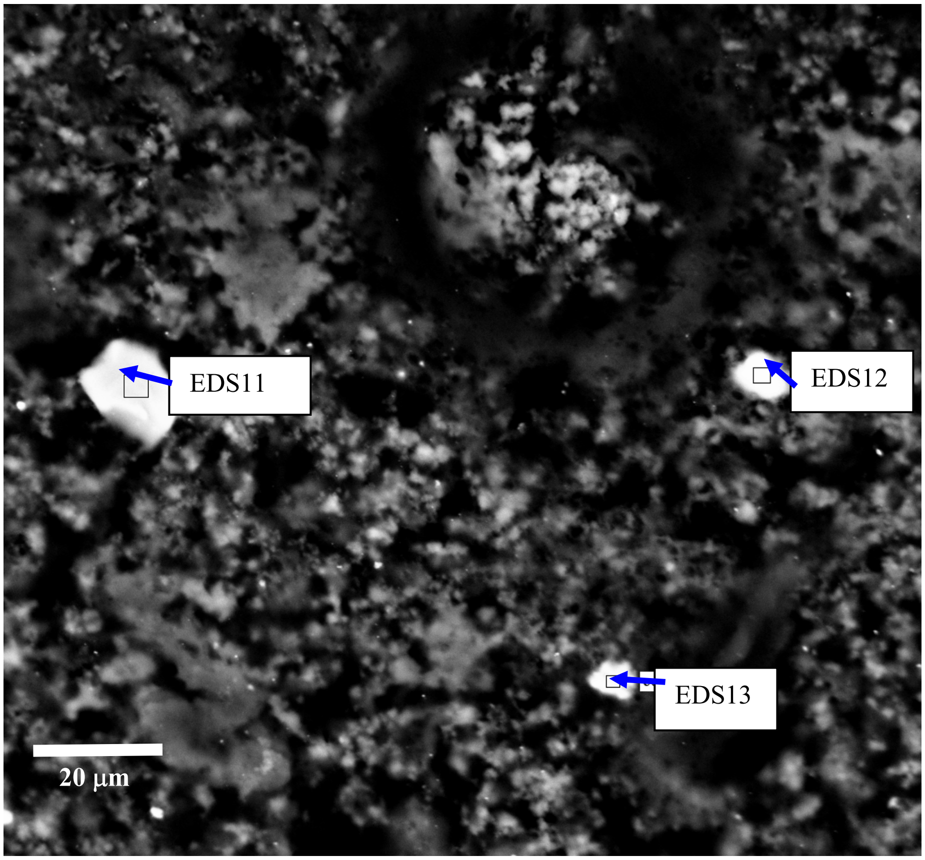

Figure 3.4. SEM/BSE Image of a Series of High-Z Particles on the Surface of Amorphous Material

In Figure 3.4, the white (bright) (high Z) particles were determined to be uranium oxide (EDS11), cerium oxide (EDS12), and a calcium-bearing phase, possibly calcite (EDS13). The mass of the material below was the sodium aluminate phase.

$Na_2U_2O_7$ (sodium uranates) have been suggested to occur in the caustic HLW tanks at the Savannah River Site (Jantzen and Laurinot 2001). If sodium uranate phases were present in AN-102, EDS would have been able to determine the composition. To confirm the composition of the uranium oxide phase, analyses were obtained with different-sized probes. As this was done, the sodium-to-uranium ratio was observed to change, but the sodium-to-aluminum ratio did not. There was no evidence from the XRD for sodium urinate-type phase, and evidence for a uraninite (UO_2) phase was also lacking. The XRD data appear to be more consistent with the oxidized form, UO_3. However, without some type of phase separation to isolate the uranium-bearing phase, it is difficult to confirm the nature of the uranium oxide.

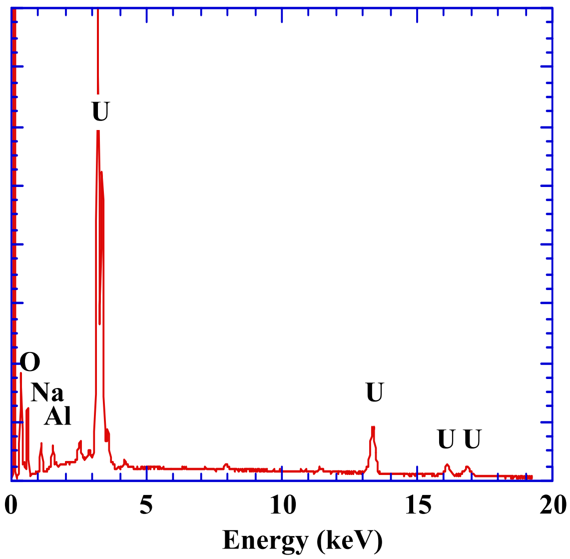

Figure 3.5a. EDS Analysis of Isolated Uranium Oxide Particle; analyses obtained with different-size spots to confirm the phase is oxide.

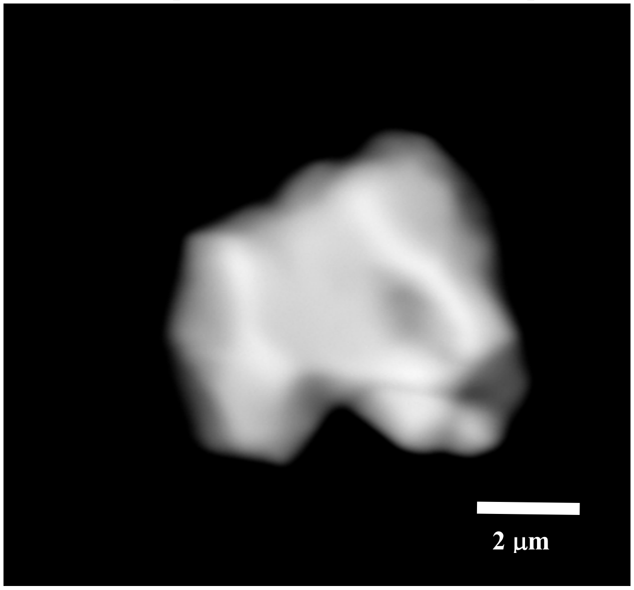

Figure 3.5b. Euhedral (well-formed) Uranium-Bearing Particle about 6–8 μm in Diameter. The BSE image of the particle suggests the phase is crystalline.

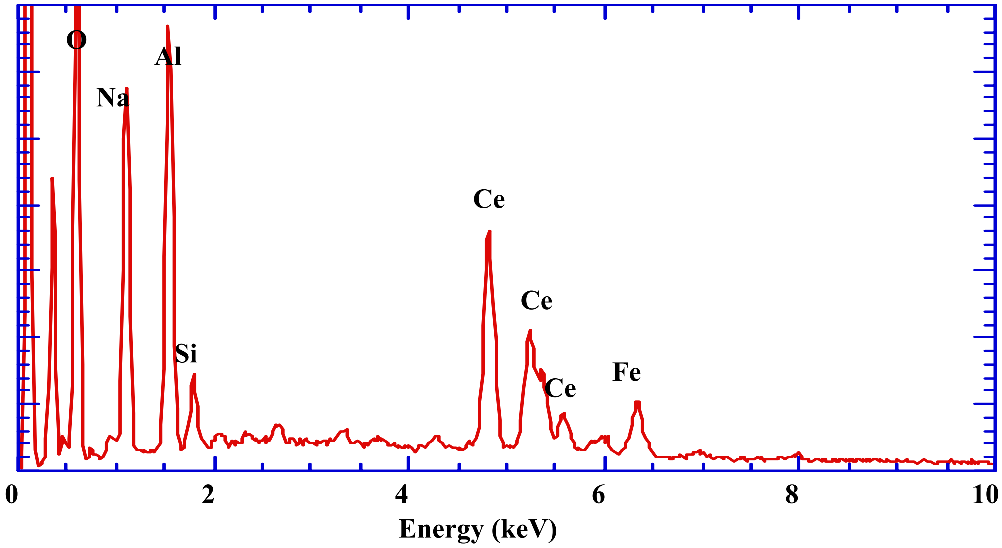

Figure 3.6a. EDS Analysis of Cerium Oxide Particle, Possibly Cerianite; the Na and Al signals are coming from the surrounding regions of the sample

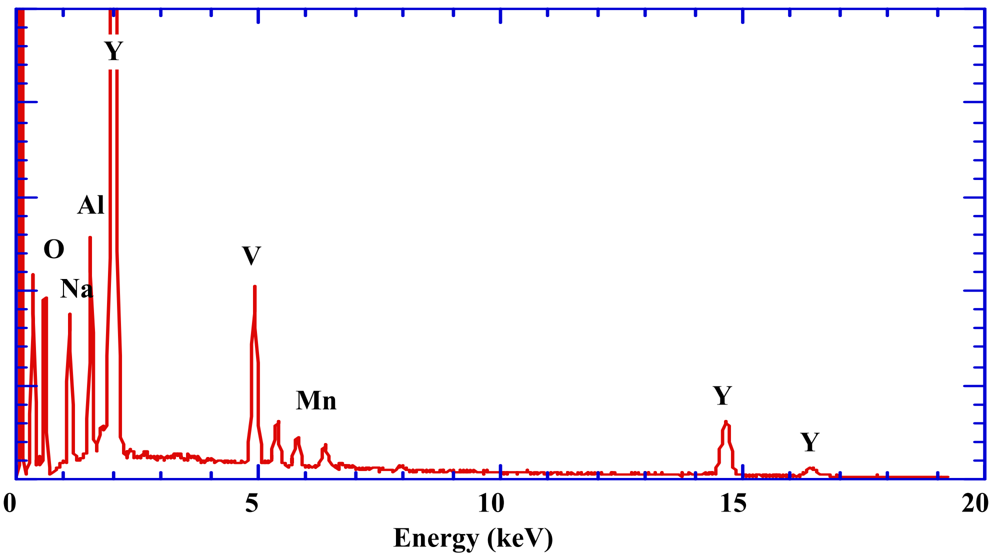

Figure 3.6b. EDS Analysis of a Yttrium Vanadate Particle Found in Sample AN-102

No other trace elements were observed in the uranium phase. Uranium is present in AN-102 at $3x10^2$ µg/g solid. Under backscattered imaging, the uranium-bearing particles are easily observable. The SEM is biased against lower average atomic number phases as these are less visible in the SEM under both backscatter electron (BSE) and secondary imaging conditions. Hence, most other elements present at similar levels in the waste were more difficult to detect in the SEM than uranium.

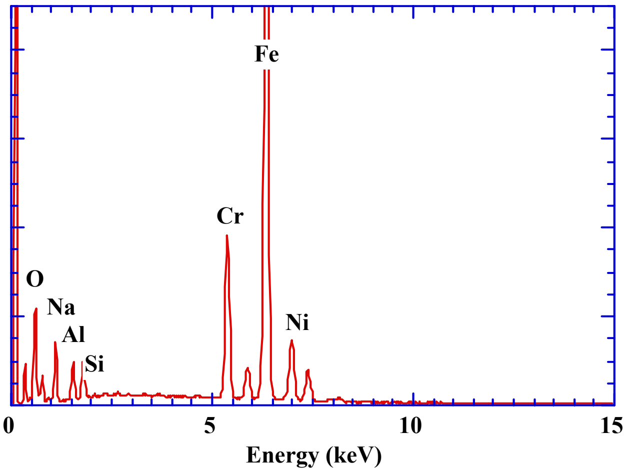

Figure 3.7a. EDS Analysis of Chromite Particle

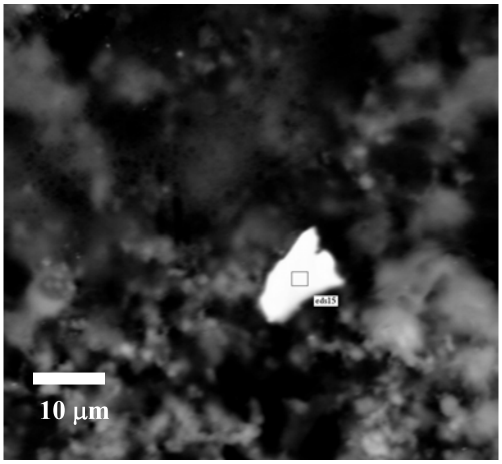

Figure 3.7b. BSE Image of the Chromite Particle

Both yttrium and vanadium are trace components in AN-102, present at about 2x10^1 µg/g solids. Cerium was also a trace component in the AN-102 washed solids. Chlorine, sulfur, silicon, and phosphorus were detected in the EDS analysis of some phases, such as the cerianite particle. However, these are most likely present in the sodium aluminate phase which was ubiquitous within AN-102.

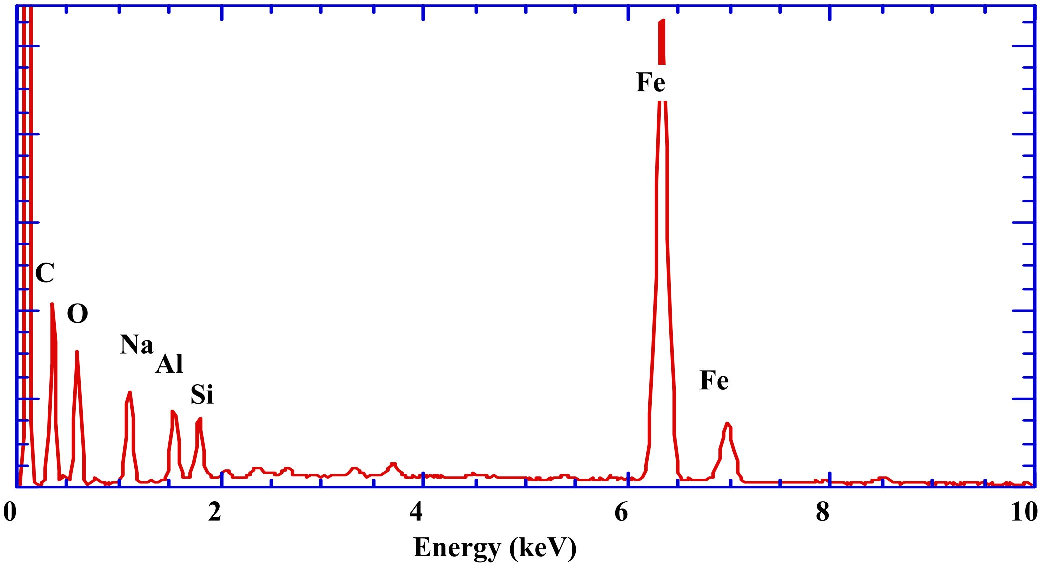

Figure 3.7c. EDS Analysis of Iron Oxide Particle

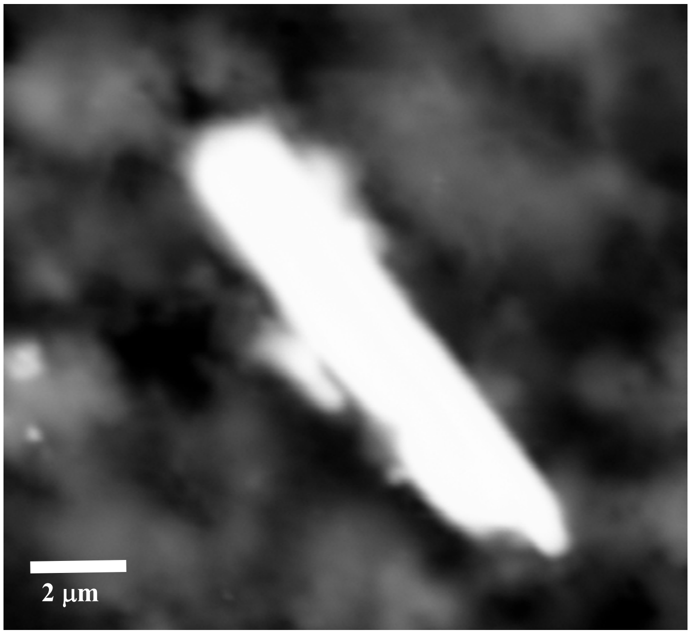

Figure 3.7d. BSE Image of the Iron-Bearing Particle

The chromite phase also contained nickel and a smaller amount of copper. It is not unexpected that these elements are present in the Fe-Cr phase. In Figure 3.7c and d, the analyzed particle contains mainly iron. The oxygen signal is extremely low, perhaps indicating that this phase is metallic; however, the weak oxygen x-rays can easily be attenuated in these types of samples and it is very unlikely that a micron-sized particle would remain metallic in a waste tank. The XRD scan also suggested that hematite (Fe_2O_3) may be present.

3.2 X-Ray Diffraction

A single XRD scan was run on the AN-102 washed solids sample. The major and minor lines are listed in Table 3.1 with possible assignments. The XRD scan is shown in Figure 3.8 with the background removed. The d-spacings of several major phases are also shown for phase identification. The spectrum consists of a limited number of sharp diffraction peaks with minor, broader peaks. The major lines can be matched with sodium nitrate ($NaNO_3$) and sodium nitrite ($NaNO_2$) and the broad lines with boehmite (AlOOH). The nitrite and nitrate phases are dissolved solids that formed during sample preparation in the SAL hot cells. These broad peaks suggest that the boehmite is poorly crystalline, perhaps a gel-like consistency. This could have important implications for waste treatment. Gibbsite is not present at detectable levels in the AN-102 sample. It is interesting that these phases containing sodium are still the major crystalline phases in the washed solids sample. Many of the minor lines have been matched with additional phases based on the SEM-EDS analyses. The SEM images suggest the presence of a large amount of amorphous material. This material was composed of mainly aluminum and sodium and was not detected during the XRD scan.

Cancrinite [$(Na,Ca,K)_{7.4}Al_6Si_6O_{24}(CO_3)_{1.6}\bullet 2.1H_2O$] and sodalite [$Na_4Si_3Al_3O_{12}Cl$] have been reported to form in caustic solutions under hydrothermal conditions (evaporators) (Jantzen and Laurinot 2001) and in Hanford tank waste (Krumhansl et al. 1999); however, no direct evidence is seen for either of these phases in the AN-102 sample. Major reflections for cancrinite would be expected at 0.321, 0.464, 0.364, and 0.210 nm (Ref: JCPDS 25-776) and at 0.362, 0.627, 0.209, and 0.237 nm for sodalite (JCPDS 20-495). In Nature, both sodalite and cancrinite are found as constituents of plutonic igneous rocks; however, cancrinite has been observed in Hanford tank wastes. These cancrinites often have nitrate ions incorporated into the structure.

The aluminum hydroxide phase, boehmite (AlOOH), was a reasonable match with XRD. The sodium nitrate and sodium nitrite phases appear to be clearly present, according to XRD, with well-defined sharp peaks; however, it was not possible to identify conclusively these phases with SEM-EDS. In one instance, there was evidence of small peak suggestive of nitrogen; however, generally, it is not possible to detect nitrogen with EDS.

Table 3.1. X-Ray Diffraction Data from AN-102 Washed Solids

2-Theta	d(nm)	BG	Height	I%	Area	I%	FWHM	P/N	Possible Assignments
8.987	0.9832	16	278	11.8	1325	11.3	0.203	8.1	zeolite
13.737	0.6441	22	56	2.4	399	3.4	0.303	3.2	UO_3, sodium aluminate
14.601	0.60617	63	161	6.8	2253	19.1	0.595	5.4	boehmite, AlOOH
14.952	0.59202	23	169	7.2	2362	20.1	0.594	6.1	NA
17.059	0.51933	13	387	16.4	1316	11.2	0.145	9.7	sodium sulfate
20.331	0.43643	15	45	1.9	89	0.8	0.084	2.9	UO_3
23.790	0.37370	42	70	3.0	145	1.2	0.088	3.3	zeolite, sodium aluminate
25.727	0.34599	21	106	4.5	271	2.3	0.109	4.7	UO_3
27.402	0.32521	56	127	5.4	455	3.9	0.152	4.7	UO_3
28.155	0.31668	118	317	13.4	4067	34.6	0.545	7.6	boehmite, AlOOH
29.462	0.30293	217	2362	100.0	7966	67.7	0.143	23.3	nitratite ($NaNO_3$)
30.085	0.29679	113	645	27.3	2345	19.9	0.155	11.7	sodium nitrite
30.911	0.28905	58	405	17.1	1529	13.0	0.160	9.4	NA
31.745	0.28164	53	689	29.2	6230	52.9	0.384	12.6	nitratite, sodium oxalate, UO_3
32.101	0.27860	49	313	13.3	2878	24.5	0.391	8.2	$NaNO_2$, uraninite, Na aluminate
34.454	0.26009	73	1576	66.7	11770	100.0	0.317	19.4	iron chromium oxide, sodium oxalate
35.509	0.25260	37	292	12.4	1117	9.5	0.163	8.0	sodium aluminate
36.352	0.24693	6	69	2.9	137	1.2	0.084	4.0	boehmite, AlOOH
38.562	0.23328	72	903	38.2	9635	81.9	0.453	14.5	sodium oxalate, sodium aluminate
39.090	0.23025	41	855	36.2	5912	50.2	0.294	14.3	nitratite
41.577	0.21703	23	125	5.3	744	6.3	0.253	5.1	NA
42.311	0.21343	42	101	4.3	448	3.8	0.189	4.2	NA
42.616	0.21197	17	330	14.0	1934	16.4	0.249	8.9	sodium aluminate
44.544	0.20324	17	317	13.4	1908	16.2	0.256	8.7	sodium nitrite
45.206	0.20041	40	234	9.9	701	6.0	0.127	7.1	sodium aluminate
46.885	0.19362	63	123	5.2	270	2.3	0.093	4.5	uraninite
47.307	0.19199	78	73	3.1	231	2.0	0.134	3.0	nitratite
47.960	0.18953	87	222	9.4	1009	8.6	0.193	6.3	NA
48.408	0.18788	87	292	12.4	1653	14.0	0.241	7.5	NA
49.150	0.18521	157	333	14.1	3297	28.0	0.421	7.5	boehmite
50.147	0.18176	26	122	5.2	781	6.6	0.272	5.0	NA
51.187	0.17831	24	66	2.8	208	1.8	0.134	3.5	sodium aluminate

Table 3.1. X-Ray Diffraction Data from AN-102 Washed Solids

2-Theta	d(nm)	BG	Height	I%	Area	I%	FWHM	P/N	Possible Assignments
51.719	0.17660	34	51	2.2	287	2.4	0.239	2.8	boehmite
53.109	0.17230	24	73	3.1	173	1.5	0.101	3.7	NA
53.664	0.17065	20	65	2.8	178	1.5	0.116	3.5	NA
54.685	0.16770	27	65	2.8	338	2.9	0.221	3.4	NA
55.406	0.16569	55	274	11.6	1316	11.2	0.204	7.6	boehmite
55.745	0.16476	68	287	12.2	1480	12.6	0.219	7.6	uraninite
56.693	0.16223	12	157	6.6	1022	8.7	0.277	6.0	hematite
61.016	0.15173	7	70	3.0	256	2.2	0.155	4.0	NA
63.899	0.14556	11	148	6.3	1742	14.8	0.500	5.9	hematite

BG= Background, I% = Relative intensity, FWHM = Full width half height, P/N = peak over noise, NA = not assigned
Compute out put – no rounding was attempted.

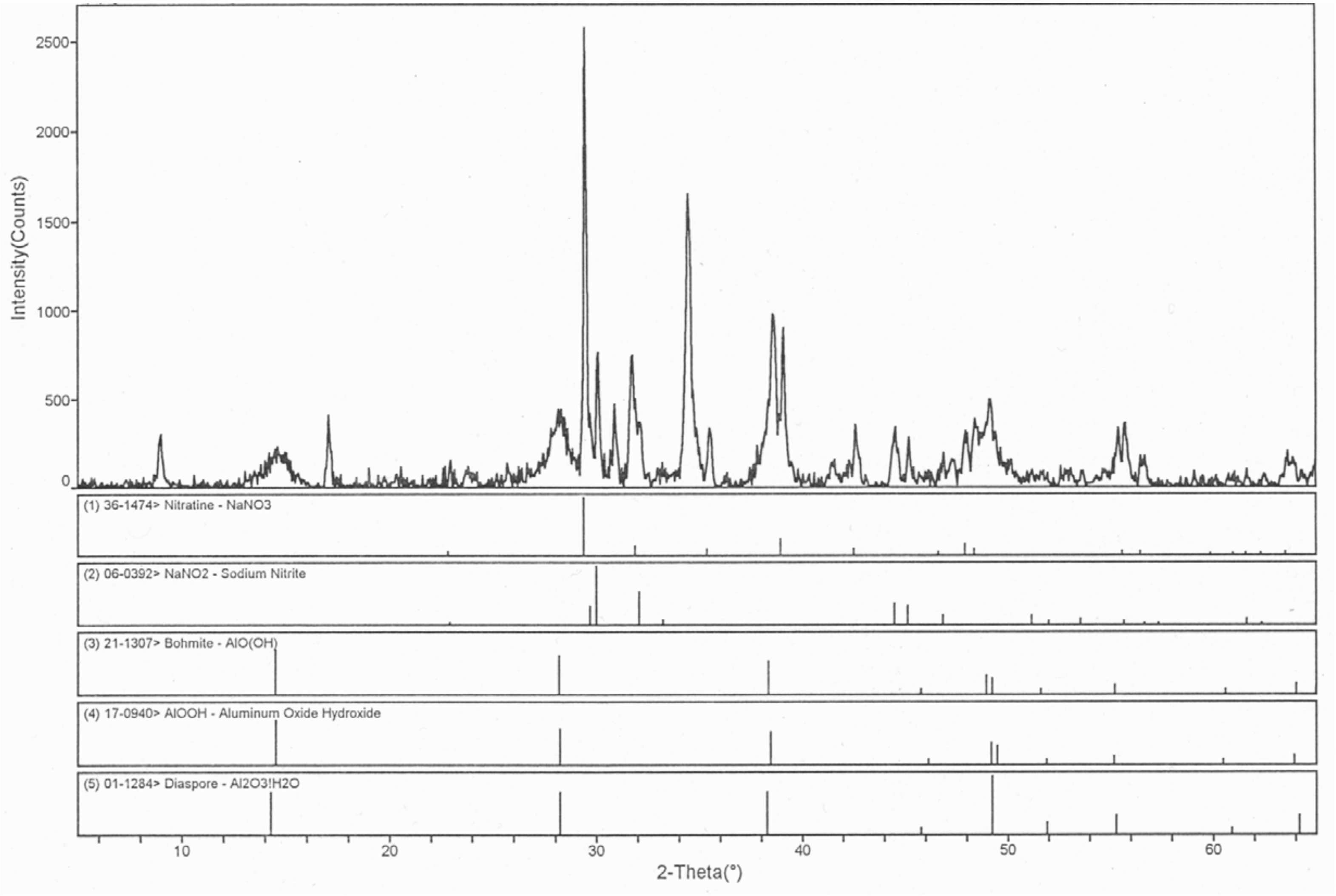

Figure 3.8. X-Ray Diffraction Scan of AN-102 Washed Solids

3.3 Particle Size Analysis of AN-102

The suspending medium for these analyses was a diluted surrogate supernatant based on the analytical laboratory data obtained for an AN-102 supernatant liquid. The composition of this supernatant liquid is reported in Table 3.2.

Table 3.2. Surrogate Supernatant Composition

Compound	Moles
$NaNO_3$	1.68E-01
NaOH	4.88E-01
$Al(NO_3)_3 \cdot 9H_2O$	1.14E-01
Na_2SO_4	1.50E-02
$Na_2HPO_4 \cdot 7H_2O$	5.66E-03
NaCl	1.19E-02
$NaNO_2$	2.57E-01
$NaCO_3$	1.11E-01
$Na_2C_2O_4$	7.08E-04
NaF	1.33E-03

The particle size distributions on a volume basis are presented graphically in Figure 3.9. In this figure, the top graph presents the volume percent of particles belonging to a discrete range of particle size or bin. The bin-centered values of this histogram are displayed on the graph. The lower graph presents the sum of these data and is referred to as the cumulative volume percent. These data represent the volume percent of particles smaller than a given particle size. For this reason the right-most bin values are used in this graph. The volume distribution data indicate that most of the volume slurry is due to particles in the 0.5 to 15 μm particle size. As the shear rate in the instrument increased (due to increasing the flow rate from 40 to 60 mL/s) some of the larger particles (i.e., particles greater than 15 μm) appear to break apart, resulting in a larger volume of smaller-diameter particles. When sonication is applied (i.e., 40 W for 90 sec) at the same flow rate (60 mL/s), the particles in the 15 to 150 μm size range appeared to break apart further. A second sonication resulted in further de-agglomeration.

The particle size distributions on a number basis are presented graphically in Figure 3.10. Obviously, a large difference exists in particle size distribution between the volume basis and the number basis distributions. These differences can be explained by recognizing that as particle size increases the volume contribution of a particle increases cubically. This weights the volume distribution more heavily toward larger particles (i.e., a few of the larger particles will greatly affect the volume basis but will have no significant effect on the number basis). Hence, Figure 3.11 suggests that most of the particles are between approximately 0.6–3.0 microns. In addition, most of these particles do not change due to changes in the shear force applied. However, small changes in the number of larger particles are greatly amplified on a volume basis (Figure 3.12).

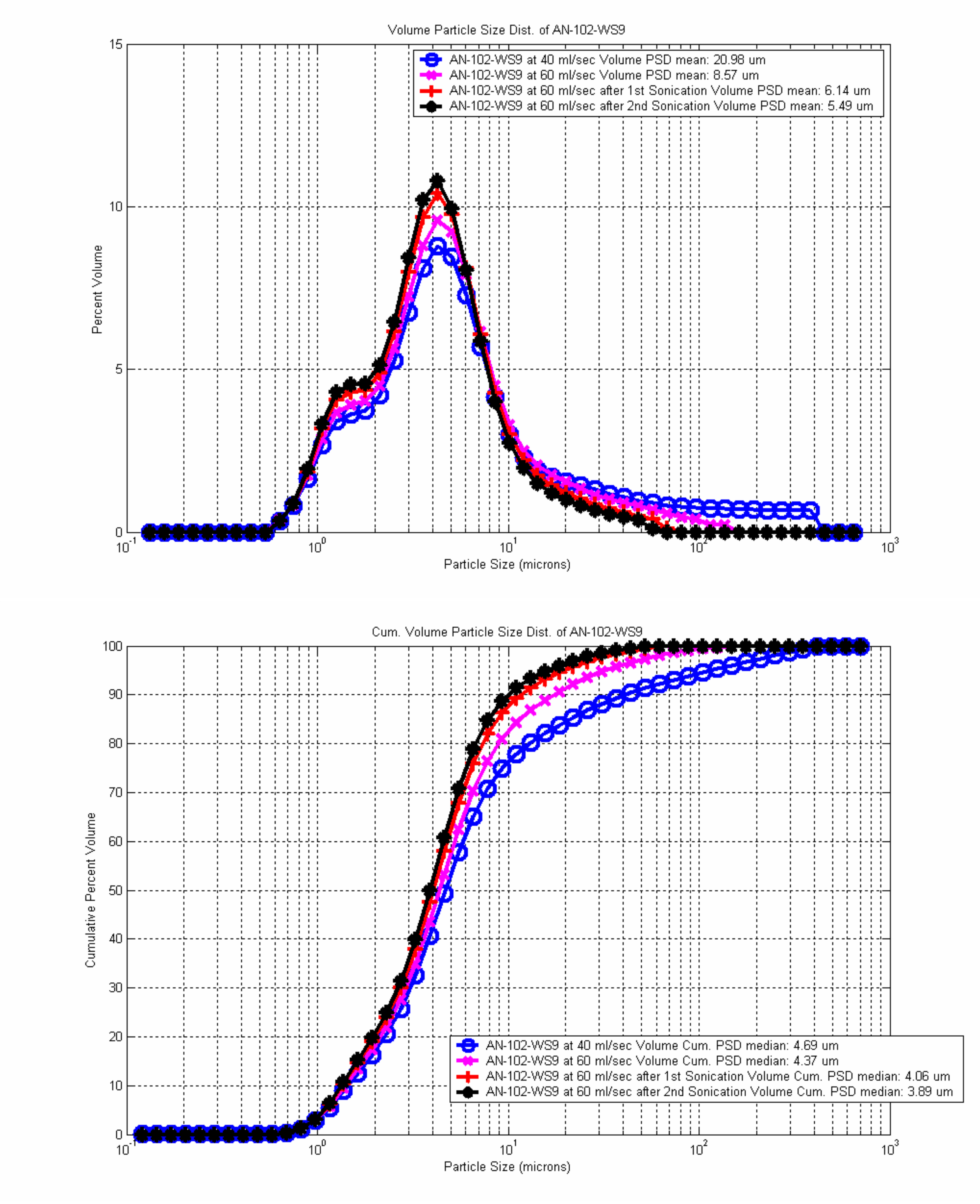

Figure 3.9. X100 Particle Size Distribution of AN-102 Washed Solids on a Volume Basis (top–differential; bottom–cumulative)

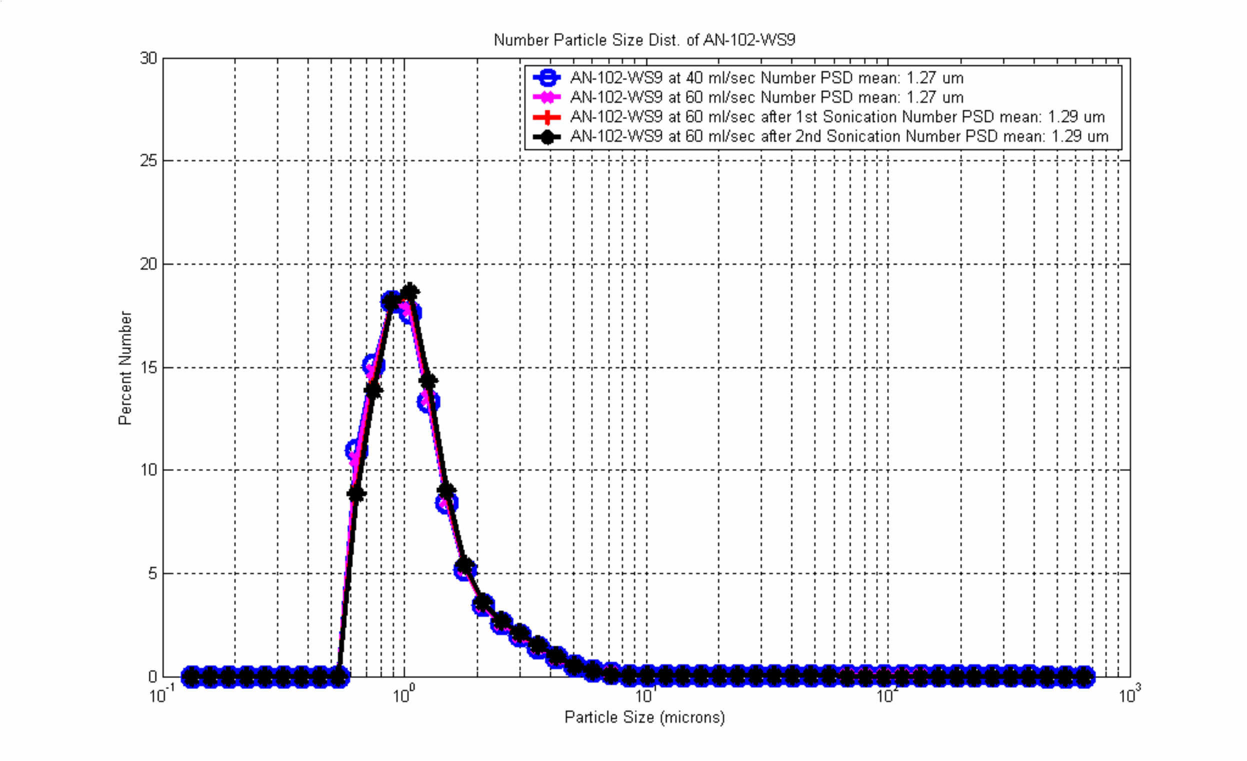

Figure 3.10a. X100 Particle Size Distribution of AN-102 Washed Solids on a Number Basis – Differential

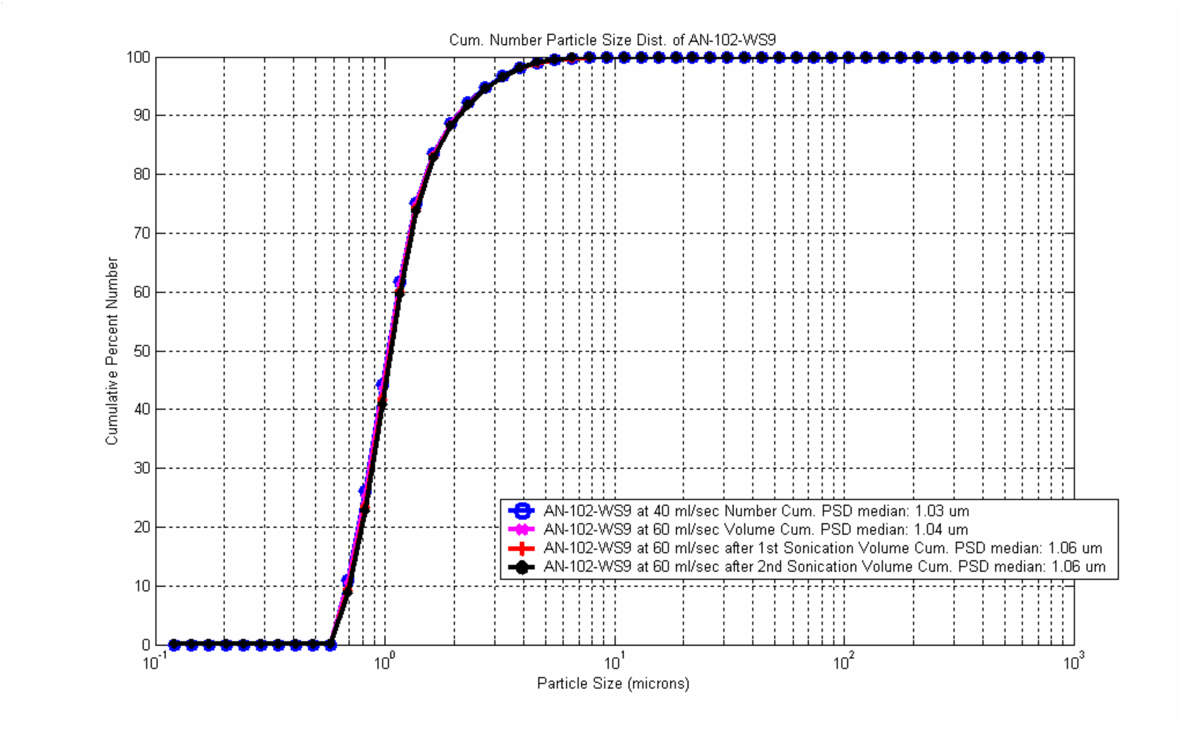

Figure 3.10b. X100 Particle Size Distribution of AN-102 Washed Solids on a Number Basis – Cumulative

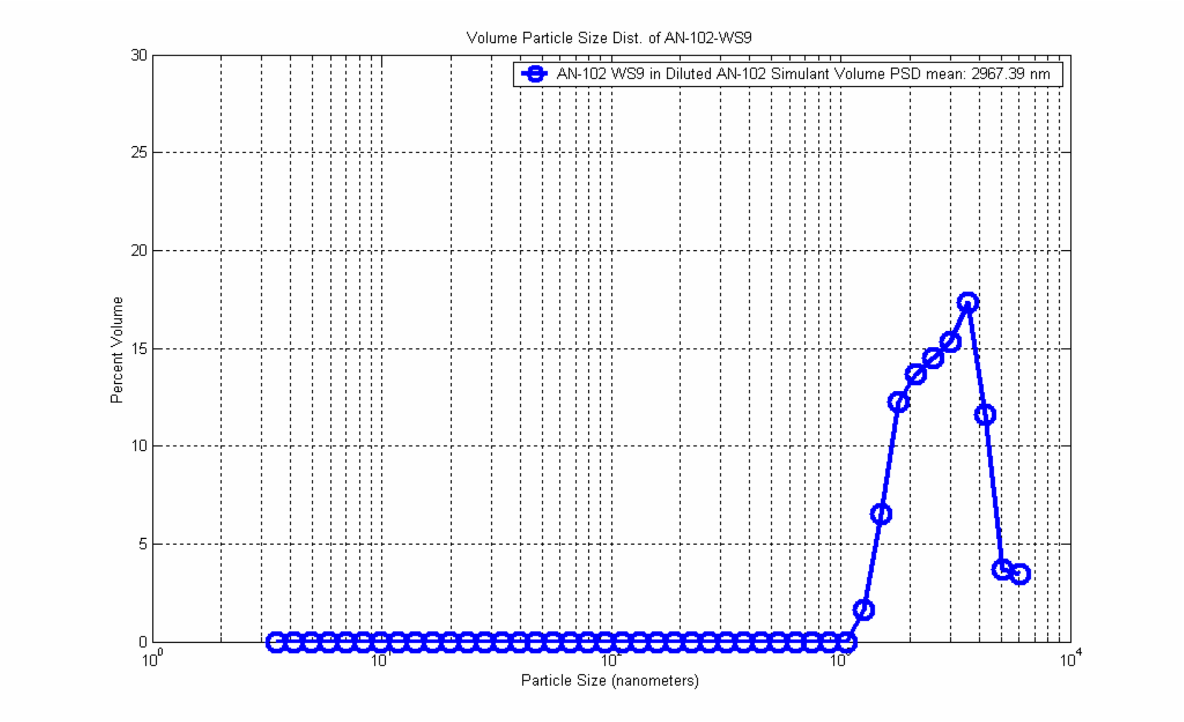

Figure 3.11a. UPA Particle Size Distribution of AN-102 Washed Solids on a Volume Basis – Differential

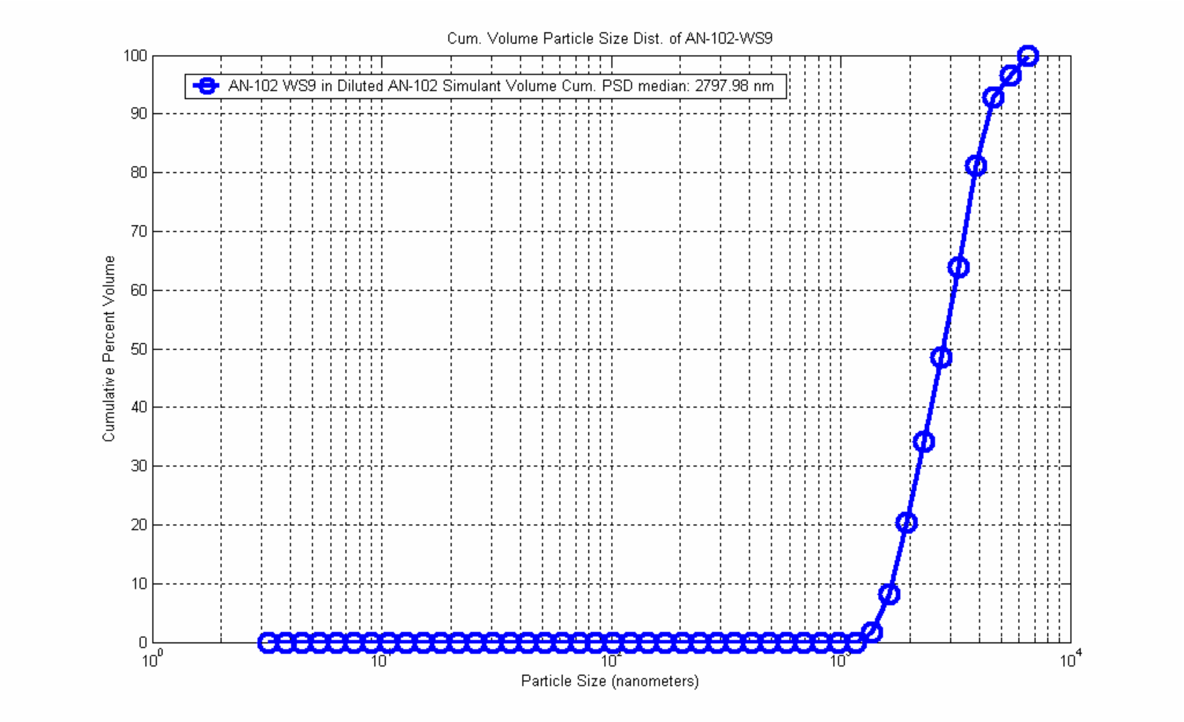

Figure 3.11b. UPA Particle Size Distribution of AN-102 Washed Solids on a Volume Basis – Cumulative

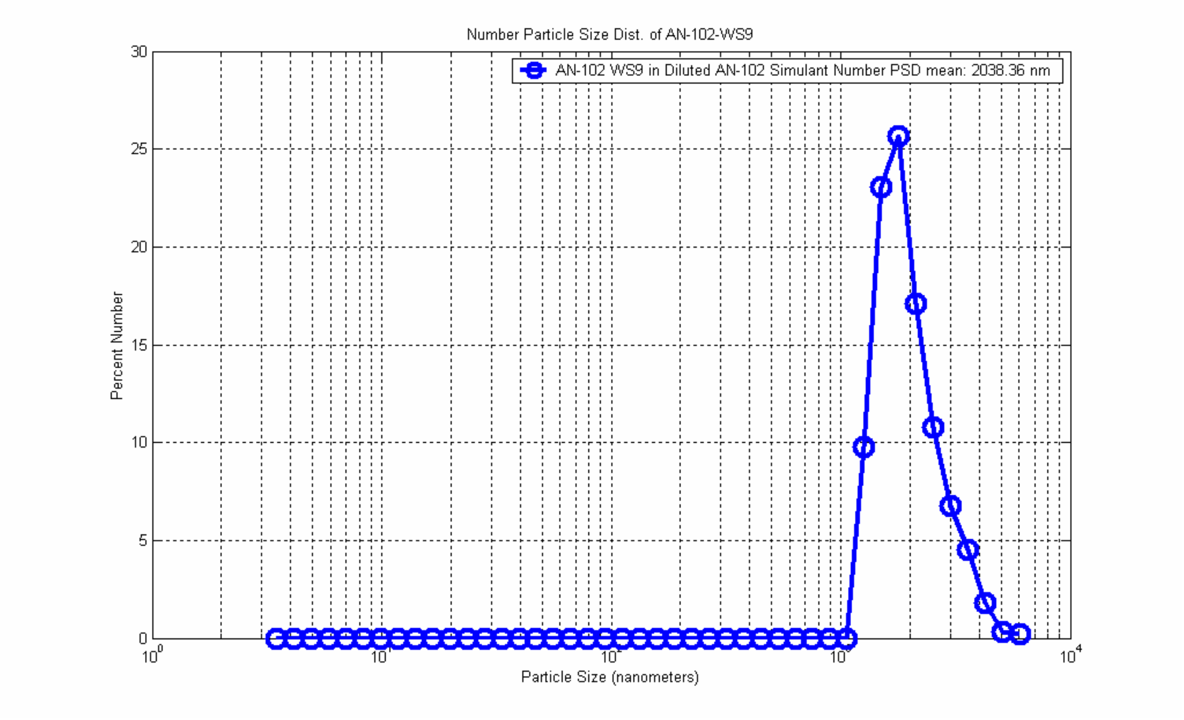

Figure 3.12a. UPA Particle Size Distribution of AN-102 Washed Solids on a Number Basis – Differential

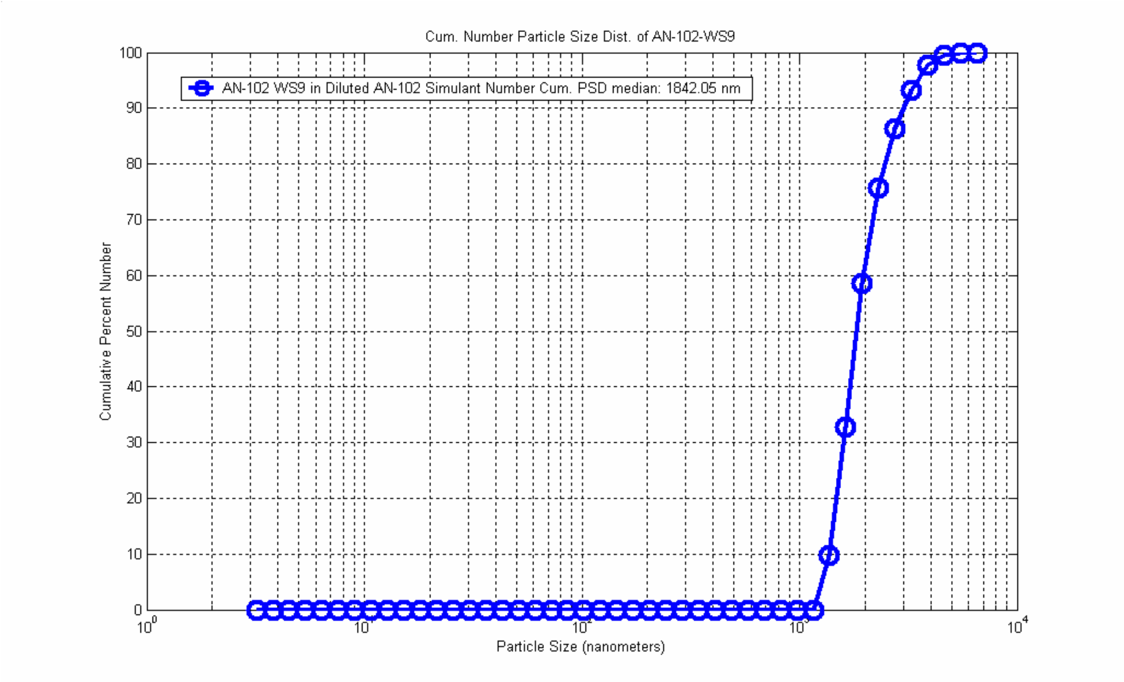

Figure 3.12b. UPA Particle Size Distribution of AN-102 Washed Solids on a Number Basis – Cumulative

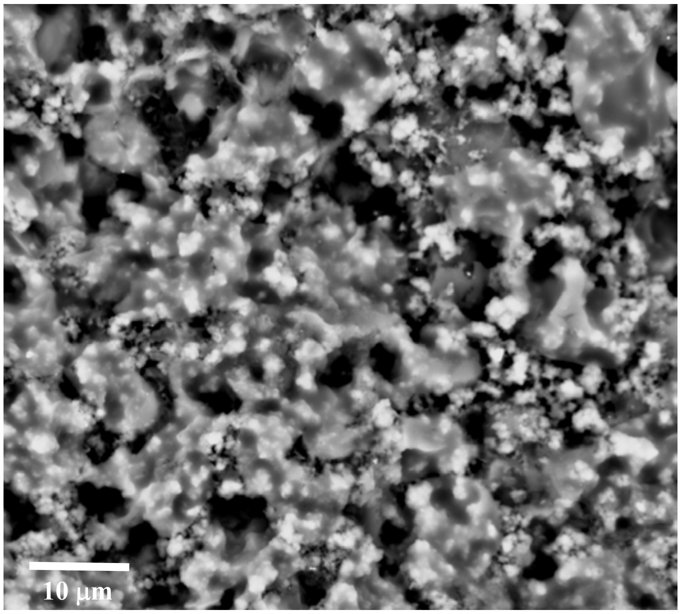

Figure 3.13. Medium Magnification of Major Phase in AN-102 Sample; particles of several sizes observed as agglomerates from 10–50 μm across made up of particles about <1–3 μm in size

As-received samples were also analyzed in the UPA. The particle size range that is common to both the X100 and UPA is 0.12–6.5 microns. The UPA data are consistent with the X100 data over this range on both volume and number bases. Because the UPA did not detect particles smaller than the X100 capabilities, the X100 particle size distribution should be considered reliable to a lower limit of 3 nm.

3.4 SEM Analysis of Particle Size in AN-102

Several SEM images of particles can be compared with PSD data. The low-magnification image shown in Figure 3.14 illustrates the nature of AN-102 washed solids as a highly heterogeneous and friable-looking material. The light-scattering analysis indicated that the particles were 0.5 to 15 microns in size. However, with sonication the volume of smaller particles increased, and further sonication resulted in further fragmentation of the sample. Indeed, most of the particles were found to be 0.6–3.0 μm after sonication. In the higher-magnification images, many of the particles are <10μm, and even smaller particles are observable. These laser light-scattering observations were reasonably consistent with the SEM images of AN-102 washed solids.

Although the results of the particle size analysis were reasonably consistent with observations made with SEM on the nature of the particles, the sample preparation method for microscopy often results in the formation of soft agglomerated particles. Therefore, the SEM images of particles do not represent the anticipated morphology of the particles during waste processing. These agglomerates form as the solids are dewatered and washed on a dead-end filter. This suggests that the WTP will not see such large agglomerated particles.

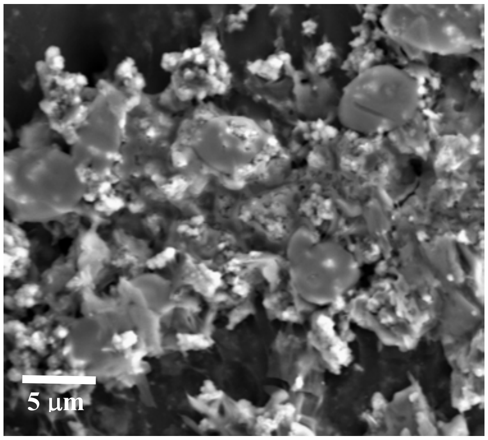

Figure 3.14a. At Higher Magnification, Smaller, Brighter Particles Attached to Surface of Larger Particles

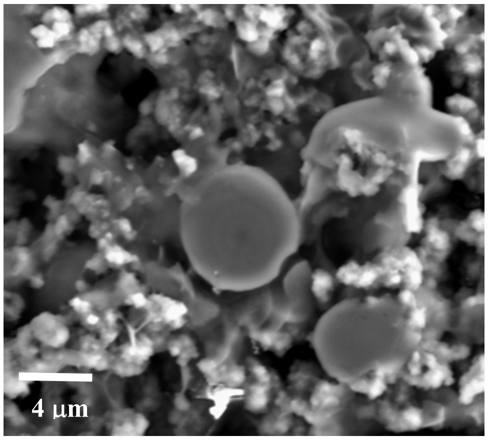

Figure 3.14b. Botryoidal Particles Appear To Possess Diameters of 4 to 6 μm

4.0 Analysis of AZ-101 Solids

Samples of AZ-101 washed solids and unwashed material were prepared for analysis in the SAL hot cells. The results of the analyses are described in this section.

4.1 XRD Analysis of AZ-101 Washed Solids Sample

The XRD scan of AZ-101 washed solids is shown in Figure 4.1a-b, and the major d-spacings are listed in Table 4.1. All major peaks in the spectra were identified, including gibbsite [$Al(OH)_3$], boehmite (AlOOH), and hematite (FeOOH). A significant background hump can be seen in the scan. Although this was easily removed by background fitting, it indicated that a proportion of the material may be either partially crystalline or amorphous. All the boehmite peaks were broad, indicating a poorly crystallized form and/or small crystallite size, whereas both hematite and gibbsite exhibited sharp peaks. This difference in morphology makes reliable estimates of the relative amounts of each Al-bearing phase potentially erroneous.

The material exhibited well-crystallized phases, although a large amorphous hump is apparent. Major phases identified as gibbsite ($Al(OH)_3$), boehmite (AlOOH), and hematite (Fe_2O_3). The 110 and 200 reflections from gibbsite were missing in the XRD scans. This may indicate preferential orientation of the crystals in the **c**-direction on the sample XRD slide, which commonly occurs in phases with platy forms. Along with the broadened peaks from boehmite, this further complicates determining the relative levels of gibbsite and boehmite.

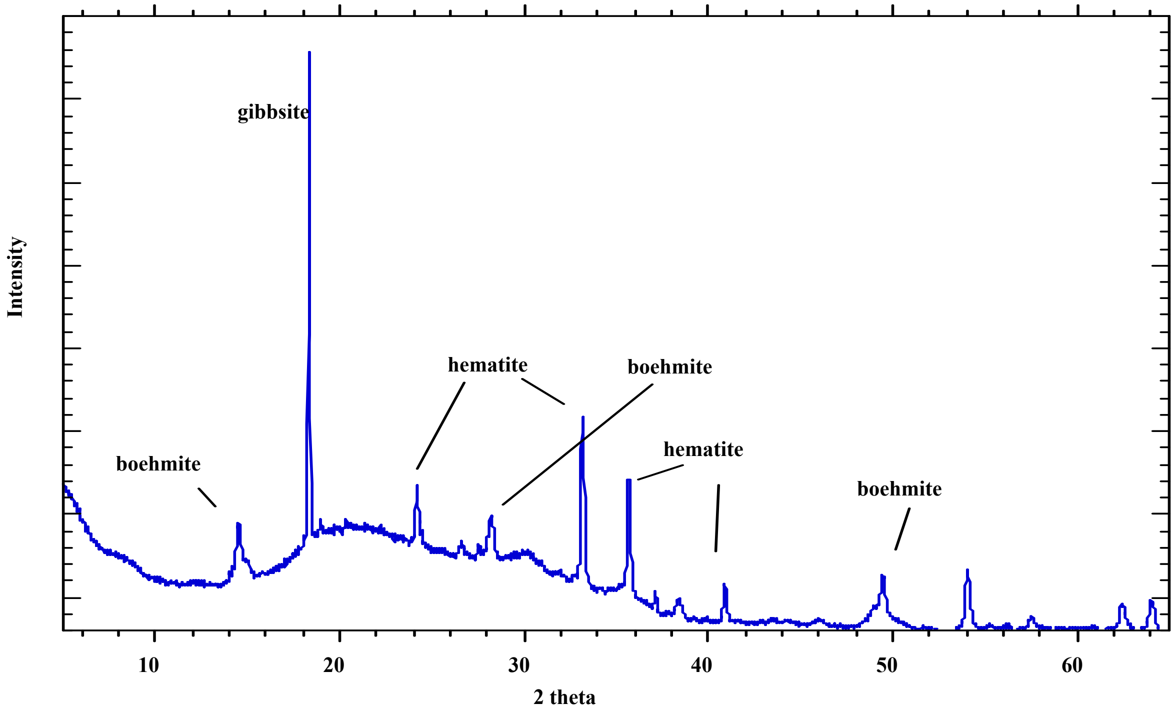

Figure 4.1a. XRD Scan of AZ-101 with Major Phase Identifications Marked

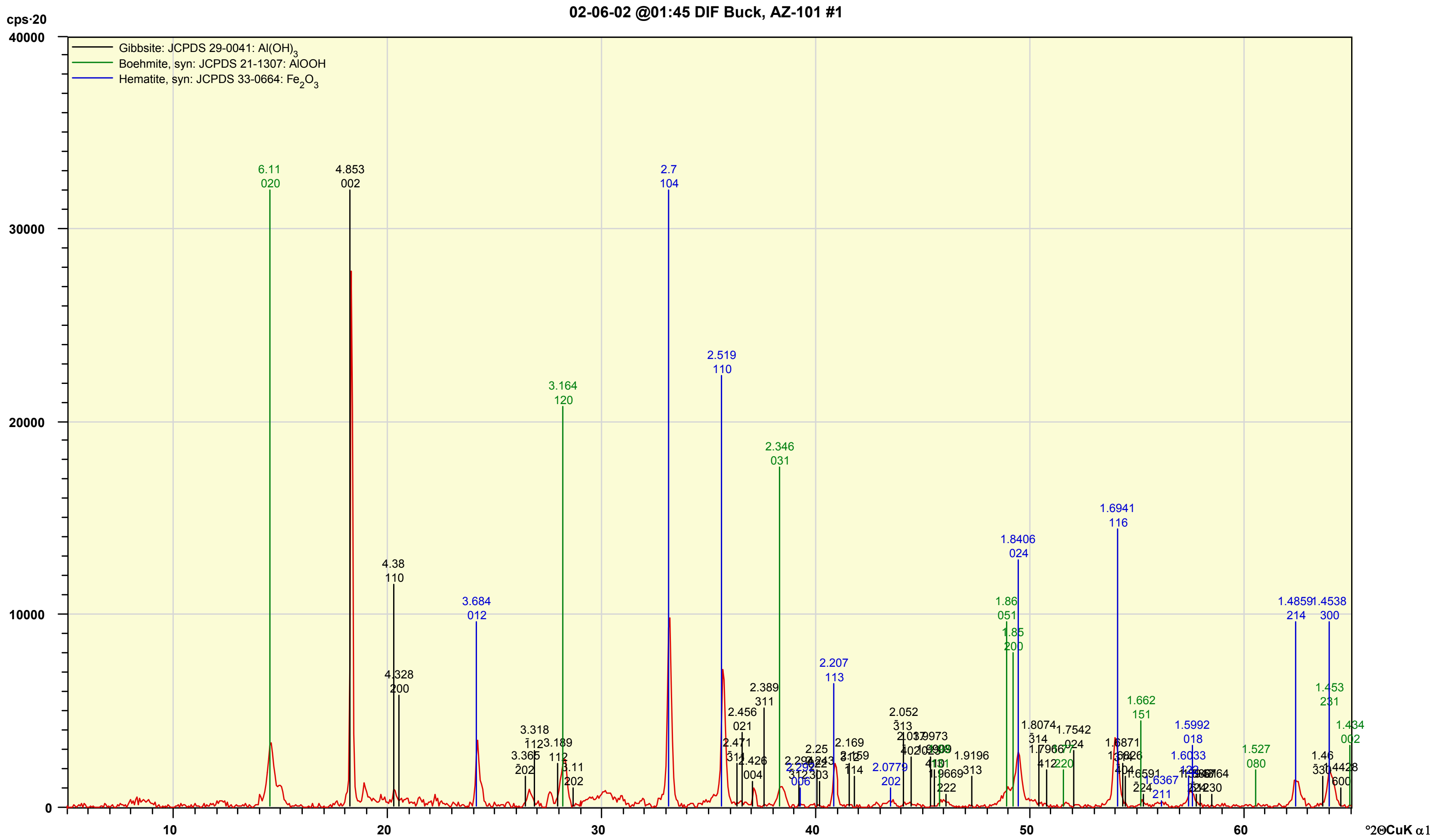

Figure 4.1b. XRD Scan of AZ-101 Background Subtracted

Table 4.1. X-Ray Diffraction Data from AZ-101 Washed Runs 1 and 2

2-Theta	d(nm)	hkl	BG	Height	I%	Area(1)	I%	FWHM	Possible Assignments
5.686	1.553		58	290	1.3	1046	0.9	0.061	NA
8.242	1.07185		167	306	1.4	2788	2.3	0.155	NA
8.295	1.06506		80	448	2.0	5143	4.2	0.195	NA
8.542	1.03431		129	319	1.4	3388	2.8	0.181	NA
8.825	1.00124		91	367	1.6	6613	5.4	0.306	NA
12.277	0.72035		49	235	1.0	1062	0.9	0.077	NA
14.041	0.63023		116	536	2.4	2226	1.8	0.071	NA
14.520	0.60955	020	63	2455	10.8	69543	57.0	0.482	boehmite (AlOOH)
15.018	0.58942		82	844	3.7	20285	16.6	0.409	NA
18.323	0.48379	002	54	22660	100.0	121979	100.0	0.092	gibbsite
18.922	0.46861		39	855	3.8	3789	3.1	0.075	NA
22.207	0.39998		86	342	1.5	1566	1.3	0.078	NaOH
24.180	0.36777	012	96	2635	11.6	21550	17.7	0.139	hematite
25.625	0.34735		93	171	0.8	776	0.6	0.077	NA
26.604	0.33478	-112	146	629	2.8	4288	3.5	0.116	gibbsite
27.523	0.32381	112	132	632	2.8	7992	6.6	0.215	gibbsite
28.181	0.3164	120	132	2016	8.9	35749	29.3	0.301	boehmite
29.924	0.29835		371	401	1.8	2184	1.8	0.093	NaOH, nitratite
30.079	0.29685		323	547	2.4	2967	2.4	0.092	NA
30.300	0.29474		152	646	2.9	7864	6.4	0.207	NA
30.618	0.29175		83	458	2.0	4933	4.0	0.183	NaOH
31.940	0.27996		98	211	0.9	805	0.7	0.065	nitratite
32.687	0.27373		122	264	1.2	1778	1.5	0.114	NaOH
33.159	0.26995		66	7766	34.3	79632	65.3	0.174	hematite
34.597	0.25905		159	273	1.2	1567	1.3	0.098	NA
34.884	0.25698		109	389	1.7	2695	2.2	0.118	NA
35.223	0.25458		138	616	2.7	6924	5.7	0.191	NA
35.660	0.25157	110	300	5901	26.0	59453	48.7	0.171	hematite
36.437	0.24638	021	23	400	1.8	6888	5.6	0.293	gibbsite
36.698	0.24469		51	480	2.1	1759	1.4	0.062	NaOH
37.119	0.24201		51	1044	4.6	6804	5.6	0.111	gibbsite
38.380	0.23434	031	17	896	4.0	16753	13.7	0.318	boehmite
40.861	0.22067	113	63	1892	8.3	17907	14.7	0.161	hematite
43.221	0.20915	-313	54	161	0.7	652	0.5	0.069	gibbsite
43.464	0.20803	202	43	235	1.0	2090	1.7	0.151	hematite
44.183	0.20482	-402	51	215	0.9	1082	0.9	0.086	gibbsite
44.429	0.20374		62	148	0.7	984	0.8	0.113	NA
45.883	0.19762	131	52	289	1.3	1177	1.0	0.069	boehmite (AlOOH)
46.202	0.19632		71	188	0.8	1235	1.0	0.112	NA
48.783	0.18652		26	692	3.1	35268	28.9	0.866	NA
48.980	0.18582	051	58	865	3.8	30954	25.4	0.608	boehmite
49.440	0.1842	024	255	2225	9.8	38379	31.5	0.293	hematite
50.178	0.18166		49	367	1.6	5654	4.6	0.262	NaOH
50.518	0.18052	-314	90	212	0.9	2438	2.0	0.196	gibbsite
51.688	0.1767	220	78	202	0.9	751	0.6	0.063	boehmite

Table 4.1. X-Ray Diffraction Data from AZ-101 Washed Runs 1 and 2

2-Theta	d(nm)	hkl	BG	Height	I%	Area$^{(1)}$	I%	FWHM	Possible Assignments
54.020	0.16961	116	29	3046	13.4	36095	29.6	0.201	hematite
55.279	0.16604	151	19	267	1.2	1134	0.9	0.072	boehmite
56.269	0.16335		67	213	0.9	1759	1.4	0.140	NaOH
57.500	0.16015	122	30	659	2.9	9247	7.6	0.239	hematite
62.382	0.14873	214	43	1400	6.2	16904	13.9	0.205	hematite
63.981	0.1454	300	51	1562	6.9	20305	16.6	0.221	hematite
AZ-101-2	Run with internal corundum standard*								
8.295	1.06506		24	112	0.4	530	0.2	0.080	NA
11.843	0.74664		108	399	1.3	4526	2.1	0.193	NA
11.960	0.73938		39	576	1.9	2711	1.2	0.080	NA
12.040	0.73445		81	548	1.8	7785	3.5	0.242	NA
12.203	0.72472		60	483	1.6	3578	1.6	0.126	NA
12.251	0.72185		85	343	1.1	3747	1.7	0.186	NA
13.988	0.63261		39	368	1.2	2099	1.0	0.097	NA
14.519	0.60956	020	66	1399	4.6	28224	12.8	0.343	boehmite
14.898	0.59414		96	589	2.0	7478	3.4	0.216	NaOH
15.131	0.58505		72	349	1.2	6382	2.9	0.311	NA
18.336	0.48346	002	97	3387	11.2	16807	7.6	0.084	gibbsite
22.197	0.40015		111	288	1.0	1062	0.5	0.063	NA
24.179	0.36779	012	71	1731	5.7	13319	6.1	0.131	hematite
25.619	0.34743	012	150	23008	76.3	158493	72.1	0.117	corundum
26.033	0.342		40	331	1.1	1496	0.7	0.077	NA
26.658	0.33412	-202	165	391	1.3	1755	0.8	0.076	gibbsite
27.543	0.32358	-112	226	279	0.9	942	0.4	0.057	gibbsite
28.199	0.3162	120	132	1094	3.6	17474	7.9	0.272	boehmite
29.485	0.30269		201	155	0.5	1573	0.7	0.173	NA
29.976	0.29784		216	350	1.2	1528	0.7	0.074	NA
30.157	0.2961		121	409	1.4	4108	1.9	0.171	NaOH
31.907	0.28025		116	156	0.5	1063	0.5	0.116	NA
32.680	0.27379		120	343	1.1	1635	0.7	0.081	NaOH
33.142	0.27008	104	93	4718	15.7	46576	21.2	0.168	hematite
35.198	0.25476	104	53	30146	100.0	219894	100.0	0.124	corundum
35.658	0.25158		63	3143	10.4	33216	15.1	0.180	hematite
37.819	0.23769	110	0	11290	37.5	78802	35.8	0.119	corundum
38.360	0.23446	031	68	369	1.2	3901	1.8	0.180	boehmite
39.816	0.22621		0	134	0.4	981	0.4	0.124	NA
40.859	0.22068	113	113	1059	3.5	6689	3.0	0.107	hematite
41.711	0.21636	006	22	336	1.1	1603	0.7	0.081	corundum
43.382	0.20841	113	39	26494	87.9	200831	91.3	0.129	corundum
43.754	0.20672	202	64	319	1.1	3480	1.6	0.185	hematite
45.639	0.19861		70	89	0.3	725	0.3	0.138	NaOH
45.703	0.19835		51	105	0.3	828	0.4	0.134	NA
45.984	0.1972	131	50	207	0.7	740	0.3	0.061	boehmite
46.239	0.19618	202	76	359	1.2	2037	0.9	0.096	corundum

Table 4.1. X-Ray Diffraction Data from AZ-101 Washed Runs 1 and 2

2-Theta	d(nm)	hkl	BG	Height	I%	Area[(1)]	I%	FWHM	Possible Assignments
48.777	0.18654	051	41	393	1.3	4399	2.0	0.190	boehmite
48.958	0.1859		83	448	1.5	6748	3.1	0.256	NA
49.402	0.18433	024	110	1203	4.0	20202	9.2	0.285	hematite
49.795	0.18297		81	239	0.8	1770	0.8	0.126	NA
50.043	0.18212		81	186	0.6	660	0.3	0.060	NaOH
50.303	0.18124		39	232	0.8	1759	0.8	0.129	NA
52.579	0.17391	024	25	9960	33.0	79088	36.0	0.135	corundum
54.019	0.16961		45	1438	4.8	16195	7.4	0.191	hematite
57.520	0.1601	116	4	19641	65.2	166047	75.5	0.144	corundum
59.762	0.15461	211	41	417	1.4	2357	1.1	0.096	corundum
61.320	0.15105	122	42	1503	5.0	11702	5.3	0.132	corundum
62.345	0.14881	214	56	534	1.8	7639	3.5	0.243	hematite
63.978	0.1454	300	65	797	2.6	9623	4.4	0.205	hematite

(1) computer output – no rounding was attempted
BG = background. NA = not assigned
I% = relative intensity.
FWHM = full width half maximum.
*Corundum (Al_2O_3) JCPDS 42-1468.

Another sample was run with a small amount of corundum (Al_2O_3) as an internal standard. However, too much of the standard was added to the sample, and the Al_2O_3 peaks dominated the spectrum. These data are presented in the table. There was some concern that the over night drying may have crystallized the aluminum oxide phases. The internal Al_2O_3 standard was used to confirm that the peak positions were accurate in the other spectra.

4.2 Scanning Electron Microscopy of AZ-101 Washed Solids

The sample was shown to be extremely complex under SEM, revealing many different phases that were not detected during the XRD scan. With optical microscopy the particles were mainly yellow and orange in color. The aggregate nature of the particles in AZ-101 made it difficult to determine the true composition of individual phases. Under SEM, individual particle aggregates were 5 to 10 µm in diameter. These larger particles were composed of many fine-grained phases (Figure 4.2 a and b). The characteristic blades (iron rose) of hematite can be seen in Figure 4.2 c and d. These exhibit bright contrast, suggesting a high average atomic number.

In Figure 4.2a, EDS analyses were obtained from an area (EDS03) and a point (EDS04). The resulting spectra were almost identical, suggesting that the Zr-Fe phase composition represents a single phase and not an agglomeration of phases.

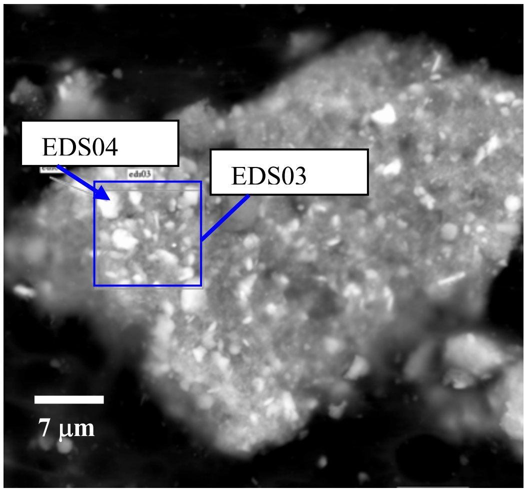

Figure 4.2a. Agglomerated Particle Containing an Al-, Zr-, and Fe-Bearing Phase

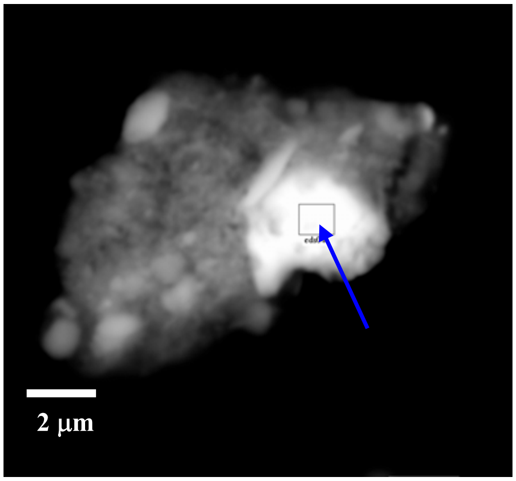

Figure 4.2b. Bright Region Corresponds to a Zr-Rich Phase

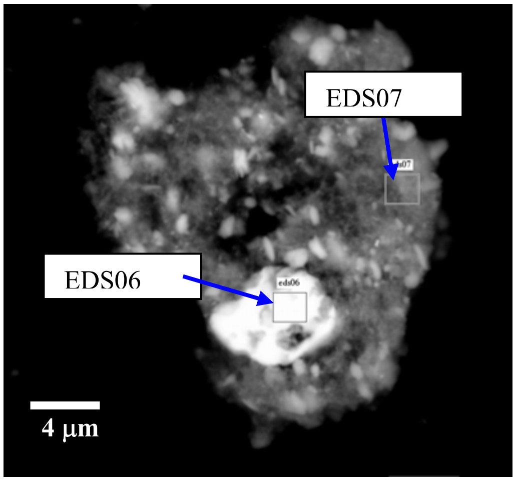

Figure 4.2c. Agglomerated Particle Containing Fe, Al, and Zr; region EDS06 rich in Cd and Sn, region EDS07 contains Fe-Zr-Al phase

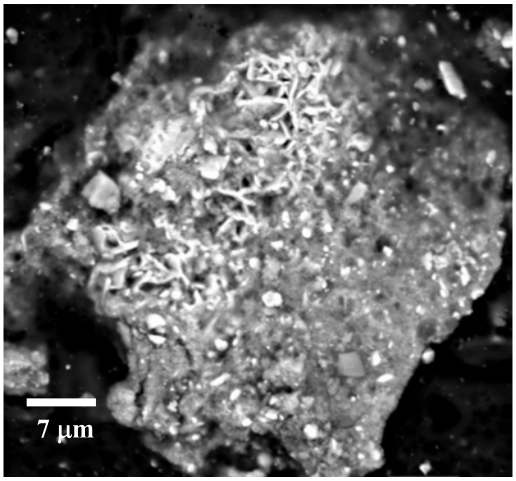

Figure 4.2d. Morphology of Aluminum Oxide Phases at Lower Voltage; consistent with XRD identification of goethite and boehmite

The sample preparation method for microscopy results in the formation of agglomerated particles. These agglomerates form as the solids are de-watered and washed on a dead-end filter. This suggests that the WTP will not see such large agglomerated particles. This process of particle coarsening on a filter contacted with air is observed with both simulant and actual washed solid samples (Tingey et al. 1999).

Cadmium is a minor component in AZ-101 solids, but tin is not reported to be in AZ-101 solids by Urie et al. (2002). However, Figure 4.3a clearly shows the presence of a Sn-Cd phase. This phase was found several times in the SEM sample. Note also the small amount of zinc in the analysis. Zinc is not reported at significant levels in either AN-102 or AZ-101; yet it is clearly present in the analysis of these Fe-Cr particles. Tin was reported in AN-102 and should clearly be present in AZ-101 according to the

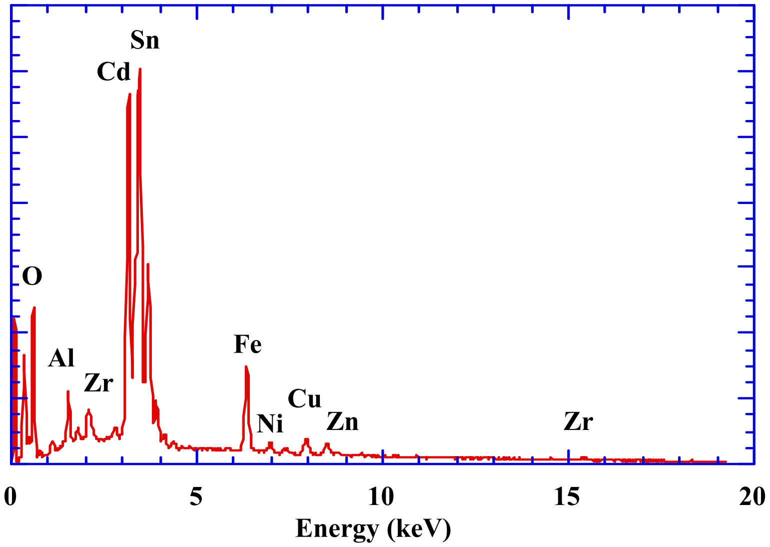

Figure 4.3a. X-Ray Energy Dispersive Analysis of Cadmium-Tin Particles

EDS analysis. The composition of another common phase found in AZ-101 is shown in Figure 4.3b. This phase contains Zr, Fe, and lesser amounts of Al, La, and Nd. Other rare earths may be present but cannot be resolved with SEM-EDS. Zirconium and iron are both major components in AZ-101, and La and Nd are minor components present at about $3x10^3$ and $1.3x10^3$ µg/g solids, respectively. Cerium may also be present but cannot be detected due to overlap problems, and its lower concentration in the washed solids ($5x10^2$ µg/g solid). A possible zirconium-iron phase might be the phosphate. One possible mineral would be mahlmodite [$FeZr(PO_4)\bullet 4(H_2O)$] which has major d-spacings at 0.316, 0.4382, and 0.958 nm.

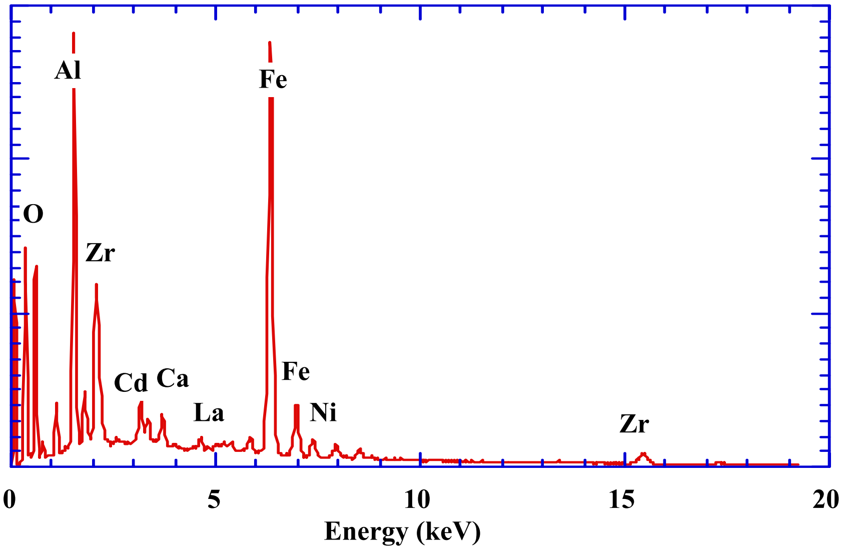

Figure 4.3b. X-Ray Energy Dispersive Analysis of Particle Showing the Presence of Al, Fe, and Zr; the phase is compositionally similar to Zr-bearing phases reported by Lumetta et al. (1996)

The XRD was not inconsistent with this; however, the XRD data are not conclusive. It is possible that phosphate groups can be exchanged for carbonate, aluminate, or even sulfate groups. Because the P-K line overlaps strongly with the Zr-L lines, further analysis with infrared spectroscopy and computer simulations was done to establish the composition.

Although the carbon signal in Figure 4.3b from the Zr-Fe phase was exceptionally high, this cannot be used for evidence of carbonate. Generally, as the probed area increases the carbon signal will increase due to the conducting carbon coating added during sample preparation. There is severe overlap of the P-K x-ray line with the Zr-L lines. The total concentration of zirconium in AZ-101 is about 3×10^4 µg/g, and the total concentration of lanthanum is about 3×10^3 µg/g solid. Semi-quantitative analysis of the Fe-Zr oxide phase suggests that the La content is ~10% the zirconium content (see Table 2.2). This suggests that the vast majority of lanthanum must be associated with this phase. Lumetta et al. (1996) report the presence of an amorphous zirconia phase, and their EDS spectrum also indicated the presence of iron and was similar to the spectrum shown in Figure 4.3b. More detailed analysis of the minor components in this phase was performed.

In Figure 4.4, an SEM image of a uranium oxide particle is shown. Only one such particle was observed during the investigation; however, similar phases were observed in AN-102. Schoepite (uranyl oxide hydrate) phases have been reported by Lumetta et al. (1997); however, the particles in this study do no possess a morphology consistent with a uranyl oxide hydrate. Particles of Fe-Cr oxide (chromite) and lead were also observed in AZ-101 washed solids.

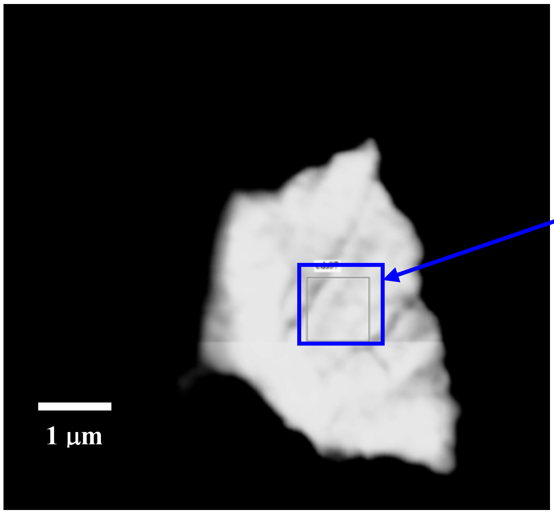

Figure 4.4. (a) SEM Image of Euhedral Uranium Oxide Particle

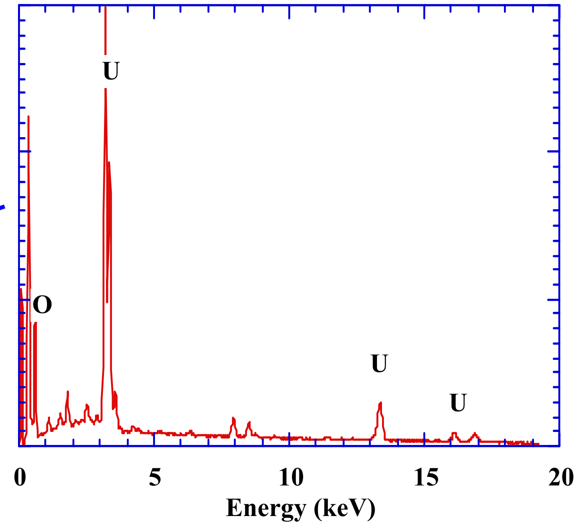

Figure 4.4b. EDS Analysis of the Uranium Phase

The aggregates shown in Figures 4.5a and b were typical of the types of particles observed in the AZ-101 SEM sample. The lighter contrast material tended to be aluminum-rich, consistent with the identification of various Al-bearing phases with XRD. However, the brighter regions that reflect the presence of high-Z materials contained U, Cd, La, Nd, and Zr.

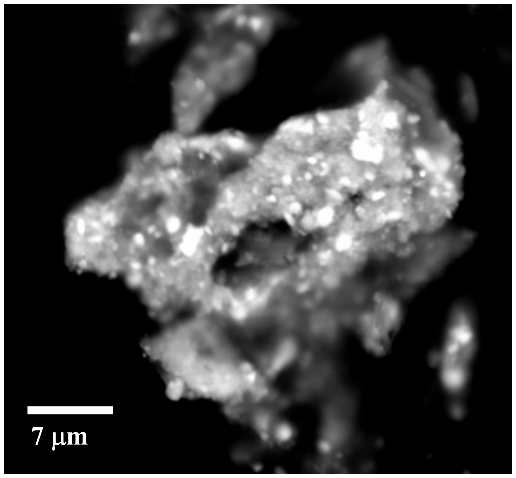

Figure 4.5a. SEM of Particle Typical of Second Sampling of AZ-101 Solids Prepared for Microscopic Characterization

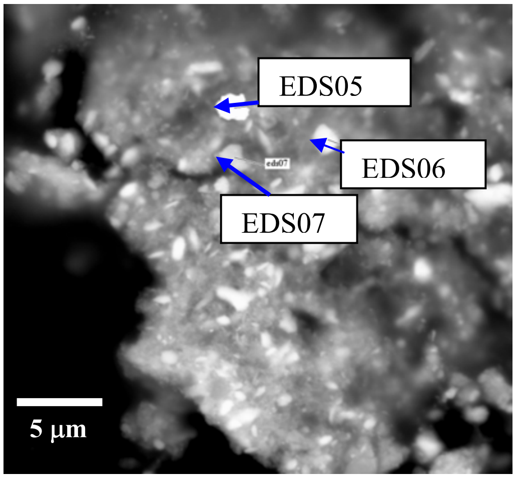

Figure 4.5b. SEM Showing Heterogeneous Aggregate Consisting of Several Phases; regions labeled EDS05 and EDS06 were iron zirconium aluminate phase; probe of region EDS07 revealed particle was uranium oxide.

In Figure 4.6, an experimental EDS analysis of the minor elements in the Fe-Zr phase, possibly with several other minor phases, is shown along with a simulated spectrum (line) of 10 elements (Na, Al, Si, Zr, Ru, U, Ca, La, Mo, Cr, Fe, Ni, Cu, and Zn. There was reasonable agreement with the experimental and a computer simulation, although it was not possible to completely model the background of the experimental analysis. This analysis indicated that the ruthenium was present in the AZ-101 washed solids sample and that it was associated with the Zr-bearing phase.

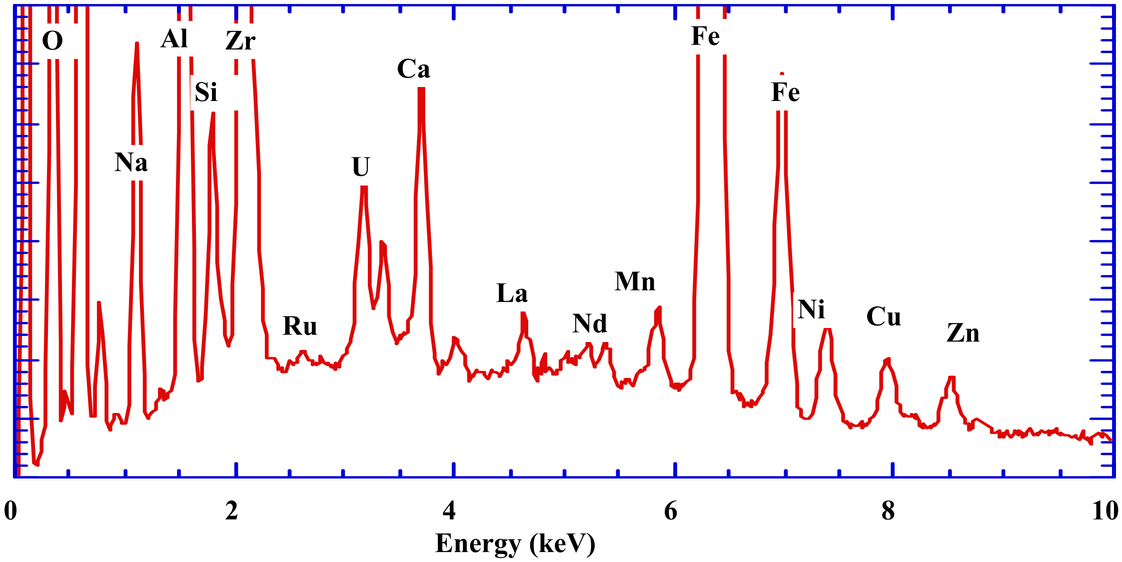

Figure 4.6. Trace Elements in AZ-101 Washed Solids

4.3 XRD Analysis of AZ-101 Unwashed Solids Sample

Sample AZ-101 unwashed represents material that had not yet gone through the first stage of washing. The XRD scan and list of d-spacings are shown in Table 4.2 and Figure 4.7, respectively. The phases found in the SEM study were not consistent with the single XRD run. A liquid separation of the sample was run to isolate the denser phases of interest. However, only a small amount of material was isolated, so the run did not yield any new information.

Table 4.2. XRD Data from AZ-101 Unwashed Solids

2-Theta	d(nm)	BG	Height	I%	Area	I%	FWHM	Possible Assignments
11.707	0.75532	19	107	1.3	302	1.5	0.120	NA
14.500	0.61036	38	463	5.6	2869	14.3	0.263	boehmite
18.332	0.48356	24	8236	100.0	20005	100.0	0.103	gibbsite
20.317	0.43673	67	2274	27.6	4983	24.9	0.093	NA
28.172	0.31649	57	164	2.0	409	2.0	0.106	boehmite
29.410	0.30345	30	3021	36.7	8109	40.5	0.114	NaOH, nitratite
30.028	0.29735	47	766	9.3	1740	8.7	0.097	NaOH
31.441	0.2843	30	47	0.6	215	1.1	0.194	NA
31.893	0.28037	48	450	5.5	1194	6.0	0.113	nitratite
32.378	0.27628	48	193	2.3	741	3.7	0.163	NA
33.167	0.26988	67	594	7.2	2699	13.5	0.193	hematite
34.101	0.2627	56	125	1.5	291	1.5	0.099	NA
34.501	0.25975	57	2293	27.8	4683	23.4	0.087	NA
35.431	0.25314	54	451	5.5	1179	5.9	0.111	hematite
36.699	0.24468	11	127	1.5	306	1.5	0.102	NaOH
39.015	0.23067	0	375	4.6	921	4.6	0.104	nitratite
40.863	0.22066	0	62	0.8	172	0.9	0.118	hematite
44.506	0.2034	33	1071	13.0	3424	17.1	0.136	gibbsite
46.870	0.19368	28	336	4.1	707	3.5	0.089	NA
47.925	0.18966	20	478	5.8	1616	8.1	0.144	nitratite
48.359	0.18806	12	213	2.6	535	2.7	0.107	NaOH
53.558	0.17096	31	88	1.1	193	1.0	0.093	NA
54.121	0.16932	32	131	1.6	650	3.2	0.211	hematite
55.655	0.16501	34	150	1.8	440	2.2	0.125	boehmite
58.616	0.15736	16	114	1.4	209	1.0	0.078	NA
62.437	0.14862	20	129	1.6	363	1.8	0.120	hematite
63.940	0.14548	41	98	1.2	202	1.0	0.088	hematite

BG= background, NA = not assigned.
I% = relative intensity.
FWHM = full width half maximum.

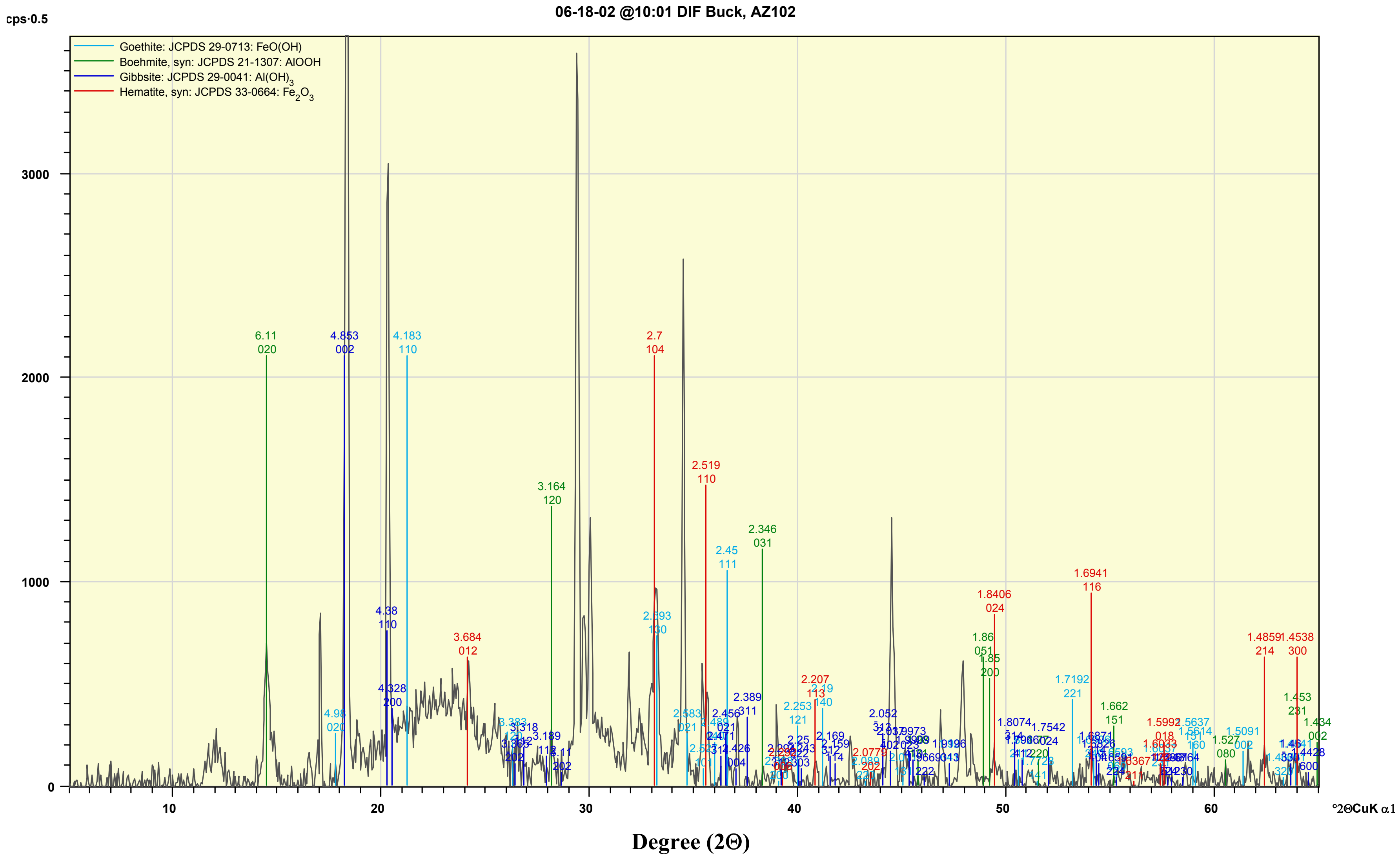

Figure 4.7. XRD Scan, Background Subtracted, of Unwashed AZ-101 Solids. Four phases are identified; several major peaks remain unidentified.

4.4 Scanning Electron Microscopy of AZ-101 Unwashed Solids

The unwashed solids of AZ-101 were significantly more radioactive than any of the other samples examined. The sample size had to be reduced several times to comply with radiation limits for the instruments. The particles in Figure 4.7 are clearly agglomerated; however, this is not believed to be representative of the form of solids during actual waste processing. The process of drying on a filter exposed to air results in the formation of these soft agglomerates. A few particles were placed on a sticky carbon film, coated with a thin-layer of conducting carbon, and examined in the JEOL840 SEM in the 326 Building. These images are shown in Figures 4.8 through 4.14.

The SEM images in Figure 4.8b and c show large particle agglomerates. On closer inspection these agglomerates appear to consist of much finer particles. The high-Z, white contrast particles are <0.3 µm in diameter. The agglomerates most likely formed during the sample preparation process and do not represent the anticipated size of particles that will be seen during waste processing. The fibrous particles in Figure 4.9 contained sodium, potassium, and oxygen.

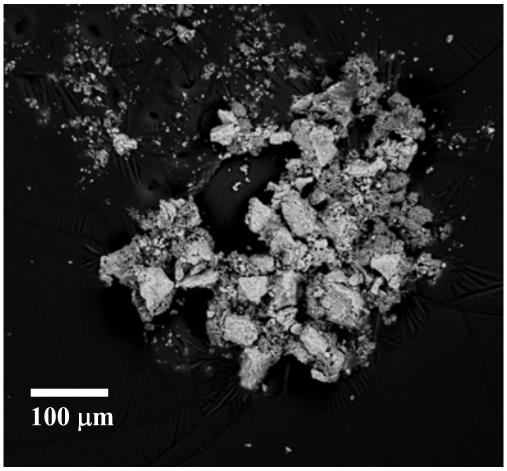

Figure 4.8a. Low Magnification View of Collection of Particles from Unwashed AZ-101

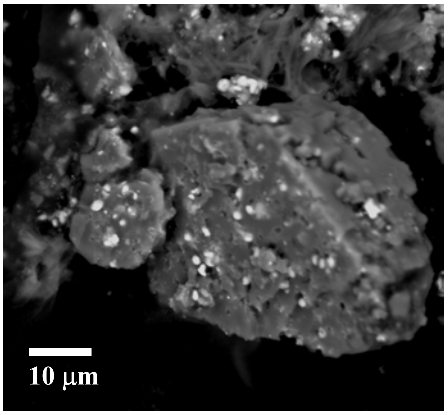

Figure 4.8b. Particle Aggregate from Unwashed AZ-101

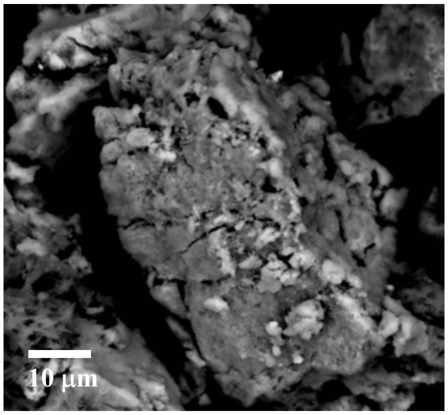

Figure 4.8c. High Magnification of Particles

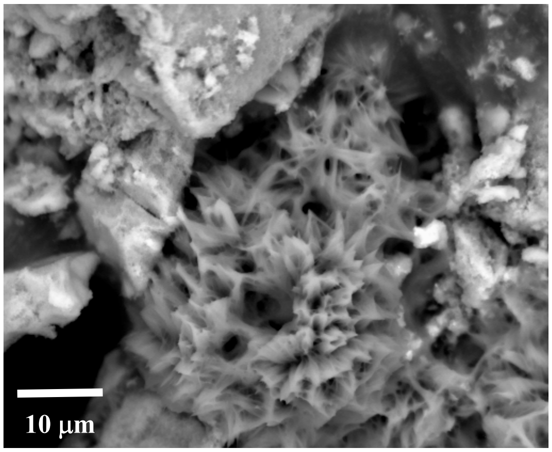

Figure 4.9. SEM Image of Sodium-Bearing Fibrous Phase

Nickel, copper, manganese, and trace zinc were detected in Region 2 in Figure 4.10. The level of zinc is similar to that of copper in the spectrum; however, zinc is not reported as a significant component in AZ-101 solids (Urie et al. 2002). In Figure 4.10a, Region 1 was aluminum oxide (Ref: EDS02), Region 2 an iron aluminate (Ref:EDS03) (see Figure 4.10b), and Region 3 an aluminum oxide (Ref: EDS01).

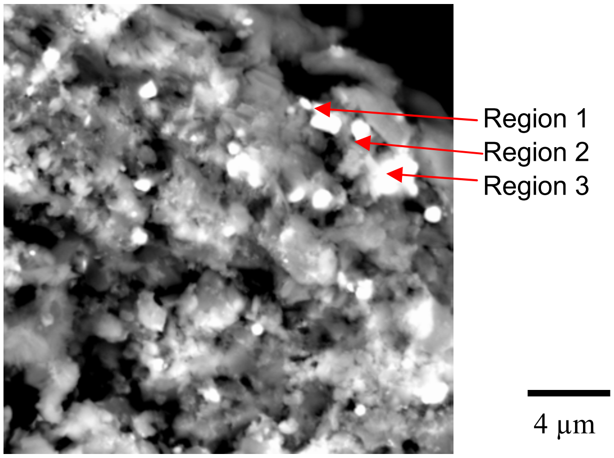

Figure 4.10a. Series of AZ-101 Particles Consisting of Aluminum

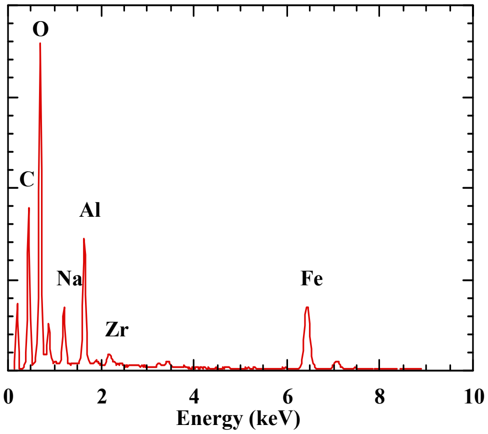

Figure 4.10b. EDS analysis of Region 2

The phases shown in Figure 4.11 were composed of iron and oxygen. The particle morphology was characteristic of hematite (Fe_2O_3). Crystals of hematite are often arranged like petals of a rose (so-called iron-rose). These particles were also observed in the washed samples (Ref: EDS04).

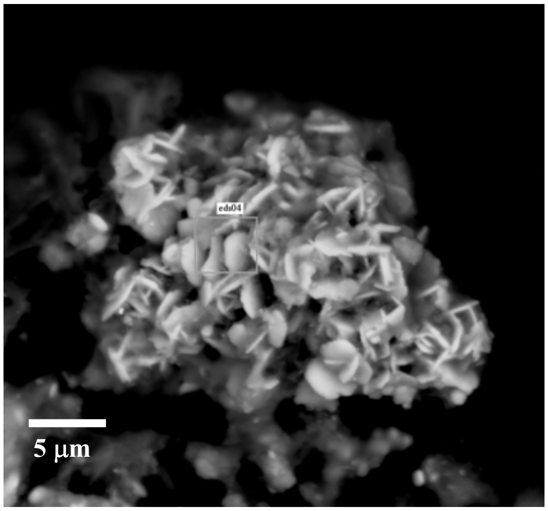

Figure 4.11. Blade-Like Phases of Hematite

The particles within these regions appeared to consist of particle agglomerates. For instance, in Figures 4.12 and 4.13a, the individual particles are submicron. The composition of the phase shown in Figure 4.12b was consistent with manganese clay minerals containing both K and Na (Chukhrov et al. 1980).

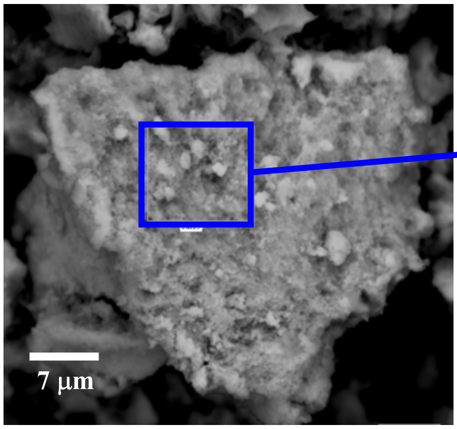

Figure 4.12a. SEM of Manganese-Bearing Phase in AZ-101

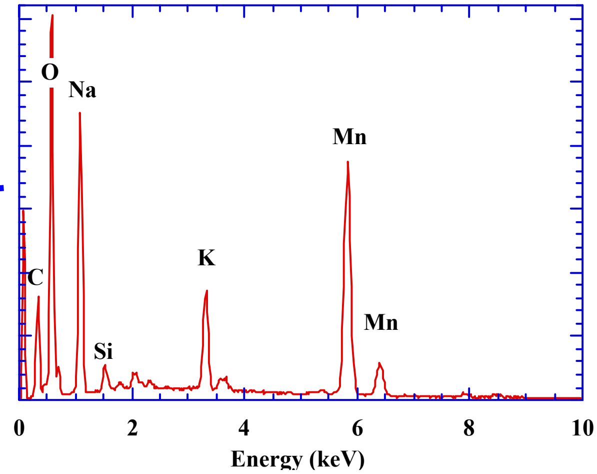

Figure 4.12b. EDS Analysis of Phase Showing Presence of Potassium, Manganese, and Oxygen

The Sr-L and Si-K peaks overlap strongly, the overall peak shape fits Si more precisely; in addition, the higher energy peak, Sr-K, was absent. The phase also contains La and Nd. Other rare earths may be present but overlap strongly in this region. This phase was also observed in the washed sample where it was observed more commonly than in the unwashed sample.

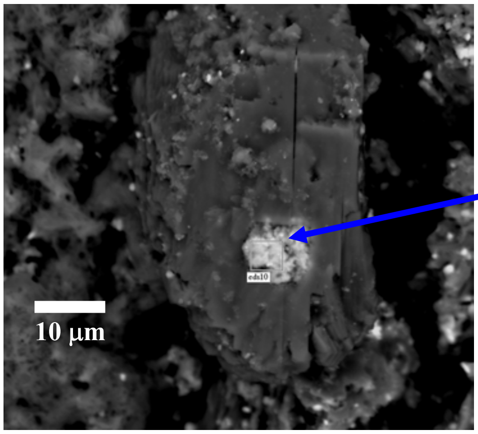

Figure 4.13a. Small Region with High-Z Material Dominated by Iron and Zirconium

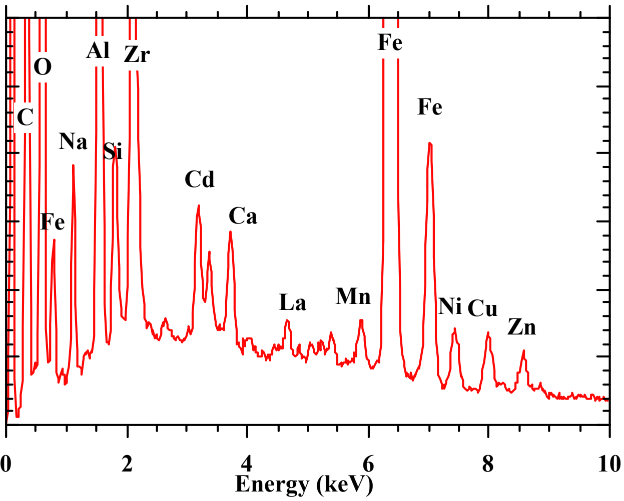

Figure 4.13b. EDS Analysis

A search was made for evidence of strontium, which is present at about $6x10^2$ µg/g solid in AZ-101. The washed solids had a high beta-radiation field, presumably due to ^{90}Sr and ^{90}Y, but, to detect strontium with EDS it would need to be locally concentrated to at least 1 wt%. This detection level was confirmed through computer simulation of EDS analyses. The sorption of strontium from 0.05 M $NaNO_3$ solution onto hydrous zirconium oxide was measured as a function of pH by Venkatesan et al. (2001). Modeling the sorption and speciation of Sr^{2+} on H_2O indicated that the hydrolysis of Sr^{2+} to the lower-charged $SrOH^+$ is a prerequisite for the abrupt increase in sorption above pH 9. Hence, it was thought that locally high concentrations of Sr may be present on the zirconium-rich phases in the AZ-101 sample. Strontium produces a strong x-ray line at 1.806 keV, close to the Si-K line at 1.740 keV. With the energy resolution of the EDS system on the SEM it was possible to resolve these energies and demonstrate that Sr was not present at detectable levels. The weaker high energy line at 14.164 keV can overlap with plutonium.

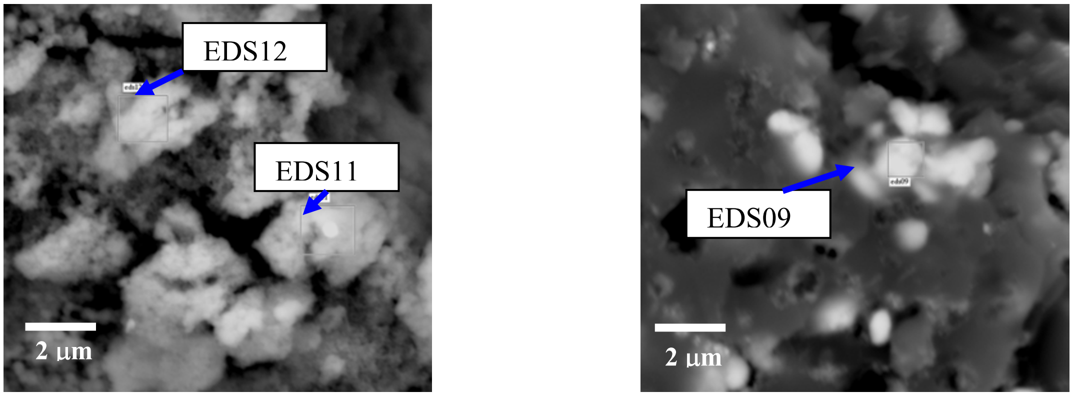

Figure 4.14a,b. SEM Image of a Cluster of Manganese-Bearing Particles; analysis with EDS (EDS11 and EDS12) indicated the phase was possibly birnessite related; white particles in (b) are Fe-Zr bearing.

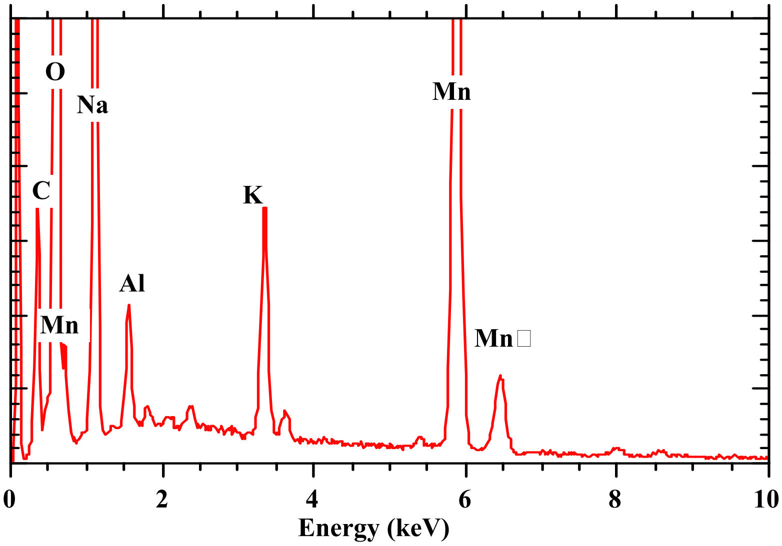

Figure 4.14c. EDS Analysis of Phases in Figure 4.14a

Manganese phases were commonly observed in the unwashed solid sample. The phase was agglomerated with a fluffy texture; the individual particles were 0.3–0.5 µm in diameter. Compositionally, the phase matched a manganese clay mineral such as birnessite (see EDS12 in Figure 4.14c). These phases exhibited lighter contrast than the bulk material. The EDS analyses of these types of phases yielded a relatively pure single-phase composition. However, manganese is a minor component of AZ-101 solids (~1x10^2 µg/g solid), suggesting that there may have been problems obtaining representative samples in this case. Manganese was not detected in any other phases.

4.5 Infrared Spectroscopy of Washed AZ-101

A section of the infrared spectrum from the AZ-101 washed solids is shown in Figure 4.15. The absorption bands are in a region most consistent with nitrate, carbonate, sulfate, aluminate and/or phosphate. The largest absorption signatures are likely due to a phosphate species because large absorption signatures for nitrates, carbonates, and sulfates typically appear at energies higher than 1100 cm^{-1}. The absorption does not appear to be due to a pure salt or mixtures of pure salts.

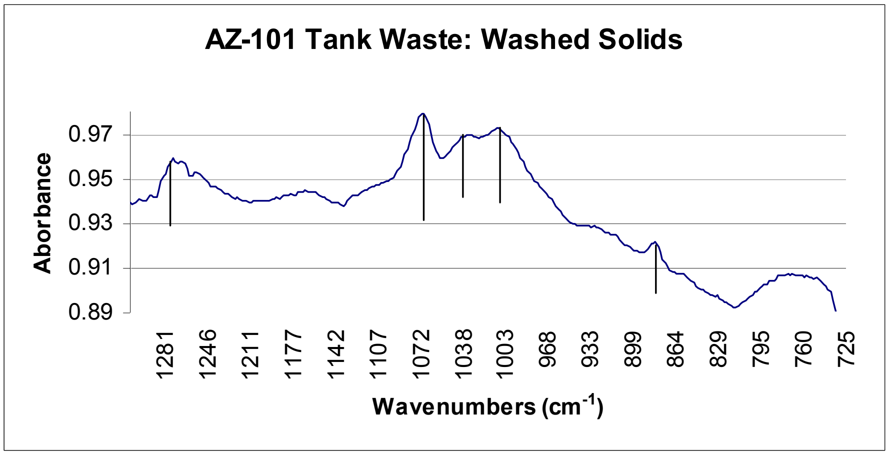

Figure 4.15. Infrared Spectrum of AZ-101 Washed Solids in Potassium Bromide

4.5.1 Absorption band identification

A short investigation was performed to establish the identity of the major components in this spectrum (Figure 4.15). First, the compositional make-up of the solids was determined from data provided by Urie et al. (2002) (see Table 2.2). The washing procedure removed all metal nitrates, soluble oxides, and sodium carbonate. Less-soluble fluoride, phosphate, carbonate, and sulfate double salts may persist; although, these should leach out with dilution. Pure insoluble metal oxides such as rare earth oxides and actinides oxides, MnO_2, Fe_2O_3, and ZrO_2, typically have absorption bands below 600 cm^{-1}, which is outside the range of the spectrum, but they also have a sharp distinctive band near 1200 cm^{-1}.

To further reduce possible candidates, several pure salts were run as KBr pellets. The most relevant of these are listed in Table 4.3. Additionally, five double salts were prepared in deionized water (see Table 4.3). The infrared spectra of these double salts are illuminating in that they suggest the sort of perturbation that will occur in the spectrum relative to the pure salts. These might then be relevant to understanding the degree to which the mixed phases (that likely occur in the tank waste solids) will influence the infrared spectrum.

A large number alumino-silicates or sulfates could potentially be formed hydrothermally in the tank waste. In the laboratory, heating of mixtures of aluminate with silica-based materials below 150°C can lead to formation of mineral phases. Examples of these are cancrinite, which forms with kaolin, and sodium nitrate heated in caustic, or the alunites, which readily form when $(NH_4)_2 SO_4$, Na_2SO_4, or K_2SO_4 are heated with $Al_2(SO_4)_3$. As is shown, the infrared spectrum of the AZ-101 solids appears to be most consistent with an insoluble phosphate, sulfate, or silicate phase. While the oxides and hydrous oxides $Zr(OH)_4$, Fe_2O_3, and UO_2 are clearly present in the solids, they have no major diagnostic bands in the 700 to 1330 cm^{-1} regions.

The compositional data suggest that the phosphate concentration is lower than that of silicate, carbonate, or sulfate. While the absorption maxima of pure aluminate and sulfate salts are generally higher than 1100 cm^{-1}, many alumino silicates, alumino sulfates, and other mineral silicates absorb between 950 and 1100 cm^{-1}.

4.5.2 Anion symmetry and coordination modes

The positions of the oxides, fluorides, nitrates, carbonates, or phosphates are seen not to dramatically shift with metal. The metal coordination often results in a reduction in the anion symmetry and causes degenerate vibrations to become non-degenerate. This means that vibrations having the same energy are decoupled to produce multiple molecular vibrations, some of which are infrared active. For $NaNO_3$, the spectrum is a single broad band, which indicates monodentate coordination of trigonal planar nitrate. In the spectrum of lanthanum nitrate, for instance, two bands appear, separated by 150 cm^{-1}. This separation indicates bidentate coordination of the nitrate. Similar effects occur for trigonal planar carbonate and tetrahedral sulfate.

The double salts show similar behavior, but the splitting is not large enough to be consistent with bidentate coordination. The sodium double-salt spectrum in Figure 4.16a shows the splitting in the nitrate and sulfate signatures. This indicates alternate coordination to one sodium or to bridged metals in these salts. The important observation with regard to the spectrum of AZ-101 is that none of the major bands for aluminate, oxalate, carbonate, sulfate, or nitrate pure salts or double salts match the observed spectrum. The spectrum of trisodium phosphate, calcium phosphate, and the $Na_7F(PO_4)_2.19H_2O$ double salt are in the appropriate region, but the band positions in these salts do not match the prominent bands in the tank waste spectrum. A much closer match is seen in the spectrum of the zirconium phosphate. This spectrum is superimposed on the AZ-101 washed sample spectrum in Figure 4.17. There are three similar absorbance bands between these two spectra. The near match in position of these bands suggests that this is a major phase in the sample, in agreement with the SEM study. But there is apparently more than this simple phosphate phase. The SEM investigation found no evidence of a pure zirconium phosphate phase in washed AZ-101.

Further evidence is provided by the sharp bands centered around 850 cm^{-1}. The tank waste spectrum has a similar band at 883 cm^{-1}. A sharp absorption band is seen for nitrate (837 cm^{-1}), carbonate (883 cm^{-1}), and aluminate (860 cm^{-1}) species. This band shifts only 10–20 cm^{-1} for substitution by other metals common to the AZ-101 composition, i.e., Al, Na, Zr, Ca, and La. The effect on the band due to the $Na_3NO_3SO_4$ double-salt coordination is again seen in Figure 4.16 to be about 3 cm^{-1}.

The nitrate salts, including zirconium nitrate, are soluble. This leaves an insoluble carbonate or aluminate species. The exact match with sodium carbonate at this band position may be fortuitous, however, an insoluble zirconium carbonate species is a reasonable candidate because the zirconium concentration in the solids is dominant. The aluminum concentration is also high, so an insoluble aluminate should not be ruled out. Unfortunately, the major bands (near 1400 cm^{-1}) in the spectra of zirconium or other metal carbonates or aluminates are outside our observation window. Again, the SEM evidence suggested that Al is present in the zirconium phase and there may also be evidence for carbon. A last band near 1240 cm^{-1} is similar to ZrF_4 which can be seen as an impurity in the $Zr_3(PO_4)_4$ spectrum.

The infrared spectrum of the AZ-101 washed solids is consistent with a mixed phase containing at least zirconium phosphate. The phase likely contains other insoluble phosphates such as Ca or La, which give the band structure its complexity. Both La and Ca were identified in association with the Zr-bearing phase in the washed AZ-101 sample with SEM-EDS. ZrF_4 may be present in the sample, consistent with a relatively high fluoride concentration in AZ-101 but not with XRD or SEM data. The presence of carbonate or aluminate species is also suggested by the infrared data and backed up by SEM-EDS data.

Table 4.3. Potential Compounds and Their Infrared Bands

Sodium oxalate [$Na_2C_2O_4$]	1321, 781, 775(w)
Potassium oxalate [$K_2C_2O_4$]	1315, 780, 721
Sodium nitrate [$NaNO_3$]	1364, 836
Sodium nitrite [$NaNO_2$]	1326, 1264, 827
$Na_3NO_3SO_4$	1371, 837
Nitrated zeolite-A (ideally $Na_{12}Al_{12}Si_{12}O_{48}\bullet 27H_2O$)	1268, 1000,732, 708, 664
Sodium aluminate [$NaAlO_4$]	1453, 867
Strontium aluminate [$Sr(AlO_4)_2$]	1452, 1091, 859, 706, 698
Lanthanum carbonate [$La_2(CO_3)_3$]	1434, 870, 847
Sodium carbonate [Na_2CO_3]	1440, 879, 702, 694
Manganese carbonate ($MnCO_3$)	1430,1074, 863, 726
$Na_6(SO_4)_2CO_3$	1452, 1110, 990, 876, 636
Sodium phosphate [$Na_3(PO_4)_3$]	1266, 1122, 1066, 992, 867, 820, 617
Calcium phosphate [$Ca_3(PO_4)_2$]	1091, 1032, 600
Aluminum phosphate ($AlPO_4$)	1120
Lanthanum phosphate [$La(PO_4)$]	1053, 1009, 617
Zirconium phosphate [$Zr_3(PO_4)_4$]	860, 774
$NaF(PO_4)_2.19H_2O$	1008, 987, 744, 698
Sodium sulfate (Na_2SO_4)	1123, 635, 613
Aluminum sulfate [$Al_2(SO_4)_3$]	1103, 927, 705
Gypsum ($CaSO_4$)	1150, 670, 600
Na_3FSO_4	1144, 629
Ferrous sulfate ($FeSO_4$)	1102, 988, 612
Ferric sulfate [$Fe_2(SO_4)_3$]	1198, 1098, 1083, 640
Zirconium hydroxide [$Zr(OH)_4$]	1338, 1098, 1050, 851, 781

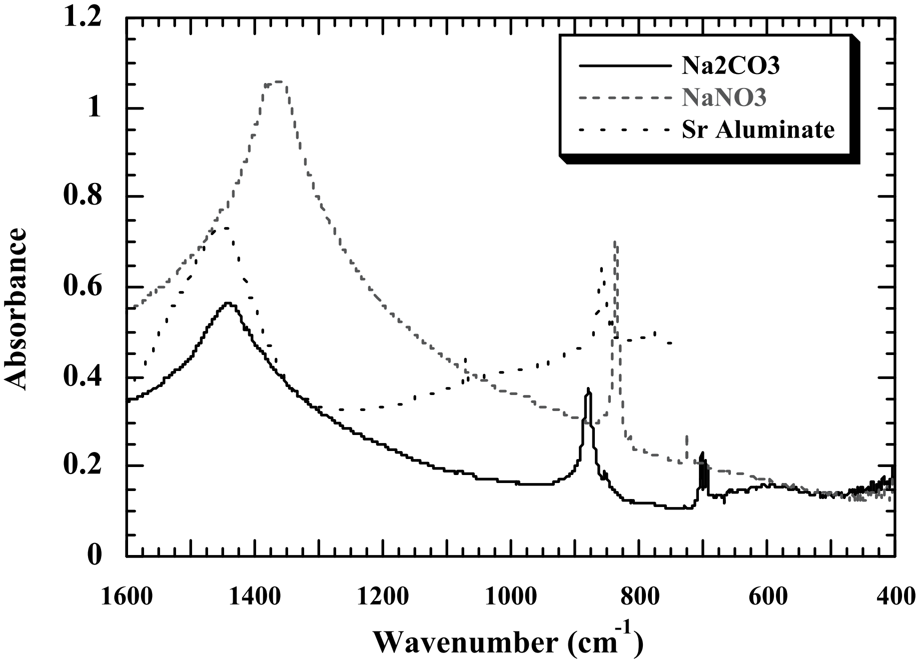

Figure 4.16a. Infrared Spectra of Na_2CO_3, $NaNO_3$, and Aluminate

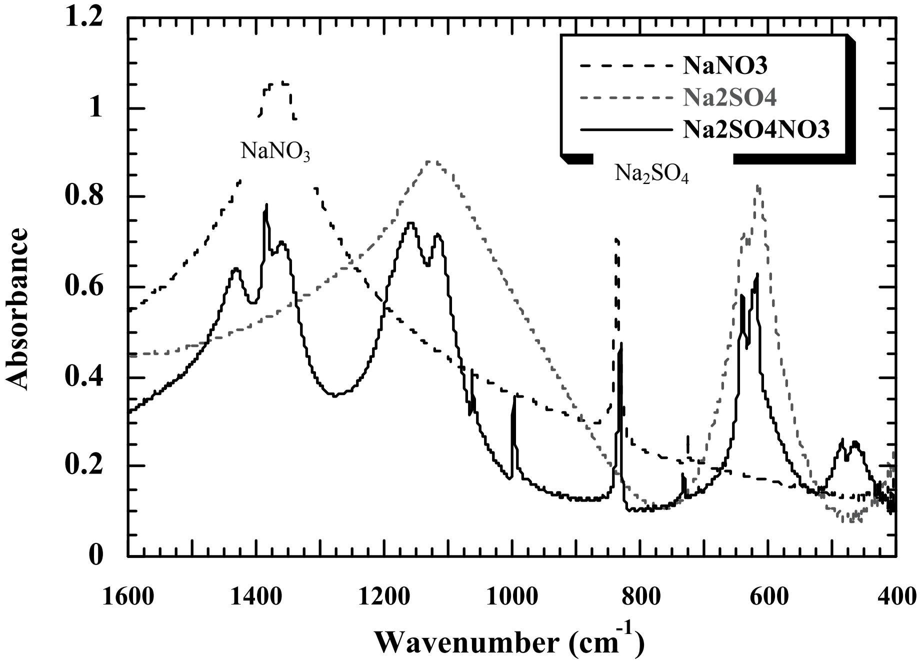

Figure 4.16b. The Double Salt $Na_3NO_3SO_4$

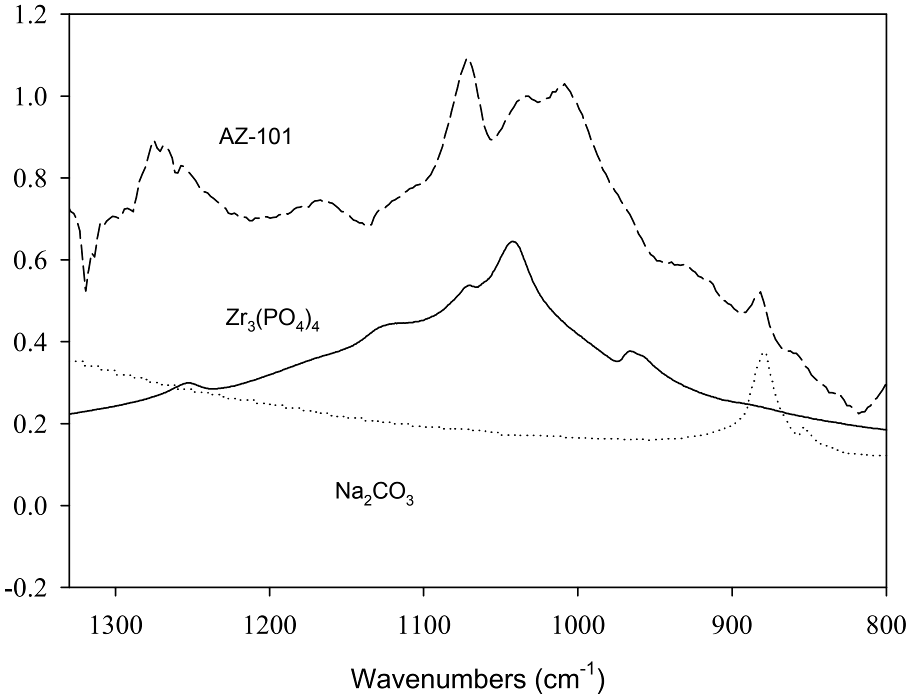

Figure 4.17. Spectra of AZ-101 and Candidate Inorganic Salts

5.0 Discussion

There are surprisingly few major phases in the tank wastes in spite of the compositional diversity. Tingey et al. (1999) expressed similar conclusions regarding characterization of phases in Hanford Tank 241-C-112. Krumhansl et al. (1999) produced simulated tank sludges with many of the same phases that were observed in AN-102 washed solids and AZ-101 washed and unwashed solids. In particular, zeolites, boehmite, hematite, and hydrotalcite have been formed in artificial sludges.

5.1 Zeolitic and Carbonate Phases

Thermodynamic analyses of Hanford tank wastes indicate that analcime and Na-clinoptilolite, rather than cancrinite or nepheline, would be stable Al- and Si-bearing solids (Krumhansl et al. 1999) (Figure 5.1). The circled region represents tank compositions.

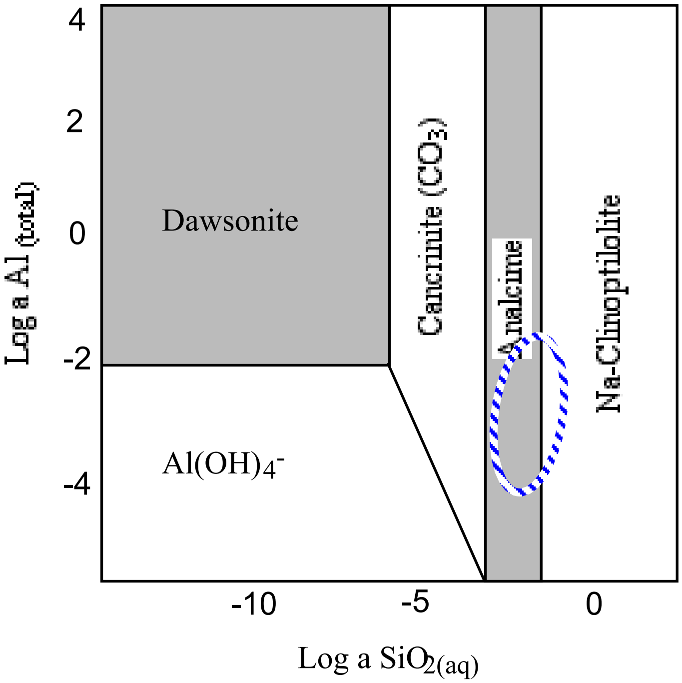

Figure 5.1. Activity Diagram for Hanford Tank Fluid Compositions (from Kumhansl et al. 1999)

Although cancrinite has been reported in tank wastes, there is no evidence that these phases were present in the AN-102 washed solids examined in this study. Cancrinite is a feldspathoid, related to alkali feldspars but deficient in silica and having less open structures than zeolites. Cancrinite is not a zeolite although it is structurally, very similar.

XRD studies of AN-102 waste were performed by Lumetta et al. (2001). They reported the presence of $NaNO_3$, $NaNO_2$, gibbsite, $Ba_2C_2O_4$, and zeolites. The zeolite thought to best fit the data was the synthetic phase zeolite-Y ($K_{48.2}Al_{48.2}Si_{143.8}O_{384}$). The XRD also revealed a peak at 38.82 degree 2-theta angle that could not be matched. Zeolites have also been formed in artificial sludges in laboratory experiments by Krumhansl et al. (1999). Jantzen et al. (2002) reported that reactive oxides, soluble silicates, and soluble aluminates can form sodium alumino-silicate (NAS) hydrogel that converts to zeolite-A (ideally $Na_{12}Al_{12}Si_{12}O_{48}\bullet 27H_2O$) under hydrothermal conditions at elevated temperatures, and eventually to sodalite (cubic), and finally to cancrinite (hexagonal). The zeolite was nitrated (i.e., some H_2O groups are replaced with NO_3^- in the structure). In nature, both nepheline and cancrinite are found in igneous rocks and generally require high temperatures and pressures to form, although Mattigod et al. (2002) have produced cancrinite in the laboratory by hydrothermal synthesis at 80°C. Conditions present in the Hanford tanks should tend to favor the formation of zeolites because these precipitate readily under low-temperature hydrothermal and/or high-pH conditions, for example, during borosilicate glass dissolution at high pH (Abdelouas et al. 1997). The morphology of the alumino silicate phases and the limited XRD data support the identification of zeolites in the sample. The zeolites present may not be found in the powder diffraction database (diffraction spacings are less accurate at the high d-spacings); however, the closest match appears to be laumontite or heulandite.

In AN-102, most of the sample consisted of a matt of aluminum and sodium. The SEM samples are coated with carbon to make them conductive, and the intensity of the carbon signal in the x-ray spectrum increases as the area probed increases. Because inorganic carbon is known to be a major component in the washed solids, carbonate phases should be present. One possible sodium alumino-carbonate phase is dawsonite [ideally $NaAlCO_3(OH)_2$]. Dawsonite has been predicted by Krumhansl et al. (1999) to form under high Al and low $SiO_{2(aq)}$ activities (see Figure 5.1). Comparison with the XRD data (see Table 3.1) revealed peaks at 0.592, 0.278, 0.260, and 0.200 nm that agree reasonably with the major reflections from dawsonite. There are no other major phases with this composition in the JCPDS database. The morphology of dawsonite is typically acicular or fibrous spheres, and rosettes; however, the phase can occur as random aggregates, as may be the case here.

5.2 Aluminum Oxide Phases

Aluminum species constitute a predominant proportion of the washed solid tank wastes. The complex chemistry of aluminum in alkaline HLW has recently been investigated in simulants by Johnston et al. (2002). They used infrared and Raman spectroscopy to study the immediate coordination sphere of aqueous Na^+, OH^-, and $Al(OH)^{4-}$ species as well as bound water contained in the hydrated solid phases (e.g., sodium aluminate). This study was useful for analyzing the infrared data on AZ-101 washed solids in this study. Sodium aluminate ($Na_2Al_2O_3(OH)_2\bullet 1.5H_2O$) is known experimentally to be a major phase in alkaline HLW (Johnston et al. 2002). Current understanding of the ternary system for Al_2O_3-Na_2O-H_2O indicates that gibbsite may preclude the formation of sodium aluminate. Indeed, Johnston et al. (2002) claim that gibbsite, although initially predicted by some models, is not observed in Hanford tank wastes. However, we see clear evidence, at least in AZ-101, for the presence of both boehmite and gibbsite. Gibbsite was also observed by Tingey et al. (1999) in Hanford tank 241-C-112. In this study, gibbsite was not found in AN-102 washed solids, but a sodium aluminate was observed with SEM-EDS.

Boehmite (AlOOH) has been identified in TEM studies of some Hanford tank waste by Krumhansl et al. (1999). The phase was identified by its hexagonal platelet-like morphology. Boehmite is sometimes observed to be fibrous or acicular, so such observations are not necessarily diagnostic. However, boehmite will precipitate as rhombohedral plates changing over to more hexagonal-like plates in the presence of nitrate (Music et al. 1998). The morphology of gibbsite crystals evolves from thin, rounded hexagons and faceted lozenges into faceted plates and blocks with well-formed basal prismatic faces. Caustic conditions, not just reaction time, are known to lead to formation of larger crystals. If boehmite (AlOOH) dominates over gibbsite a gel may be formed, preventing wastes from being removed from the tanks or easily transferred through the various pipelines. When boehmite is present in excess, dispersion and re-agglomeration processes "fluff-up" agglomerates, whereas when gibbsite is in excess, the small boehmite particles can become attached to the larger particles and will not contribute to changing the density of the solids (Tingey et al. 1999).

The broad peak in the XRD spectra from both the AN-102 and AZ-101 samples near 15° is characteristic of boehmite (Table 5.1). In AN-102 these peaks appear broader, and gibbsite is absent. In AZ-101, all the boehmite XRD peaks were also broad, suggesting the material is poorly crystalline, unlike the gibbsite. The characteristic peaks from gibbsite in AZ-101 were large and sharp; however, this does not suggest that there is significantly more gibbsite than boehmite. With the available data, it is simply not possible to quantify the relative amounts of different phases. Many of the other d-spacings are common to a series of Al oxide phases, including diaspore; however, there were distinct peaks that allow positive identification of the Al-bearing phases.

Table 5.1. Crystal Chemical Data for Aluminum Oxide Phases

	Name	**Major d-Spacings (nm)**			
α-Al_2O_3 (α-aluminum oxide)	corundum	2.09	2.55	1.60	3.48
α-$Al(OH)_3$ (α-aluminum hydroxide)	gibbsite	4.85	4.37	2.39	4.32
β–$Al(OH)_3$ (β-aluminum hydroxide)	norstrandite	4.79	2.27	4.32	2.39
β–$Al(OH)_3$ (β–aluminum hydroxide)	bayerite	2.22	4.71	4.35	1.72
β-AlOOH (β–aluminum oxyhydroxide)	diaspore	3.99	2.32	2.13	2.08
γ-AlOOH (γ-aluminum oxyhydroxide)	boehmite	6.11	3.16	2.35	1.86

Evidence from SEM did not indicate the presence of Al-O phases because all aluminum-bearing particles observed also contained sodium at the spatial resolution of the SEM instrument (~1 μm^3). It is also important to remember that the SEM sample size was small relative to the XRD samples and that the technique used, backscattered imaging, tends to highlight the high-Z particles. There is some concern that the drying process adopted for AZ-101 could have resulted in increased levels of gibbsite at the expense of boehmite. We cannot rule out the possibility that the gibbsite in AZ-101 formed during the drying in the hot cells before the SEM and XRD samples were prepared, although this is unlikely.

In Figure 5.1, an example of one typical activity plot extracted from Krumhansl et al. (1999) shows some of the Al-bearing phases predicted to form at pH 12 and high sodium activity. These types of diagrams describe the thermodynamically predicted phases but do not address the kinetics of phase formation; nevertheless, data presented by Krumhansl et al. (1999) indicate that, for many tank waste compositions, analcime and Na-clinoptilolite should be the dominant Al-Si-bearing phases.

5.3 Hematite Phases

Baltpurvins et al. (1996) examined the effect of pH and anion composition on the precipitation of iron(III) hydroxide. The proportion of goethite (FeO(OH)) relative to hematite (Fe_2O_3) increased with increasing pH. In addition, the rate of transformation was influenced by the affinity of various anions to interact with the surface of the ferrihydrite particles. Sulfate was found to slow the transformation; however, nitrate slowed the transformation the least. The presence of nitrate changed the morphology of the crystals into blade-like forms similar to those observed in this study on AZ-101. The relative composition and crystal morphology of the product species were found to be dependent on both the anion type and the pH of the system. Hematite formation was favored at pH values near the point of zero charge of ferrihydrite (pH 7–9), whereas goethite formation was favored outside of this region. A correlation between enhanced hematite formation and both the relative affinities of the anions for the ferrihydrite particles and their relative aqueous phase complex stability constants was evident. This is thought to be a manifestation of the competing formation mechanisms of hematite and goethite.

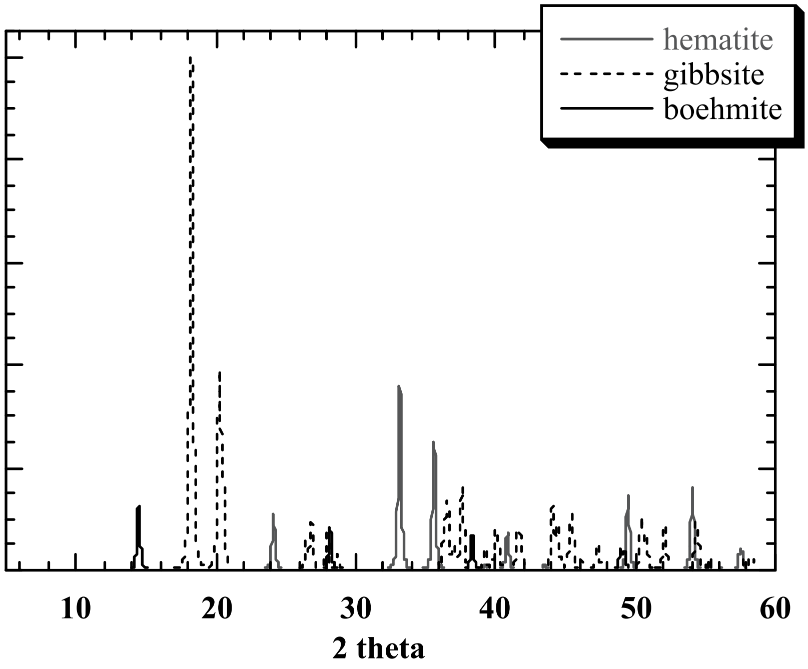

Figure 5.2. Simulated XRD Scan of AZ-101

The XRD scan shown in Figure 4.1a can be compared with the simulated scan in Figure 5.2. The simulated scan is composed of hematite (~20 vol%), gibbsite (~70 vol%) and boehmite (~10 vol%). There are several major reflections missing in the experimental XRD scan, including a significant peak from gibbsite. The simulation is performed with ideal powdered crystals. The missing reflections (110 and 200), suggest that there was preferential orientation in the **c**-direction of crystallites in the experimental AZ-101 washed solids sample. However, in the unwashed solids sample, there was no preferential orientation and the 110 and 200 reflections are visible (see Figure 4.7). This is consistent with the crystalline nature of gibbsite. In addition, the boehmite reflections were broadened due to their smaller crystallite size and crypto-crystalline nature in the AZ-101 samples. These features could not be duplicated in this computer simulation. Thus the simulation tends to underestimate the boehmite fraction.

5.4 Zirconium Phases in AZ-101

The zirconium-iron-bearing phase was observed only in the AZ-101 washed solids. The composition and structure of this phase remains unclear. Using different-sized probes the same composition was obtained, suggesting that this is a single phase. Lumetta et al. (1996) reports that tank wastes contain nano-sized particles of amorphous ZrO_2 and FeOOH. However, the technique used by Lumetta et al. (1996), TEM with a Be-window EDS system, would not have been able to establish whether these phases contained carbon or oxygen, for instance. Indeed, analysis of the data in this report suggests the composition is actually closer to a mixed Zr-Fe phase, similar to that observed in this study. Unfortunately, the EDS analyses by Lumetta et al. (1996) were not run long enough to allow minor elements to be detected. Based on the results of this study, it is highly unlikely that such pure phase oxides exist in the tank wastes. The true nature of these particles can only be determined with TEM equipped with light element-capable EDS and an electron energy-loss spectroscopy system.

The overlap of the Zr-L (2.042 keV) and the P-K (2.015 keV) lines in the EDS analysis can be severe. The presence of Zr can only be confirmed by the observation of the Zr-K line; however, phosphorus could still be present in the analyzed region. The magnitude of the overlap problem can be modeled (Figure 5.3). In Table 5.2, a composition is shown that produces a spectrum similar to an actual spectrum collected from sample AZ-101. Because the K-line x-ray efficiency is so much greater than other lines, even a small amount of Al, Si, or P yield a large peak in the x-ray spectrum.

The Zr-K peak is more prominent in the experimental spectrum because of the nature of the sample. This is because the weaker x-rays detection efficiency was slightly reduced. In addition, the bremmstrahlung is curtailed on the lower energy side more so on the experimental spectrum than in the simulated spectrum. These effects could be due to the surface roughness in the actual AZ-101 sample changes the characteristic x-ray collection efficiencies at the EDS detector. This simulation suggests that phosphorus may not be present in the sample at significant levels. As the cross-section for the Al-K, Si-K, or P-K lines are so high, even a small amount of these in the phase would have resulted in a large peak.

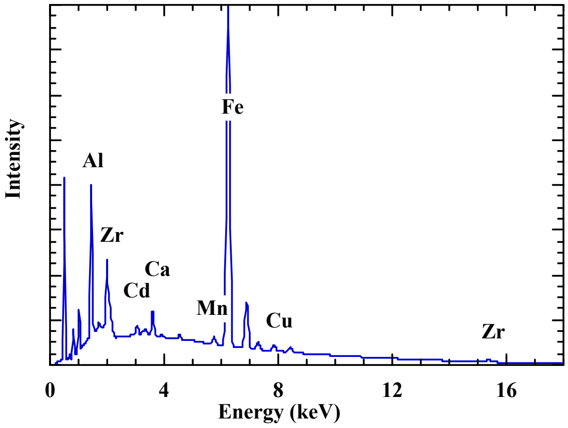

Figure 5.3a. Simulated EDS Spectrum of a Particle in AZ-101

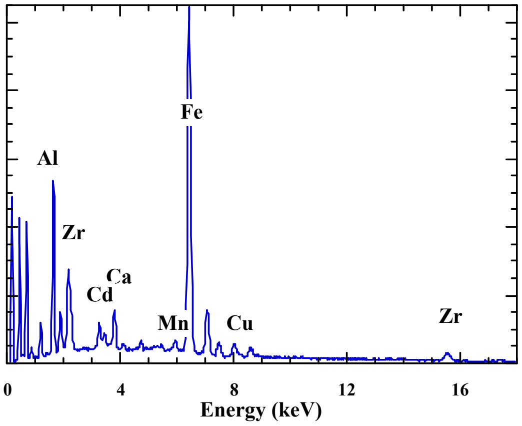

Figure 5.3b. Experimentally Obtained Spectrum from AZ-101

Table 5.2. Composition of Zr-Fe Phase Used in the Spectrum Simulation

Element	at%
Na	3.0
Al	5.0
O	56.0
Ca	0.6
Zr	14.0
Fe	16.0
Si	0.1
Cd	2.0
Sn	1.0
Ni	<0.5
Cu	<0.5
Mn	<0.5
La	<1.0

For instance, the 5 at% level of Al results in one of the largest peaks in the spectrum. In Figure 5.4, an experimentally obtained spectrum from ZrO_2 is shown. The intensity of the Zr-L line is very high relative to the Zr-K line. This is further evidence that phosphorus is unlikely to be present in this phase. In addition, the molar ratio of P to Zr is 0.24 according to Table 2.2, indicating that there is insufficient phosphorus in AZ-101 to generate a pure $Zr(PO_3)_4$ phase. The formula of the metal components in the phase based on the simulated spectrum is $Zr_{1.4}Fe_{1.6}Al_{0.5}$. Unfortunately, the EDS spectrum cannot provide clear evidence of a carbonate. All the SEM samples were coated with carbon, resulting in a minor peak that can increase in intensity as the area probed increases. However, evidence from infrared indicated the presence of some type of mixed phosphate-carbonate phase.

The zirconium-bearing phase appears to be an important component of AZ-101 washed solids, but its exact composition and structure remain unknown. To determine whether this phase is a carbonate and how much phosphate may be present, compositional data is needed from an instrument that does not

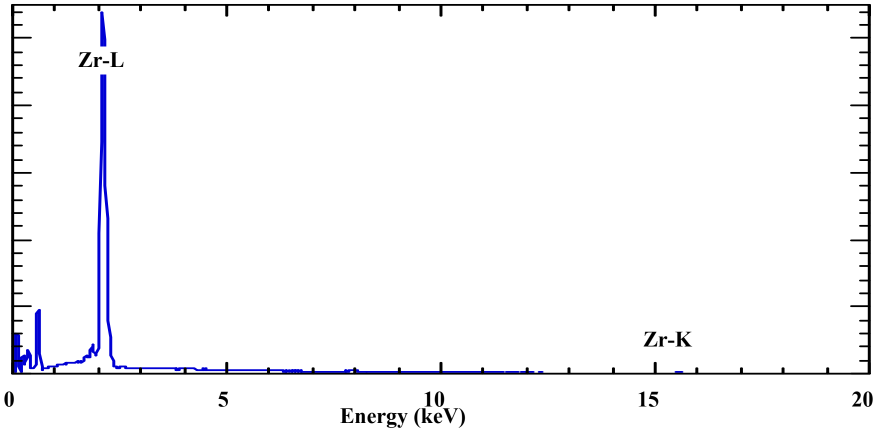

Figure 5.4. EDS Analysis of ZrO_2 for Estimating Collection Efficiencies for Zr-K and -L Lines

suffer from carbon coating issues and is able to extract structural data from the phase. For instance, analytical transmission electron microscopy (TEM) combined with electron energy-loss spectroscopy would allow determination of whether carbonate, phosphate, or both are present in these phases. The correct identification of these phases may assist in final waste immobilization in borosilicate glass.

5.5 Uranium-Bearing Phases

The one uranium-bearing phase is $Na_2U_2O_7$, supported by thermodynamic models and some observations (Jantzen and Laurinot 2001). In this study, we have observed the presence of euhedral uranium oxide particles in both AN-102 and AZ-101 washed solid samples; however, in each case, no evidence for Na-bearing uranate phases were found in the SEM-EDS analysis. The uranium oxide particles ranged in size from 5 to 8 µm in diameter to less than 1 µm. The shape of the particles suggests that they may have precipitated within the tanks. No transuranic elements were identified in the samples; however, none of the techniques used have the necessary detection capabilities to see these elements. Given the distribution of the uranium phases and their probable scattering potential, it is likely that they would be detected with XRD. In AN-102, these particles were fairly common and were attached to the bulk amorphous-looking Na-Al material. The XRD match to uraninite (UO_2) was not convincing in either AZ-101 or AN-102, but a reasonable match to UO_3-type phases was found. Under caustic conditions, it is possible that hydrated uranyl oxide hydrate, e.g., schoepite (ideal $UO_3 \cdot 2H_2O$) or uranyl carbonate, rutherfordine (UO_2CO_3), phases might precipitate. Schoepite has characteristic reflections at 0.736, 0.366, 0.359, 0.348, and 0.324 nm. Schoepite was reported in S-104 sludge by Lumetta et al. (1997). Although the TEM images look characteristic of a uranyl oxide hydrate phase, there are insufficient data to confirm the existence of schoepite. Some of these reflections may be present in the XRD scans of AZ-101, but this is simply not strong enough evidence to support the identification of schoepite in the tank waste samples. Direct identification of this micron-sized phase can only be obtained with TEM.

5.6 Minor Phases in the Samples

In both AN-102 and AZ-101, iron chromium oxide particles were observed occasionally. These would be expected to scatter at greater intensity than many of the other phases, even though they were minor components. Iron-bearing particles and iron chromium nickel were relatively common. These types of phases are unlikely to be metallic because an oxygen signal was visible in all analyses. The manganese phase observed in unwashed solids from AZ-101 was relatively common. Its composition was determined to be close to that of $Na_3MnAl_{0.2}K_{0.2}O_x$. This composition does not match any known manganese phase but, as stated earlier, quantification with SEM-EDS is problematic, particularly for the light elements, sodium and oxygen. The phase may be related to manganese clay minerals (e.g., asbolane or birnessite), which produce a strong reflection near 0.70±0.02 nm (the interlayer spacing). The manganese clay minerals have a two-dimensional layered structure that consists of edge-shared MnO_6 octahedra with cations and water molecules occupying the interlayer region (Chukhrov et al. 1980). Manganese clay mineral phases can be formed through oxidation of Mn^{2+} in concentrated NaOH solution. Although an unidentified reflection is observed near 0.7 nm, the XRD evidence is not strong enough for positive identification of this phase.

As the cerium-bearing particle (possibly cerianite, CeO_2) and the yttrium vanadate particle (possibly wakefieldite, YVO_4) were observed only once, these must be considered trace components. Cerianite (CeO_2) and powellite ($(Nd,La)WO_4$) have been observed to precipitate during long-term corrosion of borosilicate waste glasses exposed to high pH (Abdelouas et al. 1997). Tungsten-bearing particles were not observed in the samples. Zeolitic phases are commonly formed during borosilicate waste glass dissolution above pH 9–10. Wakefieldite can be formed by reacting yttrium nitrate with vanadium oxide at pH 12.5 (Riwotzki and Haase 1998) and has a structure similar to that of wakefieldite.

One problem with SEM-EDS is that the probe excites an area approximately 1 μm^3 in volume; thus it can be difficult to obtain a signal from a single phase. A higher spatial resolution technique such as TEM would be more useful in these cases because the composition would be exact, and structural information on the individual particle could be obtained (Buck et al. 1996). Quantitative information on phase distributions cannot be obtained with the techniques described in this report.

5.7 Nitrates

Evidence for sodium nitrate and nitrite phases was present in the XRD spectrum of AN-102 (see Figure 3.8). These are evaporite phases. The sample preparation methods for SEM were generally more effective at reducing the total volume of these soluble phases. Evidence for $NaNO_2$ and $NaNO_3$ was reported by Lumetta et al. (2001). It is possible to identify these solely on the basis of XRD data. Table 5.3 lists possible phases reported in the JCPDS database. Because these phases are soluble, changes in the sample preparation method can easily result in their removal.

Table 5.3. XRD Data on Sodium Nitrite and Sodium Nitrate

Compound	Major d-Spacings (nm)			JCPDS Ref.
$NaNO_3$	0.304	0.231*	0.190*	36-1474
Na_3NO_3	0.230*	0.260*	0.163	34-743
$Na_2N_2O_3$	0.229	0.268	0.258	35-926
$NaNO_2$	0.298	0.279*	0.204	6-392
*Match to measured d-spacing within +/-0.01 nm.				

The gas generation studies reported by Bryan et al. (2002) demonstrated that nitrous oxide and nitrogen gas were produced during thermal testing. The origin of the nitrogen in these gases must be from the large volume percent of nitrates and nitrites in the AN-102 solids. Because both SEM and XRD are unable to detect organic phases, infrared spectroscopy of the sample would be worthwhile. Infrared techniques were used on AZ-101 washed solids but not on AN-102 washed solids. A clearer picture of the AN-102 solids for simulant development might be accomplished by using multiple characterization techniques as well as some phase separation techniques to isolate different components. All techniques have limitations but, by using a large range of techniques, it is possible to reduce the degree of speculation. Nitrate phases were also clearly present in the unwashed AZ-101 sample but were not observed in the washed AZ-101 sample.

5.8 Particle Size Analysis

The primary particles in the tank wastes tend to associate to form larger agglomerates that can further associate into flocs. Primary particles and agglomerates have been shown by Tingey et al. (1999) to span five orders of magnitude. Tingey et al. (1999) identified the smallest particles as pure hydrous oxides of Zr and Fe that were only 3 to 6 nm in diameter. Next in size were the boehmite phases, ranging from 100 to 1 µm. These submicron particles form agglomerates that are 1 to 10 µm in diameter. Tingey et al. (1999) reported that the largest isolated crystals in Tank C-112 waste were gibbsite ($Al(OH)_3$) and exceeded 20 µm in diameter. Particle size data from very high ionic strength suspensions can be difficult to interpret; however, with the supporting SEM information, it is possible to interpret the data more effectively. Table 5.4 lists all phases observed in AN-102 washed solids and AZ-101 washed and unwashed solids and the estimated particle sizes. During the process of drying on a dead-end filter exposed to air, however, particle agglomeration can occur. For instance, precipitation of aluminate gels has plugged some of the pipes connecting the Hanford tanks (Tingey et al. 1999). However, during actual waste processing, this type of agglomeration is unlikely to occur. Although the sample contained a range of high-Z particles, the average refractive index assigned for the particle size measurement of 1.50 was appropriate for the sodium-aluminate particles that were the major phase in the AN-102 sample. This report illustrates that there are several measures of the equivalent diameter of a particle because individual particles in AN-102 do not have a single diameter. As with most complex particle systems, the particles in AN-102 are irregular with rough surfaces and unequal dimensions in different directions.

Table 5.4. Phase Identification and Particle Size Results

Element/ Species	AZ-101 Washed Solids	Particle Diameter (µM)	Technique Used	AN-102 Washed Solids	Particle Diameter (µM)	Technique Used
Al	Gibbsite	2-3	XRD	Boehmite,	ND	XRD
Al	Boehmite	ND	XRD	Zeolite	5–20	SEM, EDS
Al	Zr-Fe phase	0.5–2	SEM-EDS	Na-aluminate	<1	EDS
Ba	ND	NA	NA	ND	NA	NA
C as TIC	Carbonate	NA	IR, EDS	Carbonate	NA	EDS
C as TOC	ND	NA	NA	ND	NA	NA
Ca	Calcite	5	SEM-EDS	Zeolite, calcite	5–20	EDS
Cd	Cd-Sn phase	4–8	SEM-EDS	ND	NA	
Ce	ND	NA	EDS	Cerianite	10	EDS
Cl	ND	NA	NA	ND	NA	NA
Cr	Chromite	NA	EDS	Chromite		EDS
Cu	Fe-Zr phase, chromite	0.5–2	SEM-EDS	ND	NA	NA
F	ND	NA	NA	ND	NA	NA
Fe	Hematite	1–3	SEM, XRD	Chromite	NA	EDS
Fe	Fe-Zr phase	0.5–2	SEM-EDS	Hematite	NA	XRD, EDS
K	Mn-clay	0.3–0.5	SEM-EDS	Zeolite	5–20	SEM
La	Fe-Zr phase	0.5–2	EDS	ND	NA	NA
Mg	ND	NA	NA	ND	NA	NA

Table 5.4. Phase Identification and Particle Size Results

Element/ Species	AZ-101 Washed Solids	Particle Diameter (µM)	Technique Used	AN-102 Washed Solids	Particle Diameter (µM)	Technique Used
Mn	Mn-clay	0.3–0.5	SEM	ND	NA	NA
Mo	ND	NA	NA	ND	NA	NA
Na	$NaNO_3$	NA	XRD, EDS	Zeolite	5–10	SEM, XRD
Na	NA	NA	NA	Na-aluminate	<1	SEM-EDS
Nd	Fe-Zr phase	0.5–2	SEM-EDS	ND	NA	NA
Ni	Fe-Zr phase	0.5–2	SEM-EDS	Chromite	10	NA
NO_2	$NaNO_3$	NA	IR	$NaNO_3$	NA	XRD
NO_3	$NaNO_2$	NA	IR	$NaNO_2$	NA	XRD
P	Phosphate	NA	IR	ND	NA	NA
Pb	ND	NA	NA	ND	NA	NA
Pd	ND	NA	NA	ND	NA	NA
Rb	ND	NA	NA	ND	NA	NA
Ru	ND	NA	NA	ND	NA	NA
Si	Fe-Zr phase	0.5–2	NA	Zeolite	5–20	SEM
SO_4	Na sulfate	NA	IR	Na sulfate	NA	EDS
Sn	Cd-Sn phase	4–8	SEM-EDS	ND	NA	NA
Sr	ND	NA	NA	ND	NA	NA
Te	ND	NA	NA	ND	NA	NA
Th	ND	NA	NA	ND	NA	NA
U	U(VI)-oxide	5–20	SEM-EDS	U(VI) oxide	5–10	SEM-EDS
V	ND	NA	NA	Wakefieldite	5	SEM-EDS
Y	ND	NA	NA	Wakefieldite	5	SEM-EDS
Zr	Fe-Zr phase	0.5–2	SEM-EDS	ND	NA	NA

ND = element was not detected with SEM-EDS or IR, NA = not applicable
Particle diameter based on SEM observations of individual particles. Some particles were present as agglomerates.
Note: Some elements are listed more than once because they were present in more than one phase.

5.9 Sample Size Issues

Given the extremely small volume of the SEM, PSD, IR, and XRD samples relative to the bulk sample volume, there are issues with these being representative of the bulk material. In addition, the high activity in some samples, particularly AZ-101, necessitated further reduction of the sample size to allow examination in the various instruments. The tank waste samples are all highly heterogeneous, meaning that larger sample volumes need to be examined to be more confident in the results. However, comparison of the chemical analyses of AN-102 and AZ-101 with the SEM-EDS data, indicates that the disposition of most major and minor components has been determined. For example, evidence of co-precipitation of lanthanum and neodymium within the Fe-Zr phase in AZ-101. In addition, mineral phase data on some trace components has been established, for example, the yttrium vanadium phase in AN-102. The positive identification of a few phases; however, can tell us the approximate conditions in the tanks and will assist in thermodynamic modeling of potential phases likely to be present in the tanks.

6.0 Conclusions

Hanford Tanks 241-AN-102 (AN-102) and 241-AZ-101 (AZ-101) washed solids samples were characterized by means of scanning electron microscopy (SEM), x-ray diffraction (XRD), infrared spectroscopy (IR), and laser light scattering particle size determination (PSD) to provide a better basis for a simulant. Identification of various phases was included.

In the AN-102 extracted from the third wash, the microstructural analysis provides evidence for the presence of zeolites, including a calcium alumino-silicate phase. XRD and SEM-EDS suggests the presence of boehmite (AlOOH) and sodium aluminate, in AN-102. Evaporite phases, sodium nitrate ($NaNO_3$) and sodium nitrite ($NaNO_2$) phases were detected in the XRD scans. A number of minor phases were also found attached to the surface of the bulk material. The AN-102 sample did not have detectable levels of gibbsite. Uranium oxide particles, ranging in size from 1–5 μm in diameter, were found in the AN-102 sample. The species of these compounds could not be positively identified; however, the uranium phases were not sodium uranates. Iron oxide (hematite) and iron chromium nickel oxide (chromite) were observed. A much rarer cerium oxide (possibly cerianite) and yttrium vanadate particles (possibly wakefieldite) were also found in the AN-102 sample.

The laser light-scattering particle size analysis of the AN-102 washed solids sample indicated that most of the slurry volume was due to particles in the 0.5 to 15 μm particle size of undetermined structure. However, under sonication, particles appeared to break apart, resulting in a larger volume of smaller-diameter particles. After sonication most of the particles were between approximately 0.6 and 3.0 μm. The results of the particle size analysis were reasonably consistent with observations made with SEM on the nature of the particles; however, because the samples were extracted from dewatered and washed solids on a dead-end filter exposed to air, significant changes have occurred. This means that any direct interpretation of the SEM images to actual waste processing conditions is erroneous. The light-scattering methods are undoubtedly more accurate in determining the actual particle size during plant operation.

Zeolites were not found in the two samples of AZ-101 solids. Both samples contained boehmite and gibbsite and a number of smaller particles. A calcium pure phase, possibly calcite ($CaCO_3$), was also identified. Uranium oxide (possibly schoepite or rutherfordine) particles ranging in size from 5–10 μm to <1 μm in diameter were common in the AZ-101 samples. Hematite (Fe_2O_3) was positively identified by XRD and SEM morphology. Iron chromium nickel oxide (chromite) particles were observed in both samples. A zirconium iron (Zr:Fe = 1:1) phase was common in the washed and less common in the unwashed sample. These phases also contained aluminum, lanthanum, and neodymium. Other rare earths may be present. The phase may be mixed aluminate-carbonate-phosphate, according to infrared analysis. The occurrence of phosphate and/or carbonate with heavy metals may be an important consideration during vitrification. A manganese-bearing phase was also commonly found in the unwashed sample. Particle size analysis of these AZ-101 samples is described in Urie et al. (2002).

Poorly crystallized boehmite and well-formed hematite were found in both AZ-101 and AN-102. Gibbsite was found in AZ-101 but not in AN-102. Drying under heat could have resulted in increased levels of gibbsite in AZ-101; however, the drying procedures were the same for both sets of samples. The identification of other phases such as schoepite is, at present, tentative. A significant number of smaller particles were also found attached to the bulk material. Iron chromium nickel oxide (chromite), cerium oxide (cerianite), and yttrium vanadate (wakefieldite) particles were also found in the sample. Further detailed analysis with analytical transmission electron microscopy would be necessary to identify the individual phases conclusively and determine the location of specific elements. This information could then be used to reanalyze the bulk analysis data to obtain more reliable estimates of particle types and quantities and greatly assist in the understanding of the waste samples.

7.0 References

Abdelouas A, JL Crovisier, W Lutze, B Grambow, JC Dran, and R Müller. 1997. “Surface layers on a borosilicate nuclear waste glass corroded in $MgCl_2$ solution.” *J. Nucl. Mater*. Vol. 240, pp. 100-111.

Baltpurvins, KA, RC Burns, GA Lawrance, and AD Stuart. 1996. “Effect of pH and Anion Type on the Aging of Freshly Precipitated Iron(III) Hydroxide Sludges.” *Environ. Sci. Technol*. Vol. 30, pp. 939–944.

Bryan SA, JGH Geeting, and RL Sell. 2002. *Thermal and Radiolytical Gas Generation from Washed AN-102 Sludge.* PNWD-3201, Battelle – Pacific Northwest Division, Richland, WA.

Buck EC, NR Brown, and NL Dietz. 1996. “Contaminant Uranium Phases and Leaching at the Fernald Site in Ohio.” *Environ. Sci. Technol*. Vol. 30, pp. 81-88.

Chukhrov FV, AI Gorshkov, ES Rudnitskaya, VV Beresovskaya, and AV Sivtsov. 1980. “Manganese minerals in clays: A review.” *Clays Clay Miner*. Vol. 28, pp. 346-354.

Geeting, JGH, KP Brooks, RT Hallen, LK Jagoda, AP Poloski, DR Weier, and RD Scheele. 2002. *Filtration, Washing, and Caustic Leaching of Hanford AZ-101 Sludge*. PNWD-3206, Battelle Pacific Northwest Division, Richland, WA.

Jantzen CM, JE Laurinot and KG Brown. 2002. "Thermodynamic modeling of the SRS Evaporators: Part I. The 2H and 2F Systems (U)" Westinghouse Savannah River Company Report, WSRC-TR-2000-00293, Rev 1, Aiken, SC.

Johnston CT, SF Agnew, JR Schoonover, JW Kenney III, B Page, J Osborn, and R Corbin. 2002. “Raman Study of Aluminum Speciation in Simulated Alkaline Nuclear Waste.” *Environ. Sci. Technol.* Vol. 36, pp. 2451-2458.

Krumhansl JL, PV Brady, PC Zhang, HL Anderson, SE Arthur, SK Hutcherson, MA Molecke, C Jove-Colon, J Liu, M Qian, KL Nagy, and B Wakoff. 1999. *Final Report: Phase Chemistry of Tank Sludge Residual Components*. Environmental Management Science Program, Project No. 60403. On line at: http://www.osti.gov/em52/final_reports/60403.pdf (accessed March 2003).

Lumetta GJ, BM Rapko, MJ Wagner, J Liu, and YL Chen. 1996. *Washing and Caustic Leaching of Hanford Tank Sludges: Results of FY1996 Studies*. PNNL-11278 Rev 1, Pacific Northwest National Laboratory, Richland, WA.

Lumetta GJ, IE Burgeson, MJ Wagner, J Liu, and YL Chen. 1997. *Washing and Caustic Leaching of Hanford Tank Sludge: Results of FY1997 Studies.* PNNL-11636 Rev 1, Pacific Northwest National Laboratory, Richland, WA.

Lumetta GJ, RT Hallen, IE Burgeson, RL Sell, SD Halstead, JP Bramson, OT Farmer III, LR Greenwood, ED Jenson, MJ Steele, and MW Urie. June 2001. *Evaporation of a Mixture of Tank AN-102 Low-Activity Waste and C-104 Washing and Leaching Solutions*. WTP-RPT-017, Battelle – Pacific Northwest Division, Richland, WA.

Mattigod, SV, DT Hobbs, LQ Wang, DM Dabbs, and IA Aksay. 2002. *Precipitation and Deposition of Aluminum-Containing Species in Tank Wastes*. Environmental Management Science Program, Project No. 81887. On line at: http://emsp.em.doe.gov/portfolio/AbstractDetails.asp?ProjectID=373 (accessed March 2003).

Music S, D Dracevic, S Popovic, and N Vdovic. 1998. "Microstructural properties of boehmite formed under hydrothermal conditions." *Mater. Sci. Eng*. Vol. 52, pp. 145-153.

Riwotzki K and M Haase. 1998. "Wet chemical synthesis of doped colloidal nanoparticles: YVO_4:Ln (Ln= Eu, Sm, Dy)." *J. Phys. Chem*. Vol. B102, pp. 10129-10135.

Tingey JM, JD Berg, KD Keefer, AS Lea, DR Rector, JW Virden, and S Stenkamp. 1999. *Final Report: Colloidal Agglomerates in Tank Sludge: Impact on Waste Processing*. Environmental Management Science Program, Project No. 54628. On line at: http://www.osti.gov/em52/final_reports/54628.pdf (accessed March 2003).

Urie MW, GM Mong, PR Bredt, AP Poloski, JA Campbell, RD Scheele, OT Farmer, CZ Soderquist, SK Fiskum, RG Swoboda, LR Greenwood, MP Thomas, EW Hoppe, and JJ Wagner. 2002. *Chemical Analysis and Physical Property Testing of 241-AZ-101 Tank Waste—Supernatant and Centrifuged Solids.* PNWD-3215, Battelle – Pacific Northwest Division, Richland, WA.

Venkatesan KA, PR Vasudeva, and K Stamberg. 2001. "Modeling of the sorption of Sr(II) on hydrous zirconium oxide." *J. Radioanal. Nucl. Chem*. Vol. 250, pp. 477-484.

Distribution

No. of
Copies

OFFSITE

4 Savannah River Technology Center
Russ Eibling
PO Box 616, Road 1
Building 999-W
Aiken, SC 29808

Erich Hansen
PO Box 616, Road 1
Building 773-41A
Aiken, SC 29808

Jim Marra
PO Box 616, Road 1
Building 773-43A
Aiken, SC 29808

Harold Sturm
PO Box 616, Road 1
Building 773-A
Aiken, SC 29808

No. of
Copies

ONSITE

16 Battelle - Pacific Northwest Division

B.W. Arey	P8-16
J.M. Bates	K7-15
J.R. Bontha	K6-24
E.C. Buck	P7-27
A.R. Felmy	K8-96
S.K. Fiskum	P7-22
J.G.H. Geeting	P7-28
E.D. Jensen	P7-22
B.K. McNamara	P7-25
D.E. Kurath	P7-28
A.P. Poloski	P7-25
G.L. Smith	H4-02
Project File (2)	P7-28
Information Release (2)	K1-06

9 Bechtel National, Inc.

S.M. Barnes	H4-02
W.L. Graves	H4-02
H.R. Hazen	H4-02
D.E. Larson	H4-02
R.A. Peterson	H4-02
K. Prindiville	H4-02
P.S. Townson	H4-02
W.L. Tomasitis	H4-02
WTP PDC Coordinator	H4-02